
UNIVERSITATEA BABEŞ-BOLYAI
BABEŞ-BOLYAI TUDOMÁNYEGYETEM
BABEŞ-BOLYAI UNIVERSITÄT
TRADITIO ET EXCELLENTIA

# Laser Induced Photoelectron Holography in Diatomic Molecules

Ph.D. thesis

GELLÉRT ZSOLT KISS

SCIENTIFIC SUPERVISOR
PROFESSOR DR. LADISLAU NAGY

FACULTY OF PHYSICS, BABEŞ-BOLYAI UNIVERSITY
CLUJ-NAPOCA, ROMANIA
2019

Gellért Zsolt Kiss

# Laser Induced Photoelectron Holography in Diatomic Molecules

DOCTORAL THESIS

presented to the Faculty of Physics,
Babeş-Bolyai University, Cluj-Napoca, Romania
2019

# Abstract

Laser physics and technology has become a highly developing field of science in the recent years. With the remarkable achievements in the production of ultrashort and intense laser pulses new horizons have been opened for scientists to investigate ultrafast phenomena taking place at atomic level and to manipulate matter below the microscopic size. In parallel to the impressive developments in the laboratories the newly emerging and not completely understood processes needed to be explained by elaborate theoretical works.

The present thesis aims to deliver novel and useful knowledge to the broad theoretical field of laser-matter interaction, by investigating - with the use of first principle calculations - laser induced ultrafast processes taking place in small atomic systems in the presence of ultrashort XUV radiation fields.

In the first part of this work the theory behind the laser-atom/molecule interaction is detailed in the framework of the *single active electron approximation*, then different theoretical methods will be presented by comparing the results obtained by their numerical implementation for the hydrogen atom.

In the main part of the present thesis, first the development and the implementation of a numerical method based on the direct solution of *time-dependent Schrödinger equation* for diatomic molecules is presented, and then this is employed to investigate the laser induced electron dynamics and the *photoelectron holography* in the $H_2^+$ molecule.

Finally, the conclusions will be drawn, mainly on how the intensity of the laser field and the internuclear distance - via the value and the spatial profile of the binding potential - influence the *photoelectron spectra* and the interference patterns, that appear in the photoelectron hologram of the molecular target.

# Contents

CHAPTER 1.

# Introduction to laser technology

In the last decades laser science has become the most promising tool for detailed investigations of ultrafast phenomena taking place at atomic scales, and for matter manipulation with high energy concentrations. The "**l**igth **a**mplification by **s**timulated **e**mission [1] of **r**adiation" (laser) technique, which produces coherent and highly monochromatic light beams, was implemented first in experiments in 1960 [2], since then lasers have become routinely used in a wide array of applications in our daily life. These applications include industrial utilizations, such as material processing (cutting and welding with high-power light sources) and commercial uses in optical communications and computer technology, such as data transfer via optical fibers, data storing on digital optical discs (DVD, Blue-Ray), bar-code readers, laser printers, pointers, or scanners. For military purposes lasers are being integrated in energy weapons or in enemy disorientation devices, and they are routinely used for missile guidance and even as target designators. Beyond these commercial and military applications laser technology became crucial in the medical area, where high precision surgical procedures are needed: tumor removals for cancer treatments [3, 4, 5], eye [6], soft-tissue [7, 8] or even cosmetic surgeries [9].

Since the invention of the first laser apparatus laser technology has undergone a remarkable progress in the broad spectrum of fundamental scientific domains, ranging from high energy nuclear physics (by considering the recent improvements in laser driven fusion [10]), or atomic physics to the more complex fields of the biochemistry and pharmaceutics, where new horizons are being opened for the medicinal chemistry and drug synthesis[11]. At the heart of these important achievements lie the state-of-the-art laser techniques which allow the manipulation of matter at high spatial and temporal resolutions at nanoscopic and atomic scales. By the continuous implementation of the newly emerging methods higher and higher power beams have been produced, while shorter and shorter pulse durations achieved.

The year 1985 represented a milestone in this progress when the "chirped pulse amplification" (CPA) method was invented by Donna Strickland and Gérard Mourou[1], which gives us the possibility to amplify an ultrashort ($< 10$ fs $= 10^{-14}$ s) laser pulse up to and even above $10^{15}$ W/cm$^2$ intensity. Nowadays, the majority of high power ($> 10^{12}$ watts) laser facilities

[1]Donna Strickland and Gérard Mourou were awarded the Nobel Prize in Physics on 2nd of October 2018 for their joint work on CPA

all over the world are using the CPA technique, next to a number of commercial CPA based Ti:sapphire laser systems, which can produce peak powers between $10^{10}$ and $10^{11}$ watts. Moreover, by the implementation of the momentous laser facility, Extreme Light Infrastructure (ELI), new horizons seem to become accessible for the international laser community, where the aspiration to operate within extreme conditions has become a daily routine. In ELI, which until this moment is based on three different pillars: ELI-Beamlines in Prague (Czech Republic), ELI Attosecond Light Pulse Source (ELI-ALPS) in Szeged (Hungary), and ELI Nuclear Physics (ELI-NP) in Măgurele (Romania), fast and remarkable scientific progresses are being achieved already: e.g., ELI-NP holds the world record for the highest power (10 petawatts) produced ever [12].

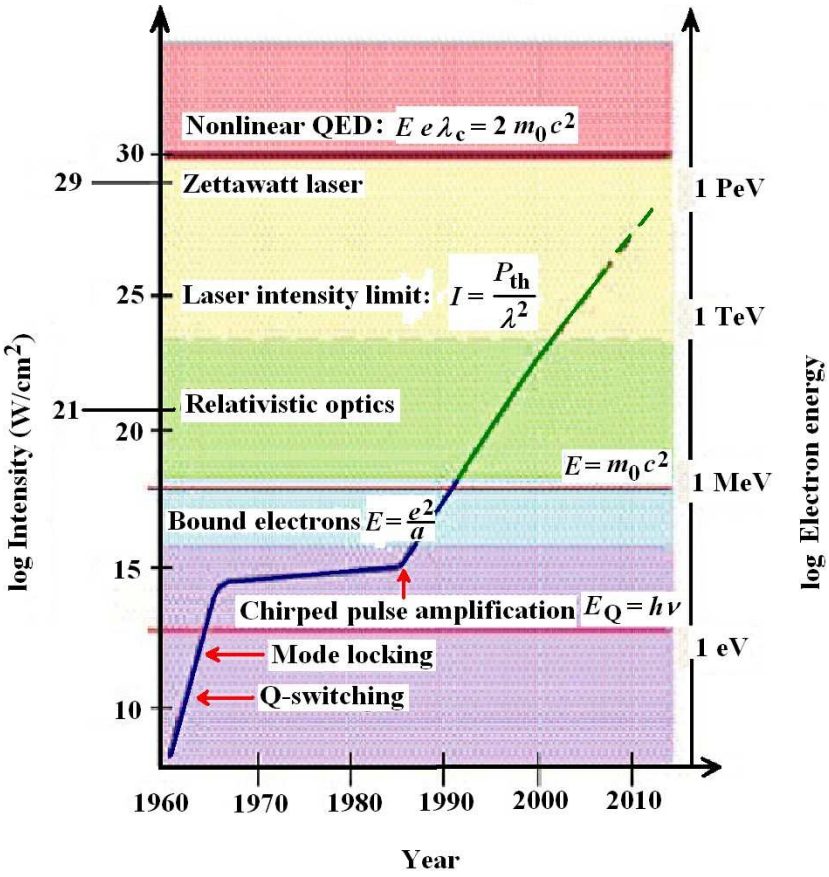


Figure 1.1: Progress in achievable light intensity with the year. The black curve shows a continuous increase having two large slopes, first around the year 1960 (the invention of the laser), and another one starting from 1985 (the invention of the CPA technique). The figure is adapted from Mourou and Yanovsky (2004) c 2004 OSA [13].

Due to the possibility of generating these extreme conditions (focusing high intensity pulses onto atomic systems and operating with ultrashort time scales) new and previously not entirely understood phenomena can be induced and investigated at the nanoscopic scale and below that. The most well known phenomenon that occurs during the interaction between an incident light beam [electromagnetic (EM) wave] and matter is the *photoelectric effect*, when the target system (atom/molecule) is ionized by the emission of a bound electron

from the negative energy region ($E_b < 0$) into the continuum (positive energy region $E_k > 0$) induced by the external EM field. To explain that regardless of the EM field intensity, light may eject electrons even at low intensities, Albert Einstein proposed [14] that the light beam can be considered as a collection of discrete wave packets, i.e. photons, each having a given $\nu$ frequency and energy $E_\nu = h\nu$. This link between the energy and frequency was given by Max Planck [15] via the Planck constant $h \simeq 6.626{\times}10^{-34}$ Js. In the photoelectric mechanism the bound electron absorbs a single photon from the radiation field and gets released, then detected experimentally as a *photoelectron* with the maximum energy of $E_k = h\nu - L$, where $L = -E_b > 0$ stands for the work function, i.e., the amount of energy that should be "invested" to release the bound electron. However, in the spacial case, when the energy of the absorbed photon is lower than the work function $L$, but equal to the energy difference between two bound states $h\nu = E_{b'} - E_b$, a process called *photoexcitation* takes place, which means that the electron is carried by the pumped energy from a lower energy level $b$ to the higher level $b'$.

It was observed later, that if the radiation field is a high intensity ($> 10^{10}$ W/cm$^2$) laser field, depending on the field's parameters next to the single photon ionization other ionization mechanisms may appear as well, such as the multi-photon ionization (MPI), above-threshold ionization (ATI), tunneling ionization (TI), or over-the-barrier ionization (OBI). Beyond these primary processes, secondary mechanisms may also occur resulting from the quiver motion of the ionized electron under the influence of the radiation field. Once the electric component of the laser field (e.g., a sinusoidal wave function of time) changes its sign (it reverse its direction) the previously ejected electron may be driven back so closely to the parent ion that will interact with this. During this interaction the EM field accelerated photoelectron with a probability different than zero may be reabsorbed by the ion, and during the recollision event a single, high-frequency photon is released. In experiments, where gas or solid targets are illuminated, these high-energy photons are detected as high harmonics of the initial beam, meaning that they will appear in the measured spectra having frequency values integer multiples $n\nu$ of the original light's frequency ($\nu$). This process is called high harmonic generation (HHG), and it enjoys a high-level of interest since it has opened the possibility to produce high energy attosecond (1 as = $10^{-18}$ s) pulses in the XUV regime. Apart from the high harmonic generation, according to a second scenario the laser-driven electron may not be reabsorbed but only scattered on the residual ion, resulting in the diffraction of the electron wave packet. The name of this process is the laser induced electron diffraction (LIED), and can be used to obtain structural information about the target [16]. This information regarding the geometry of the atom/molecule is imprinted in the measured photoelectron momentum distribution [or photoelectron spectra (PES)] [17] of the irradiated target. In the case when next to the diffracted (scattered) wave packet a second (unscattered, or weakly scattered) wave is also present, the coherent superposition of these two waves leads to a more structured photoelectron spectra than in the case of LIED. It has been shown [18] that the well distinguishable radial fringe pattern in the PES is created by the interference of

the wave packets emitted during the same quarter cycle of the radiation field but following different paths (i.e., accumulating a certain phase difference). In this picture, where the weakly scattered EWP is considered as part of the reference wave packet and the strongly scattered EWP as part of the signal wave packet, the spatial interference pattern may be interpreted as the hologram of the target, and the process itself as the holographic mapping (HM) of the target's state. Since the location of the interference minima and maxima located in the HM pattern strongly depend on the local (short range) potential of the parent ion experienced by the strongly scattered EWP, the HM can be considered a promising tool for extracting relevant structural information about the irradiated system.

By the recent developments in the field of laser science, experimental groups reached the limit of the order of attoseconds for the pulse durations[19], while world leading theoreticians are contributing to that with their theoretical works based on comprehensive - in the most occasions first-principle (*ab-initio*) - calculations [20, 21]. These recent achievements, which resulted in the decrease of the pulse durations to the femto- and sub-femtosecond regime opened new possibilities in the imaging and controlling of quantum processes taking place in atomic and molecular systems. The typical time scale at which the most well known quantum phenomena occur is situated below the region of picoseconds ($10^{-12}$ s). As illustrated on Figure 1.2 the motion (vibration) of the atoms in molecules and solids occurs at the order of tens and hundreds of femtoseconds (1 fs = $10^{-15}$ s), while the dynamics of the electrons in nanostructures or in smaller systems are taking place between few attosecond (1 as = 1fs/1000 = $10^{-18}$ s) and hundreds of femtoseconds.

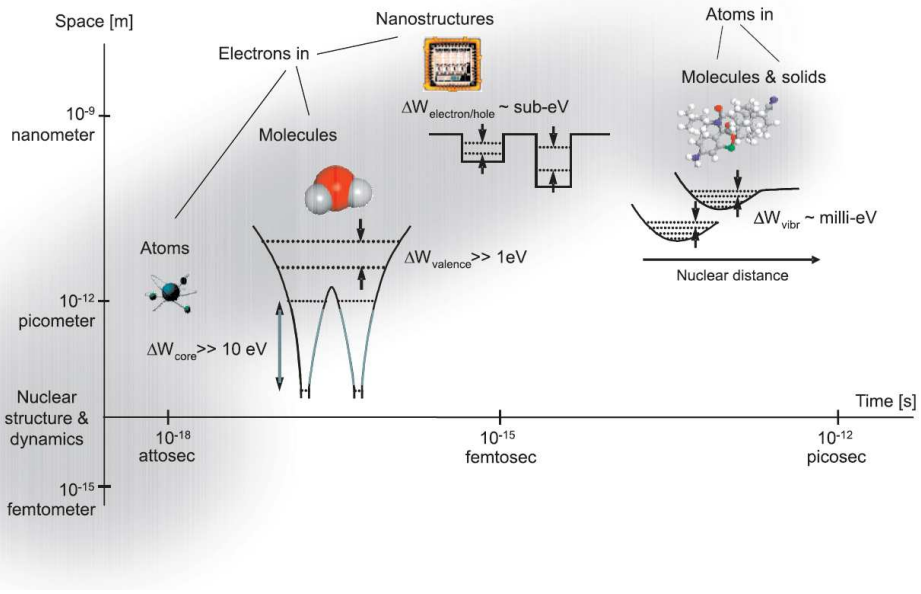


Figure 1.2: Time scales and characteristic lengths for dynamics in atoms and molecules. Adapted from [19].

With the production of fs pulses the area of the ultrafast spectroscopy was born, and the possibility to follow and study in real time the movement of atoms in molecules during

chemical reactions. By using attosecond laser pulses the making of ultrafast movies from the motion of bound electrons inside atoms and molecules became possible [22, 23]. Beyond real time investigations, by finding the optimal pulse parameters lasers may also be used as appropriate tools to induce desired quantum states in the targets in order to facilitate chemical reactions [24, 25].

Due to the newly emergent phenomena, resulted from the interaction between matter and ultrashort, high intensity radiation fields, a correct understanding of the underlying processes is required. This can be achieved by extensive and elaborate theoretical investigations, which on the other hand will play an important role to generate further directions for experimentalists and for new technical developments in the field of laser science and technology. The present work is a theoretical one, which aims to deliver additional and deeper understanding - by the development of efficient numerical tools - in the field of laser induced electron dynamics, mainly to decipher the features appearing in the photoelectron spectra of the diatomic ($H_2^+$) molecule. The work, as it will be presented in the following sections, is based on first principle calculations.

CHAPTER 2.

# Laser-matter interaction

## 2.1 Principle of lasers

A traditional laser apparatus, as its name (light amplification by stimulated emission of radiation) indicates, is based on the *stimulated emission* phenomenon, which notion was intuitively first introduced and explained by Albert Einstein in 1917 [26]. Nowadays, the term "lasers" are used worldwide to describe all sources of lights that emit coherent electromagnetic waves in the form of narrow beams.

From the dawn of the quantum mechanics we know that inside atoms/molecules the electrons are located on well defined (discrete) energy levels, and via an energy change process with the environment they may jump between these levels. By the absorption of external energy an electron may be excited to a higher energy state $|\psi_2\rangle$, and after a short period of time ($\sim 10^{-8}$ s) with a high probability will spontaneously jump back to a lower energy (ground) state $|\psi_1\rangle$ by emitting its excess energy ($\Delta E = E_2 - E_1$) into its environment. When this exes energy is emitted in a form of a photon ($E_{photon} = \Delta E$), the process is known as the *spontaneous emission*. However, if a photon with energy similar to $\Delta E$ passes by the excited electron prior to that the spontaneous emission happens, by interacting with this will stimulate the release of the excess energy in the form of a photon. This process is referred to as the *stimulated emission* and the released photon is emitted in the same direction as the incident one, having the same frequency, phase and polarization. These processes could be exhaustively described within the quantum radiation theory elaborated by Paul Dirac starting from the 1920s. Due to the later and notable works done by the American Charles Hard Townes and the Soviet physicist, Aleksandr Prokhorov and Nikolay Basov, a significant amount of new theoretical knowledge had been acquired until the 1950s, leading to the construction of the first radiation amplifier by J. P. Gordon *et al* [27] in 1954, which operated in the microwave regime. This was named *maser*, which is the acronym for "microwave amplification by stimulated emission of radiation". It was the first time, when experimentally was proven that microwave radiation can be amplified by using specially prepared ammonia molecules ($NH_3$). Later in 1958, A. H. Schawlow and C. H. Townes published [28] the principles of the optical masers and gave new perspectives for building such

amplifying devices that can operate at shorter wavelengths, e.g., in the optical regime [1]. A few years later, in 1960, based on this article, Theodore H. Maiman constructed the first laser in the Hughes Research Laboratories. This device used ruby crystals to produce amplified radiation at $\lambda = 694$ nm wavelength. Since 1960, due to the continuous developments in laser science, new laser devices have been constructed, which operated at various wavelengths: covering the major part of the electromagnetic spectrum, starting from the microwave region ($\lambda \sim 1$ mm) down to the XUV ($\lambda \sim 10$ nm) radiations (see Figure 2.1 at the end of this section).

A traditional laser apparatus is made of from three essential components: the active medium, the energy pump, and the optical resonator. Considering a medium with a two level system where $E_1 < E_2$, the intensity of an electromagnetic wave which travels through this medium in the $Ox$ direction is given by the Beer-Lambert-Bouguer law

$$I_\nu(x) = I_\nu(0)e^{-\mu(\nu)x}, \tag{2.1}$$

where $\nu$ is the frequency of light, and the absorption coefficient $\mu(\nu) = [N_1 - N_2(g_1/g_2)]\sigma(\nu)$ depends on the population densities $N_1$, $N_2$, the multiplicity (statistical weights) of the two levels $g_1$ and $g_2$ ($g = 2J + 1$ with $J$ being the total angular momentum quantum number of the electron), while $\sigma(\nu)$ is the absorption cross section of the $|\psi_1\rangle \rightarrow |\psi_2\rangle$ transitions. An amplification of the radiation field can be obtained if $\mu(\nu)$ becomes negative, i.e., the condition $N_2 > (g_2/g_1)N_1$ is met. Considering that under thermal equilibrium conditions - according to the Boltzmann distribution law - the lower energy levels are first populated and remain more populated than the higher energy levels, i.e.,

$$N_2 = N_1 \frac{g_2}{g_1} \exp\left(-\frac{E_2 - E_1}{k_b T}\right). \tag{2.2}$$

The $N_2 > (g_2/g_1)N_1$ *population inversion* may be achieved only in non-equilibrium by pumping external energy (optically or in the form of electric current) into the system. However, it can be shown that if the medium is built up from a group of atoms with only two energy-levels the population inversion can not be achieved, since the continuously excitations will reach equilibrium with the de-exciting processes (spontaneous and stimulate emissions), and the $N_1 \rightarrow N_2$ population transfer will stop when $N_1 = N_2$ is met, resulting in the so-called optical transparency. Hence, in order to achieve non-equilibrium conditions, at least one additional - intermediate - energy state ($|\psi_3\rangle$) is required with the condition $E_1 < E_2 < E_3$. In the case of the three-level lasers the *pumping process*, which depending on the active medium can be an optical pump process of a flash-lamp, an electrical discharge, or even some chemical reactions, will excite the atoms from the $E_1$ to the $E_3$ energy level. Then a fast *radiationless transition* $E_3 \rightarrow E_2$ will occur, where the $\Delta E_{32} = E_3 - E_2$ energy is transferred into heat

[1] In 1964 Townes, Prokhorov and Basov were awarded the Nobel Prize in Physics for their works regarding the developments of masers and lasers.

(e.g., vibrational motion). An electron from the level $E_2$ will decay to $E_1$ by releasing a photon with the energy $h\nu = E_2 - E_1$ (*laser transition*). Given that the lifetime of the later transition is much longer than the former one, i.e., $\tau_{21} \gg \tau_{32}$, the population of the $E_3$ level will be practically zero next to the population of the second energy level: $N_3/N_2 \approx 0$, therefore the population of the excited (state) atoms will accumulate on the $E_2$ energy level, while the highest level becomes practically vacated. Thus, during the pump process further atoms can be excited to the $E_3$, and consequently the condition $N_2 > N_1$ achieved (the pump transition is faster than $\tau_{21}$), which leads to population inversion.

In order to obtain even higher amplification of the electromagnetic wave, the active medium is introduced into an *optical resonator* (optical cavity), which in the simplest setup is a Fabry-Pérot interferometer. In this case the active medium is placed between two highly reflecting mirrors separated by the distance $L$ giving the possibility for the beam to make hundreds of passes through the gain medium. One of the mirrors is called the *high reflector* and is used to reverse the incident light back into the active medium, thus its reflectance in the most optimistic case should be $R_1 \simeq 1$. The other mirror is the *output coupler* and it is only partially reflective, i.e., $R_2 \geq 99\%$, which allows a small portion of the beam to transmit through it. In this way, an initial wave with intensity $I_\nu(0)$ which travels through the medium and which is reflected back twice by the mirrors, is amplified by the factor of

$$G(\nu) = I_\nu(2L)/I_\nu(0) = R_1 R_2 e^{-2L\mu(\nu)} = (1 - T_2)e^{-2L\mu(\nu)}, \tag{2.3}$$

where $T_2$ is the transmittance of the output coupler and given that it is a small number one can safely use that $1 - T_2 \simeq e^{-T_2}$. By taking into account, that other factors dependent on the laser frequency $\nu$ may also be present in the amplification process, e.g., scattering and diffraction losses, which work against the beam amplification, these unwanted losses together with the transmittance of the output mirror can be grouped together into a loss factor $\gamma(\nu)$, and the gain of the intracavity beam after a round-trip given as

$$G(\nu) = e^{-[2L\mu(\nu)+\gamma(\nu)]}. \tag{2.4}$$

Considering that the field amplification occurs when $G(\nu) > 1$, the expression for the minimal population inversion required for this condition can be deduced to:

$$\Delta N_{\min} = \frac{g_1}{g_2} N_2 - N_1 \geq \frac{\gamma(\nu)}{2L\sigma(\nu)} \tag{2.5}$$

Lasing is achieved when this condition is fulfilled by the pumping process. In the first step randomly emergent spontaneously emitted photons appear in the medium, and a part of them which are ejected along the axis of the resonator will be reflected back and stimulate the emission of secondary photons emitted from the atoms already pumped to the excited level. These secondary photons will have the similar directions, phases and frequencies as the

initial ones, and will further stimulate newly excited atoms found on the $|\psi_2\rangle$ level. Hence, an avalanche of highly coherent photons will appear inside the active medium which will travel along the resonator axis. The signal of those initial photons that were not emitted parallel to the resonator axis will not gain final amplification, since they either will not be reflected by the mirrors or after a few reflections will exit the cavity or absorbed by the resonator's side walls. As a consequence, their signal will be lost for the lasing process.

In real systems where many atoms are present inside the cavity the transition between the energy states will not be exactly the same for all the radiating elements, since each atom may experience a slightly different environment. The electron cloud of each atom is influenced by the presence and motion of its neighboring atoms, hence its energy levels and transition rates may be slightly shifted from the well defined and exact values obtained for the case where only a single atom would be present in the radiation field. From the statistical point of view, this can be translated into the simple picture, according to which the energy levels of each atom is broadened. As a consequence, the active medium will have the capability to amplify frequencies located inside a certain range $\nu \pm \Delta\nu_{\max}$, where $\nu = \Delta E_{21}/h$. However, the physical size (the inter-mirror distance $L$) of the optical resonator will differentiate between these possible frequencies, in a way that after many reflections - from the mirrors - only those waves will show constructive interference, whose multiple integer of their half wavelength is equal to the optical path length

$$n \cdot L = q\frac{\lambda}{2}. \tag{2.6}$$

In the relation above $n$ is the refractive index of the medium, through which the light travels with the speed $c/n$, and the integer number $q$ is known as the longitudinal (axial) *mode order*, that labels the frequencies $\nu_q = qc/(2nL)$ of the standing waves confined in the cavity. All other waves whose lengths do not satisfy this relation will be suppressed by destructive interference and will not take part in the amplification process. Considering that, the separation between the axial nodes $\Delta\nu_{\text{ax}} = \nu_{q+1} - \nu_q = c/(2nL)$ is usually smaller than the spectral width of the amplification ($\Delta\nu_{\text{ax}} < 2\Delta\nu_{\max}$), the laser will operate simultaneously for all $q$ nodes where $\nu_q \in [\nu - \Delta\nu_{\max}, \nu + \Delta\nu_{\max}]$ and where the condition (2.5) for the population inversion can be fulfilled by the pumping process [i.e., $G(\nu_q) > 1$]. The selection of a fewer modes for the lasing process can be done either by shortening the length of the interferometer (in this case $\Delta\nu_{\max}$ will increase and the number of $\nu_q$ inside the gain domain decrease), or by inserting into the resonator a frequency selective optical component, the so-called Fabry-Pérot etalon. It has to be mentioned though, that the cost of both mode-selection methods will be manifested in efficiency losses.

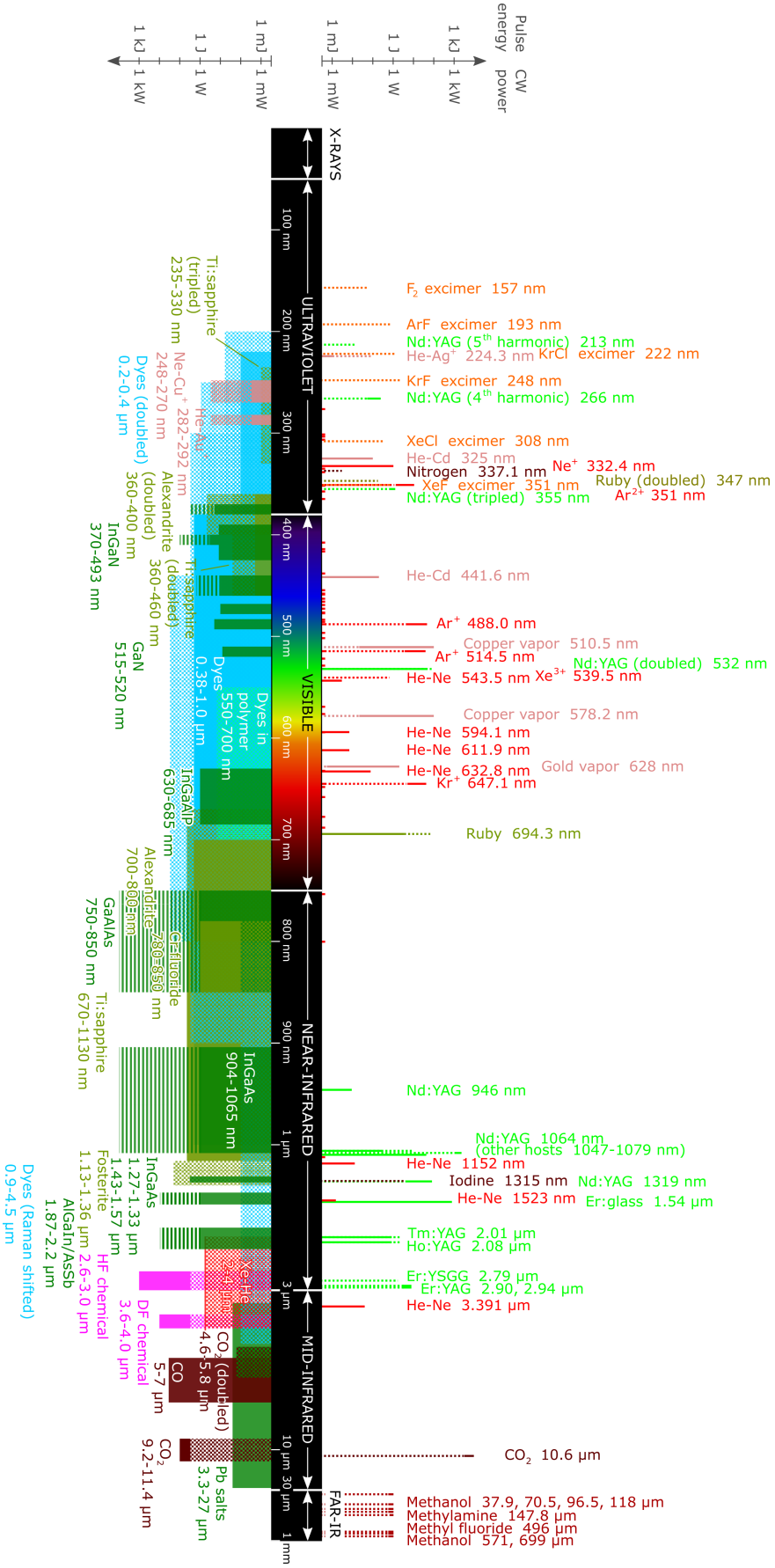


Figure 2.1: Wavelengths of commercially available lasers (as of May 2019). Most of the data available online can be found in Weber's book *Handbook of laser wavelengths* [29].

## 2.2 Maxwell's equations for describing the laser field

In the picture of the classical physics a laser field is described by its electric $\vec{E}(\vec{r};t)$ and magnetic $\vec{B}(\vec{r};t)$ component, which are the solutions of the *Maxwell equations* (SI units) in the vacuum [no electric charge density ($\rho = 0$), no electric current ($\vec{J} = 0$)]:

$$\begin{aligned} \nabla \cdot \vec{E}(\vec{r};t) &= 0 \\ \nabla \cdot \vec{B}(\vec{r};t) &= 0 \\ \nabla \times \vec{E}(\vec{r};t) &= -\frac{\partial \vec{B}(\vec{r};t)}{\partial t} \\ \nabla \times \vec{B}(\vec{r};t) &= \frac{1}{c^2}\frac{\partial \vec{E}(\vec{r};t)}{\partial t}, \end{aligned} \tag{2.7}$$

where the two vectors are orthogonal to each other ($\vec{E} \cdot \vec{B} = 0$) and $c = 2.99792458 \times 10^8$ m/s is the speed of light - the speed of the electromagnetic radiation - in free space. $\nabla$ is the so-called nabla, or Del, - the vector differential - operator, which in the Cartesian coordinate system is given as

$$\nabla = \hat{x}(\partial/\partial x) + \hat{y}(\partial/\partial y) + \hat{z}(\partial/\partial z), \tag{2.8}$$

where $\hat{x}, \hat{y}, \hat{z}$ represent the orthogonal unit vectors ($\hat{x}^2 = \hat{y}^2 = \hat{z}^2 = 1$; $\hat{x}\cdot\hat{y} = \hat{y}\cdot\hat{z} = \hat{z}\cdot\hat{x} = 0$). The electric and magnetic fields may also be expressed in terms of a scalar potential $\Phi(\vec{r};t)$ and a vector potential $\vec{A}(\vec{r};t)$:

$$\begin{aligned} \vec{E} = -\nabla\Phi(\vec{r};t) - \frac{\partial \vec{A}(\vec{r};t)}{\partial t}, \\ \vec{B} = \nabla \times \vec{A}(\vec{r};t). \end{aligned} \tag{2.9}$$

These potentials are not uniquely defined and can be freely adjusted until the electric and magnetic fields remain unchanged. These adjustments are the so called **gauge transformations**. By performing the following transformation - involving the vector potential -

$$\vec{A}(\vec{r};t) \rightarrow \vec{A}(\vec{r};t) + \nabla f^G(\vec{r};t), \tag{2.10}$$

with $f^G(\vec{r};t)$ (the so-called *gauge function*) being an arbitrary real function of space and time, the magnetic field remains unchanged:

$$\vec{B} = \nabla \times (\vec{A} + \nabla f^G) = \nabla \times \vec{A}, \tag{2.11}$$

since $\nabla \times (\nabla f^G) = 0$. However, this transformation will change the electric component accordingly to:

$$\vec{E} = -\nabla\Phi - \frac{\partial \vec{A}}{\partial t} - \nabla\frac{\partial f^G}{\partial t} \equiv -\nabla\left(\Phi + \frac{\partial f^G}{\partial t}\right) - \frac{\partial \vec{A}}{\partial t}. \tag{2.12}$$

To avoid the change of the electric field a second transformation - involving the scalar potential - should be used, which reads as:

$$\Phi(\vec{r};t) \rightarrow \Phi(\vec{r};t) - \frac{\partial f^G(\vec{r};t)}{\partial t}. \tag{2.13}$$

## The Coulomb (radiation) gauge

In electrodynamics or quantum chemistry a frequently used gauge is the **Coulomb gauge** ($CoulG$), or radiation gauge, when the condition

$$\nabla \cdot \vec{A}(\vec{r};t) = 0 \tag{2.14}$$

is fulfilled, and the scalar potential that satisfies the equation $\nabla(\nabla\Phi) = \Delta\Phi = -\rho/\epsilon_0$ (deducible from the general form of Maxwell's first equation, i.e., from the Gauss law: $\nabla\vec{E} = \rho/\epsilon_0$) will be zero, since in the free space electromagnetic radiation the electric charge density $\rho = 0$. It is a convenient choice to use the Coulomb gauge, since the electric component of the laser field is calculated in this way simply by the negative of the time derivative of the vector potential:

$$\vec{E}(\vec{r};t) = -\frac{\partial\vec{A}(\vec{r};t)}{\partial t}. \tag{2.15}$$

By introducing Equation (2.15) and $\vec{B} = \nabla \times \vec{A}$ into Maxwell's fourth equation (2.7), and applying the general vector relation of

$$\vec{a} \times (\vec{b} \times \vec{c}) = \vec{b}(\vec{a} \cdot \vec{c}) - (\vec{a} \cdot \vec{b})\vec{c} \tag{2.16}$$

one obtains: $\nabla(\nabla\cdot\vec{A}) - \nabla^2\vec{A} = (-1/c^2)\,(\partial^2/\partial t^2)\,\vec{A}$, where the first term disappears ($\nabla\vec{A} = 0$), and the Maxwell's equation in potential formalism using the Coulomb gauge leads to the homogeneous wave equation for the vector potential

$$\frac{\partial\vec{A}^2(\vec{r};t)}{\partial t^2} = c^2\nabla^2\vec{A}(\vec{r};t). \tag{2.17}$$

It can be easily proven, that the above equation is satisfied by monochromatic plane waves having the wavelength $\lambda$ and phase $\varphi$, and which can be described generally by the complex functions

$$\vec{A}_{\lambda,\varphi}(\vec{r};t) = \hat{\epsilon}A_0\left[e^{i(\vec{k}\vec{r}-\omega t-\varphi)} + e^{-i(\vec{k}\vec{r}-\omega t-\varphi)}\right], \tag{2.18}$$

where $i = \sqrt{-1}$ is the imaginary unit, $\omega$ is the angular frequency, $\vec{k}$ is the propagation vector ($|\vec{k}| = \omega/c = 2\pi/\lambda$), $\hat{\epsilon}$ is the polarization vector, and $A_0$ represents the amplitude of the vector potential.

By considering Eq. (2.18), for the electric ($\vec{E}$) and magnetic component ($\vec{B}$) of the laser field (as the solutions of the Maxwell's equations) two monochromatic plane waves are

obtained, which propagate in space with the speed of light $c$, and are perpendicular to each other and to the propagation direction:

$$\begin{aligned}\vec{E}(\vec{r};t) &= \hat{\epsilon}E_0\cos(\vec{k}\cdot\vec{r}-\omega t-\varphi)\\ \vec{B}(\vec{r};t) &= (\hat{k}\times\hat{\epsilon})\frac{E_0}{c}\cos(\vec{k}\cdot\vec{r}-\omega t-\varphi),\end{aligned} \tag{2.19}$$

where $E_0 > 0$ is amplitude of the electric field. The above equations describe a continuous wave, which has infinite temporal and spatial extents, and which is employed (as an appropriate tool) when the interaction between matter and continuous-wave lasers or multi-cycle ("long") laser pulses are studied. In other cases, when ultrashort few-cycle laser fields are considered (as in our case) the temporal shape of the $\vec{E}(\vec{r};t)$ gets modified, since the ultrashort laser pulses are produced by the superposition of monochromatic plane waves with appropriate frequencies ($\nu$), amplitudes ($E_0$) and phases ($\varphi$). When the propagation direction and the polarization of these components are the same, the net electric field composed by the constituent waves can be described mathematically with the equation:

$$\vec{E}(t) = \begin{cases}\hat{\epsilon}E_0F_{\text{mask}}(t)\sin(\vec{k}\cdot\vec{r}-\omega t+\varphi_0), & \text{if } ;t\in[0,\tau]\\ 0, & \text{otherwise,}\end{cases} \tag{2.20}$$

where $\tau$ is the duration of the laser pulse, $F_{\text{mask}}(t)$ is an envelope function that shapes the temporal profile of the pulse, and $\varphi_0$ describes the difference between the carrier-wave (with angular frequency $\omega$) and the envelope. The most frequently used mask functions in laser-matter investigations are the Gauss- and square-envelopes. In the present work I used a sine-square envelope function having the mathematical form of: $F_{\text{mask}}(t) = \sin^2(\pi t/\tau)$.

## The dipole approximation

In numerous occasions, when smaller systems (light atoms, few atomic molecules) are used as laser targets, it is a convenient and a valid approach to use the dipole approximation (DA), which states that spatial variations of the electric field may be neglected [i.e., $\vec{E}(\vec{r};t)\rightarrow\vec{E}(t)$] in the vicinity of the target, since the wavelength of the incident wave $\lambda$ is much larger than the position $\vec{r}$ of the ejected electron: $\lambda >> r$. In the present case we considered XUV pulses having the central wavelength in the order of 100 nm ($= 10^{-7}$ m), while the typical size of an atom or diatomic molecule is in the interval of ½ Ångstrom (the size of the hydrogen atom) and tens of Ångstroms (1 Å$= 10^{-10}$ m). In this way, the electric field and the vector potentials are approximated as

$$\begin{aligned}\vec{E}(\vec{r};t) &\rightarrow \vec{E}(t)\\ \vec{A}(\vec{r};t) &\rightarrow \vec{A}(t) = -\int_0^t \mathrm{d}t' E(t'),\end{aligned} \tag{2.21}$$

meanwhile the condition [Eq. (2.14)] of the Coulomb gauge remains valid as well. In addition to this, within the dipole approximation the magnetic component of the laser field disappears:

$$\vec{B}(\vec{r};t) \approx \nabla \times \vec{A}(t) = 0. \tag{2.22}$$

In the next few lines, the mathematical deduction of the dipole approximated electric field is presented. By taking into account that the magnitude of the propagation vector $|\vec{k}| = 2\pi/\lambda$ is inversely related to the wavelength $\lambda$ of the incident light, for small target systems the condition $kr \ll 1$ is valid. By denoting with $x = |\vec{r}|/\lambda$, and using the unity vectors $\hat{k} = \vec{k}/|\vec{k}|$, $\hat{r} = \vec{r}/|\vec{r}|$ the expression of the vector potential [Eq. (2.18)] may be given in the form of

$$\vec{A}(\vec{r};t) = \hat{\epsilon}A_0 \left[\exp\left\{i[2\pi x\hat{k}\hat{r} - (\omega t + \varphi)]\right\} + \exp\left\{-i[2\pi x\hat{k}\hat{r} + (\omega t + \varphi)]\right\}\right]. \tag{2.23}$$

By using the Taylor series and employing the multipole expansion of Equation (2.23) the form of the vector potential in dipole approximation reads as

$$\vec{A} \approx \hat{\epsilon}A_0 \left(1 + \mathcal{O}(x)\right) \left[e^{-i(\omega t+\varphi)} + e^{i(\omega t+\varphi)}\right], \tag{2.24}$$

where $\mathcal{O}(x)$ stands for the error of the expansion. Considering this, in the expression of the laser's electric field (2.20) the term $\vec{k} \cdot \vec{r} \leq 2\pi|\vec{r}|\lambda$ will vanish. Therefore, the short-pulsed laser field is described by its electric component, which in the present work will be considered with the following analytical form:

$$\vec{E}(t) = \begin{cases} \hat{\epsilon}E_0 \sin^2\left(\frac{\pi t}{\tau}\right) \sin(\omega t + \varphi_0), & \text{if } ; t \in [0, \tau] \\ 0, & \text{otherwise.} \end{cases} \tag{2.25}$$

## 2.3 Charged particle in laser field

A particle having the electric charge $q$ and mass $m$ is accelerated in the laser field by the Lorentz force:

$$\vec{F}_{\mathrm{L}} = m\frac{\mathrm{d}^2\vec{r}}{\mathrm{d}^2t} = q\left[\vec{E} + \vec{v} \times \vec{B}\right], \tag{2.26}$$

where $\vec{v} = \mathrm{d}\vec{r}/\mathrm{d}t$ is the electron's velocity. In the dipole approximation and using the Coulomb gauge the force between the particle and the laser field gets simplified, and the dynamics of the charged particle will be simply governed by the electric field of the incident radiation field:

$$\vec{a} = \frac{\mathrm{d}^2\vec{r}}{\mathrm{d}^2t} \approx \frac{q}{m}\vec{E}(t). \tag{2.27}$$

However, in order to describe generally the dynamics of the quantum particle in radiation field, the Hamiltonian of the system needs to be obtained first (the starting point of quantum physics calculations). A complete picture concerning the interaction with radiation fields can

be acquired by employing the *Lagrangian formalism*, where

$$\frac{\mathrm{d}}{\mathrm{d}t}\left[\frac{\partial\mathcal{L}(\vec{r},\vec{v};t)}{\partial\vec{v}}\right]-\frac{\partial\mathcal{L}(\vec{r},\vec{v};t)}{\partial\vec{r}}=0 \tag{2.28}$$

is the Euler-Lagrange equation, and it is identical with the Newton's law for the force [i.e., Equation (2.26)], in the case when for the $\mathcal{L}(\vec{r},\vec{v};t)$ Lagrangian the appropriate expression is introduced:

$$\begin{aligned}\mathcal{L}(\vec{r},\vec{v};t) &= T(\vec{v})-U(\vec{r},\vec{v};t)= \\ &= \frac{1}{2}m\vec{v}^2-q\left[\Phi(\vec{r};t)-\vec{v}\vec{A}(\vec{r};t)\right].\end{aligned} \tag{2.29}$$

Using the canonical momentum

$$\vec{\mathcal{P}}=\frac{\partial\mathcal{L}}{\partial\vec{r}}=m\vec{v}+q\vec{A}(\vec{r};t) \tag{2.30}$$

the Hamiltonian function will be given as

$$H(\vec{r},\vec{v};t)=\vec{\mathcal{P}}\cdot\vec{v}-\mathcal{L}(\vec{r},\vec{v};t)=\frac{1}{2}m\vec{v}^2+q\Phi(\vec{r};t). \tag{2.31}$$

After introducing the expression $\vec{p}=\vec{\mathcal{P}}-q\vec{A}$, the above equation leads to the Hamiltonian, which is expressed in terms of the scalar and vector potentials as

$$H(\vec{r},\vec{\mathcal{P}};t)=\frac{\left[\vec{\mathcal{P}}-q\vec{A}(\vec{r};t)\right]^2}{2m}+q\Phi(\vec{r};t). \tag{2.32}$$

Here, it has to be stressed out that the above equation describing the Hamiltonian is a gauge invariant expression, and while the kinetic momentum and other physical observable quantities remain invariant, the canonical momentum $\vec{\mathcal{P}}$ depends on the chosen gauge.

## Quantum mechanical description

In the *non-relativistic limit* and by neglecting the small spin dependent terms, the Hamiltonian of a quantum particle is obtained by replacing the quantities in Equation (2.32) with their corresponding operators (e.g., the canonical momentum $\mathcal{P}$ in coordinate representation is replaced by the operator $\hat{\mathcal{P}}=-i\hbar\nabla$):

$$\hat{H}=\frac{\left[\hat{\mathcal{P}}-q\hat{A}\right]^2}{2m}+q\hat{\Phi}. \tag{2.33}$$

The Hamilton operator will act on the wave function $\Psi(\vec{r};t)$, which is introduced to describe the charged particle being in the quantum state $|\Psi(t)\rangle$, and the modulus square of which gives the probability density

$$\frac{\mathrm{d}P(\vec{r};t)}{\mathrm{d}\vec{r}}=|\Psi(\vec{r};t)|^2 \tag{2.34}$$

of finding the particle in position $\vec{r} \in [\vec{r}, \vec{r}+\mathrm{d}\vec{r}]$ at time moment $t$. The action of the Hamilton operator on the quantum state reads as:

$$\hat{H}|\Psi(t)\rangle = \left[\frac{1}{2m}\hat{\mathcal{P}}^2 - \frac{q}{2m}\left(\hat{\mathcal{P}}\hat{A} + \hat{A}\hat{\mathcal{P}}\right) + \frac{q^2}{2m}\hat{A}^2 + q\hat{\Phi}\right]|\Psi(t)\rangle. \tag{2.35}$$

In the Coulomb gauge [$\nabla \cdot \vec{A}(\vec{r};t) = 0$ and $\Phi(\vec{r};t) = 0$] and by using the coordinate representation of the operators $\hat{\mathcal{P}} = -i\hbar\nabla$, $\hat{A} = \vec{A}(\vec{r};t)$ and $\hat{\Phi} = \Phi(\vec{r};t)$, one can easily prove the equality

$$\begin{aligned}\hat{\mathcal{P}}\left(\hat{A}|\Psi(\vec{r};t)\rangle\right) + \hat{A}\left(\hat{\mathcal{P}}|\Psi(\vec{r};t)\rangle\right) &= -i\hbar\left(\nabla\vec{A}\right)|\Psi(\vec{r};t)\rangle + 2\vec{A}\left(\hat{\mathcal{P}}|\Psi(\vec{r};t)\rangle\right) = \\ &= 2\vec{A}\hat{\mathcal{P}}|\Psi(\vec{r};t)\rangle,\end{aligned} \tag{2.36}$$

and give the expression of the Hamiltonian as

$$\hat{H}^{\mathrm{CoulG}}(\vec{r};t) = \frac{1}{2m}\hat{\mathcal{P}}^2 - \frac{q}{m}\vec{A}(\vec{r};t)\hat{\mathcal{P}} + \frac{q^2}{2m}\vec{A}^2(\vec{r};t), \tag{2.37}$$

which in dipole approximation yields to

$$\hat{H}^{\mathrm{CoulG}}_{dip}(\vec{r};t) = \frac{1}{2m}\hat{\mathcal{P}}^2 - \frac{q}{m}\vec{A}(t)\hat{\mathcal{P}} + \frac{q^2}{2m}\vec{A}^2(t). \tag{2.38}$$

## Gauge transformations

As it was mentioned earlier, the mathematical form of the vector potential $\vec{A}(\vec{r};t)$ and scalar potential $\Phi(\vec{r};t)$ can be freely chosen according to the gauge transformations (2.10)-(2.13) leaving the physical observables [the electric field ($\vec{E}$) and the magnetic field ($\vec{B}$)] unchanged. However, in quantum mechanics, the gauge transformations should be also applied on the wave function $\Psi$ and on the arbitrary operator $\hat{A}$ as follows

$$\begin{aligned}\Psi &\rightarrow \Psi' = \hat{T}\Psi \\ \hat{A} &\rightarrow \hat{A}' = \hat{T}\hat{A}\hat{T}^{\dagger},\end{aligned} \tag{2.39}$$

where the transformation operator $\hat{T}$ is defined as

$$\hat{T} = \exp\left\{-i\frac{q}{\hbar}f^G(\vec{r};t)\right\}, \tag{2.40}$$

with $f^G(\vec{r};t)$ being the gauge function, while the expectation value of the measurable quantity $A$ remains gauge invariant:

$$\langle A\rangle = \frac{\langle\Psi'|\hat{A}'|\Psi'\rangle}{\langle\Psi'|\Psi'\rangle} \equiv \frac{\langle\Psi|\hat{A}|\Psi\rangle}{\langle\Psi|\Psi\rangle}. \tag{2.41}$$

Besides the Coulomb gauge another two favored choices are the *velocity* and the *length gauge*s, which can be obtained from the first by employing the quantum mechanical transformations according to Eq. (2.39) by employing the appropraite (correct) gauge functions $f^G$.

### *Velocity gauge*

In the velocity gauge the potentials and the wave functions are obtained by transforming the potentials from the dipole approximated Coulomb gauge by using the following generating function

$$f^G(\vec{r};t) \rightarrow f^G_{cg\rightarrow vg}(t) = -\frac{-q}{2m}\int_{-\infty}^{t} \mathrm{d}t'[\vec{A}^{cg}(t')]^2. \tag{2.42}$$

The expression for these functions yields to:

$$\begin{aligned}
\vec{A}^{vg}(t) &\rightarrow \vec{A}^{cg}(t) + \nabla f^G_{cg\rightarrow vg}(t) \equiv \vec{A}^{cg}(t) \\
\Phi^{vg}(t) &\rightarrow \Phi^{cg}(t) - \frac{\partial f^G_{cg\rightarrow vg}(t)}{\partial t} \equiv \frac{q}{2m}[\vec{A}^{cg}(t)]^2 \\
|\Psi^{vg}(\vec{r};t)\rangle &\rightarrow \exp\left\{\frac{iq^2}{\hbar 2m}\int_{-\infty}^{t}\mathrm{d}t'[\vec{A}^{cg}(t')]^2\right\}|\Psi^{cg}(\vec{r};t)\rangle.
\end{aligned} \tag{2.43}$$

Since in many circumstances the term containing $\vec{A}^2(t)$ is much smaller then the term depending on $\vec{A}$, the former is usually neglected from the Hamiltonian operator, which yields to a simplified form of the Hamiltonian in the velocity gauge

$$\hat{H}^{vg} = \frac{\hat{\mathcal{P}}}{2m} - q\vec{A}(t)\frac{\hat{\mathcal{P}}}{m} + \frac{qA^2(t)}{2m} \simeq \frac{\hat{\mathcal{P}}}{2m} - q\vec{A}(t)\frac{\hat{\mathcal{P}}}{m}. \tag{2.44}$$

In Eq. (2.44) it can be observed that the vector potential is coupled with the *velocity* $\vec{v} \leftarrow \hat{\mathcal{P}}/m$ of the charged particle.

### *Length gauge*

The length gauge is obtained by using the following generating function

$$f^G(\vec{r};t) \rightarrow f^G_{cg\rightarrow lg}(t) = -\vec{r}\vec{A}(t), \tag{2.45}$$

which leads to the expressions of the vector and scalar potential

$$\vec{A}^{lg}(t) \rightarrow \vec{A}^{cg}(t) + \nabla\left[-\vec{r}\vec{A}^{cg}(t)\right] = 0$$

$$\Phi^{lg}(t) \rightarrow \Phi^{cg}(t) + \vec{r}\cdot\frac{\partial\vec{A}(t)}{\partial t} = -\vec{r}\cdot\vec{E}(t) \tag{2.46}$$

and transforms the wave function (i.e., quantum state) according to:

$$|\Psi^{lg}(\vec{r};t)\rangle \rightarrow \exp\left\{\frac{iq}{\hbar}\vec{r}\vec{A}(t)\right\}|\Psi^{cg}(\vec{r};t)\rangle. \tag{2.47}$$

Using the above equations the Hamiltonian in length gauge reads as:

$$\hat{H}^{lg} = \frac{\hat{\mathcal{P}}^2}{2m} - q\vec{r}\vec{E}(t), \tag{2.48}$$

which in the case when the charged particle is the electron ($q = -e = -1.6\times10^{-19}$ C) it is written as: $\hat{H}^{lg} = (\hat{\mathcal{P}}^2/2m) + e\vec{r}\vec{E}(t)$. In addition to that, if the particle is also influenced by an electrostatic field created by the local electric charges found in the particle's vicinity (e.g., positively charged nuclei, or negatively charged electron cloud) the Hamiltonian should be complemented also with the potential energy term $V(\vec{r})$ in order to describe these interactions.

In this work I preferred to use the length gauge [considering the expression Eq. (2.48) of the Hamiltonian], since its numerical implementation is less complicated than the use of other gauge approaches.

CHAPTER 3.

# Laser induced processes in atoms and molecules

As already specified in the introductory part (Chapter 1) the interaction of short and intense laser pulses with atoms and molecules mainly manifests in the field induced motion of the light electrons. The vibration and rotation of the heavier nuclei begin to play also an important role in the field induced dynamics, when the wavelength of the intense radiation field is in the upper range of the spectrum, i.e., in the infra-red (IR) domain. In these extreme conditions the bond-breaking and fragmentation of larger molecular systems (biomolecules) may also occur. Although, in most cases when interactions with ultrashort (tens of attosecond) pulses in the XUV regime are studied - as in the present case - the Bohr-Oppenheimer and the fixed nuclei approximation can be safely considered and the motion of the nuclei neglected next to the dynamics of the electrons. Thereby, we will focus our attention only on the electron's dynamics inside the laser field and at this moment will not consider the investigation of the nuclear motion.

In the following section the main aspects regarding the various types of photoionization (PhI) processes will be briefly presented. This will be followed by a short review on the high harmonic generation (HHG) process, which is one of the most promising and interesting result of the photoionization for the area of attosecond pulse generations. Finally, the theory behind the holographic mapping (HM) of atoms and molecules using laser driven photoelectrons will be discussed.

## 3.1 Photoexcitation and ionization mechanisms

The primary processes during the interaction between atomic systems and external electromagnetic fields consist of the electron excitation (or stimulated de-excitation) and photoionization of the irradiated system. Since the investigation of the dynamics of the ejected electrons presents the central topic of the present thesis the nature of these mechanisms will be briefly summarized.

## Photoexcitation and de-excitation

A single photon excitation occurs when an electron located on a $|\psi_i\rangle$ bound state (at the beginning of the laser field usually the ground state) absorbs one photon whose energy is lower than the $I_p$ ionization energy of the target (i.e., measured from the given initial state), but equal to the

$$\varepsilon_{\text{ph}} = h\nu = \varepsilon_f - \varepsilon_i \tag{3.1}$$

energy difference between a final (excited bound) and the initial state. One photon excitations begin to be the dominant mechanisms even at low and moderate laser field intensities, since inside a laser pulse many photons with different frequencies are simultaneously present, and it is probable for the electron to "find" a photon with the appropriate energy to jump to the next (excited) level. According to the selection rule of optical transitions when the electron absorbs a single photon and is excited to the $|\psi_f\rangle$ final state its orbital quantum number $l$ will be increased or decrease by one ($\Delta l = l_f - l_i \pm 1$). In the case of high intensity laser fields the photon density is higher, and two or multi-photon absorptions may be present. In the case of the two photon excitation the electron absorbs two photons almost at the same time and jumps from the initial state to the higher energy level $\varepsilon_{f'} = 2h\nu + \varepsilon_i$ while its orbital quantum number is changed according to $\Delta l = 0$.

## Single-photon ionization

When the absorbed photon's $h\nu$ energy is greater than the $I_p$ ionization energy of the target, the electron will be released by the laser field from the ground state into the continuum with the kinetic energy

$$\varepsilon_{\text{kin}}^{SPI} = \frac{p^2}{2m} = h\nu - I_p. \tag{3.2}$$

The *single-photon ionization (SPI)* mechanism may be present even at low and moderate field intensities, and is a dominant ionization process when the photon density is low (e.g., it is dominant when short wavelength - UV, XUV, X-rays - lasers are used and where the energy per photon ratio is high).

## Multi-photon and above-threshold ionization

By the continuous developments in the laser technology the field's intensities have been further increased. However, these high field (amplifications) intensities were first achieved for larger wavelengths, i.e., shorter $\nu$ central frequencies, meaning relatively low photon energies, which were not suitable to fulfill the (3.2) condition of the single-photon ionization. Nonetheless, experimentalists were still able to observe electrons in the continuum. Due to the high field intensities these photoelectrons were liberated by absorbing multiple number of photons. The energy gain from an integer number of $n$ photons is transformed into the kinetic energy of the ejected electrons according to the relation

$$\varepsilon_{\text{kin}}^{MPI} = n \cdot h\nu - I_p, \tag{3.3}$$

and the process is known as the *multi-photon ionization* (MPI) mechanism. Phenomenologically, this process can be explained with the existence of virtual energy levels inside the atom/molecule, which are separated by the energy difference $\Delta\varepsilon = h\nu$ and have a very short $\Delta t$ lifetime according to the relation $\Delta\varepsilon \cdot \Delta t \geq \hbar/2$, which is known as the Heisenberg uncertainty principle. During this short period of time [i.e., $\Delta t \geq 1/(\nu 4\pi) = T/(4\pi)$] a virtually excited electron may absorb another $h\nu$ energy photon and will advance to the next virtual level. This action is repeated till the total energy of the electron will be positive (i.e., the electron is released). In the spacial case when the virtual levels coincide with actual excited states the process known as the resonant enhanced multi-photon ionization mechanism takes place. When the electron absorbs more than the sufficient number of photons to acquire positive energy, the *above threshold ionization (ATI) mechanism* is present, where the emitted electron's kinetic energy is calculated as:

$$\varepsilon_{\text{kin}}^{ATI} = (n + n') \cdot h\nu - I_p. \tag{3.4}$$

In this case the electron absorbs an $n' \geq 1$ number of excess photons, while in the measured photoelectron spectrum these multiphoton absorptions will appear as evenly spaced peaks separated by the $h\nu$ energy difference. It was observed that by increasing the intensity of the laser field the number of ATI maxima also increases, whilst their height (intensity of maxima) decreases with the photoelectron's energy. However, a plateau (i.e., a region with approximately the same peak heights) is observed in the photoelectron spectrum, which is located in the energy range between two and ten times the ponderomotive energy ($2U_p - 10U_p$). The appearance of this plateau can be explained by the back-scattering of the ejected electrons on the residual ion. Another feature of the ATI spectrum is the suppression of the low order photoelectron peaks with the increase of laser intensity. This property can be explained with the phenomenon known as the *laser induced Stark shift*, where the bound states are dressed with the laser's electric field. Since the Stark shift has little effect on the low-lying bound states, but it modifies significantly the higher level energy states, i.e., it raises the Rydberg and continuum states, the ionization potential is increased. Hence, the lower part of the $n + n'$ photon ionization channels will be significantly emptied, resulting in the decrease of the intensity of low order ATI maxima. Due to this effect, in many occasions the first peak in the spectrum almost vanishes. Although, by taking into account that the intensity profile of the radiation pulse varies smoothly in time, for small time windows the excited states may be Stark shifted into resonance with the ground, therefore the total suppression of the corresponding peaks is avoided.

## Tunneling and over-the-barrier ionization

Until this point in the presented photon-induced processes we assumed hat the laser field does not modify the binding potential (Coulomb field) of the electron. This is valid until the intensity of the radiation field does not approach the intensity associated to the electric

field strength 'felt' by the bound electron: for instance in the case of the hydrogen atom the electric field strength of the binding electron $E_{\mathrm{H}} = e/(4\pi\epsilon_0 a_0^2) \simeq 5.1 \times 10^{19}$ V/m corresponds to the intensity $I_{\mathrm{H}} = (\epsilon_0 c/2)E_{\mathrm{H}}^2 \simeq 3.51 \times 10^{16}$ W/cm$^2$, where $\epsilon_0$ is the vacuum permittivity and $a_0$ is the Bohr radius of the hydrogen atom (according to the definition of the atomic unit of electric field strength and intensity: $E_{\mathrm{H}} = I_{\mathrm{H}} = 1$).

It was shown [30] that if the intensity of the laser field approaches or exceeds the intensity associated to the electric field strength of the bound electron an alternating ionization process takes place. This process can be interpreted classically by taking into account that the effective potential felt by the bound electron can be obtained by adding the electron-laser interaction term to the Coulomb potential:

$$V_{\mathrm{eff}}(\vec{r}) = V_{\mathrm{C}}(\vec{r}) - e\vec{r}\vec{E}(t). \tag{3.5}$$

$V_{\mathrm{eff}}(\vec{r})$ will differ the most from $V_{\mathrm{C}}(\vec{r})$ when the magnitude of the momentary electric field is the highest: $E(t) = \pm E_0$. For the case of the hydrogen atom the form of the modified potential is illustrated along the $oz$ direction in Figure 3.1.

As one can observe the laser-induced suppression of the binding potential takes place and a potential barrier is formed. If the frequency of the laser field is sufficiently low, the electron may escape from the parent ion by tunneling through this barrier. This tunneling process has the highest probability near the peaks of the radiation field, thus in every halc-cycle tunneling photoelectrons will be emitted appearing in the spectrum as periodic electron signals. The process is known as *tunneling ionization* (TI) and it was observed experimentally first in 1974 by using microwave radiations [31]. The TI mechanism represents one of the basis concept for understanding the high harmonic generation of ultrashort attosecond pulses (see the next section) usually obtained for atoms in the gas phase by using coherent radiation fields in the IR regime (typically when $\lambda \geq 800$ nm).

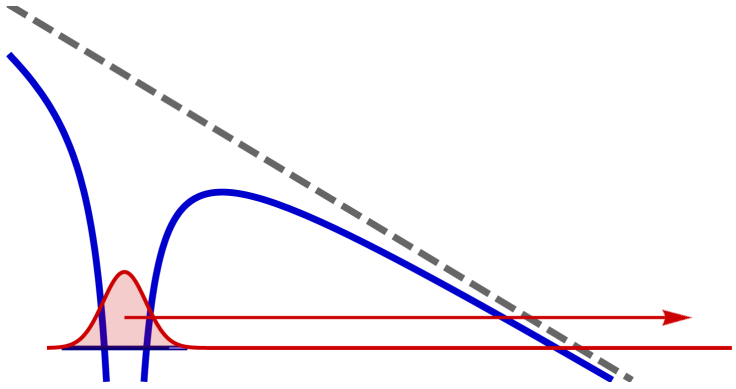

Figure 3.1: The schematic of the the tunnel ionization mechanism. The blue curve illustrates the Coulomb potential of the hydrogen atom modified by the electric component of the laser field. The term describing the interaction between the electron and the external electric field is given by the dashed (dark gray) line. The electron described by the wave function (red curve) may tunnel out through the potential barrier created on the *rhs* of the potential.

Moreover, by further increasing the laser intensity this can reach a critical value when the height of the potential barrier disappears and the electron wave packet can freely "flow" out the parent ion. The process is known as *over-the-barrier* ionization (OBI) and it occurs in atomic targets when the intensity of the radiation field exceeds the critical value of

$$I_{\text{crit}} \left[\frac{\text{W}}{\text{cm}^2}\right] \simeq 4 \times 10^9 \times (I_p[\text{eV}])^4 \, Z^2, \tag{3.6}$$

where $-I_p$ is the energy of the bound state and $Z$ is the charge of the parent ion. For the simplest target, i.e., for the hydrogen atom, the potential barrier is totally suppressed when $I_{\text{laser}} = I_{\text{crit}}^{OBI} \simeq 1.4 \times 10^{14}$ W/cm$^2$.

*The Keldysh parameter*

In order to identify the dominant ionization mechanism that occurs during the interaction between atoms/molecules and external radiation fields, Keldysh introduced a laser and target dependent parameter

$$\gamma = \sqrt{\frac{I_p}{2U_p}} = \frac{\omega}{eE_0}\sqrt{2m_e I_p}, \tag{3.7}$$

which was later named after him, and where the $U_p = e^2E_0^2/4m_e\omega^2$ ponderomotive (quiver) energy of the ejected ("free") electron is calculated as the cycle-averaged energy gained by this from the radiation field having the angular frequency $\omega = 2\pi\nu = 2\pi c/\lambda$ and electric field amplitude $E_0$. The *Keldysh parameter* is used to distinguish the intensity regimes associated with different photoionization processes. When the $\gamma \gg 1$ condition is fulfilled it means that the quiver energy of the continuum electron is much less then the ionization energy of the target and the binding potential is not significantly distorted by the radiation field. In this case the photoemission occurs predominantly via single or multiphoton absorptions. In the other limit, when $\gamma \ll 1$ the wavelength $\lambda$ is large ($\sim$ IR waves) meaning that the period of the laser field $T = \lambda/c$ is also sufficiently large to favorize the quasi-static tunneling photoemission. The transition between the two regimes, i.e., around $\gamma \approx 1$, is a smooth one, since it was observed that by approaching $\gamma$ to 1 starting from the multiphoton regime the ATI peaks start to fade out gradually until they almost completely vanish.

It is worth mentioning though, that apart from the laser field's intensity also the temporal contrast, the duration and the period of the pulse may play an important role for determine which photoemission mechanism will be observed in the experiments to be the dominant one. For instance, it could be a reasonable experimental outcome that even though the intensity of the incident light is situated in the extremely high region, hence by distorting the Coulomb potential it would facilitate photoemission via the tunneling process, the measured spectra will show mainly ATI peaks. This outcome can be easily understood by considering that

almost all the target systems located in the focal volume will be depleted via multi-photon processes by the high intensity radiation field before the electric field reaches its peak value and a potential barrier is created. Hence an ionization saturation occurs below the $I_{\mathrm{crit}}$ value, which can be impeded by using shorter (i.e., ultrashort) pulses.

## 3.2 High Harmonic Generation (HHG)

The *high harmonic generation* (HHG) process is a special and a possible outcome of the laser induced ionization, which enjoys a strong interest in the field of attoscience, namely in the production of high energy (XUV) ultrashort pulses. In this process the laser ejected electron is driven back by the radiation field to the parent ion, where it is reabsorbed, and the energy gained from the EM field during the excursion time is emitted in a form of a high frequency XUV photon (by using an appropriate phase-matching the created photons are coherently added and XUV attosecond pulses are produced).

The essence of the HHG process can be understood most easily in the semi-classical framework using the three-step-model (TSM) proposed by M. Lewenstein [32]. This model which is based on the strong field approximation (SFA) and the single active electron (SAE) approximation, states that in the first step the (active) electron escapes the parent atom/molecule through the potential barrier created by the laser field via the tunneling process. This event is highly probable to take place near the maximum of the external field and the ejected electron appears in the continuum at time $t$ with the kinetic energy $\varepsilon_k = [\vec{k} + \vec{A}(t)]^2/2 + I_p$, where $\vec{k}$ is the kinetic momentum (atomic units were considered: $\hbar = e = m_e = 1$). In the second step the ionized electron is accelerated in the continuum by the oscillating EM field, which as it changes its direction drives back the electron to the parent ion, where a recombination between electron-ion occurs. During this recombination event (third step) the electron is absorbed and emits its energy gained from the driving field in the form of a high energy photon.

Harmonic generation is a nonlinear optical process in which the frequencies of the newly emitted photons - appearing in the measured spectrum - are integer multiples of the $\nu_0$ fundamental frequency. In measurements, where monoatomic gas targets are irradiated with intense monochromatic light pulses due to symmetry considerations only odd integer multiples of $\nu_0$ can be obtained: $\nu_{\mathrm{HHG}} = (2n+1)\nu_0$, where $n$ is a positive integer. This characteristic feature of the HHG spectra for atomic gas can be explained by taking into account the following considerations. In each optical cycle two electron trajectories are responsible for the XUV bursts. The emission of these photoelectrons occurs near the two consecutive extrema of the radiation field via tunnel effect and the moments of recolissions with the parent ion are separated by half of the period of the incident field ($T/2$). In this way the electric fields of the two intracycle emitted XUV pulses were "born" with opposite phases

$$\begin{aligned} E_1^{(\omega)} &= A(\omega)\exp\{i(\omega t + \varphi)\} \\ E_2^{(\omega)} &= A(\omega)\exp\{i[\omega(t - T/2)] + \varphi + \pi\}, \end{aligned} \tag{3.8}$$

and by using that $e^{i\pi} = -1$ the sum of these two fields results in a net electric field of

$$E^{(\omega)} = E_1^{(\omega)} + E_2^{(\omega)} = A(\omega)e^{i(\omega t+\varphi)}\left(1 - e^{-i\omega T/2}\right), \tag{3.9}$$

which vanishes for the case of even $\omega = 2n\omega_0$ harmonics, since $(1 - e^{-i\omega T/2}) = 0$. Thus, in real experiments during the propagation through the active medium these two intracycle waves having opposite phases will cancel out by destructive interference, whereas those having approximately the same phases will be constructively enhanced, giving rise to odd harmonics in HHG spectra obtained for atomic gas targets.

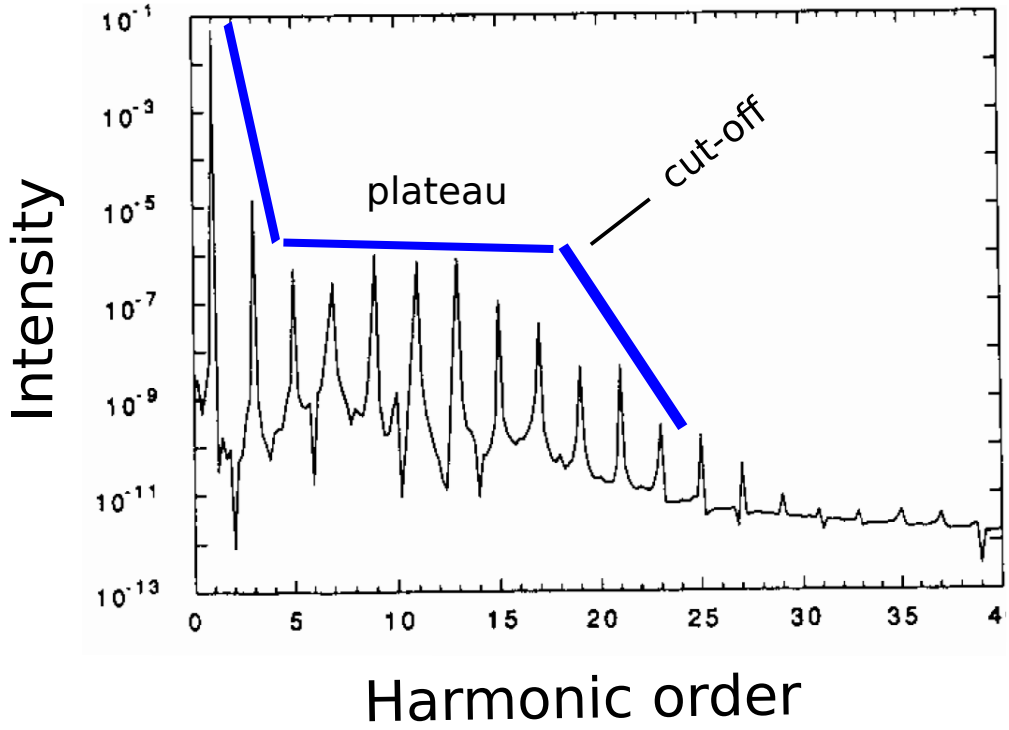


Figure 3.2: The blue solid lines illustrate the typical regions observed for HHG spectra. The presented spectrum was obtained for Xenon target by using a 1064 nm wavelength and $3 \times 10^{13}$ W/cm$^2$ intensity laser adapted from [33].

The typical HHG spectrum (see Fig. 3.2) where the measured (or calculated) intensities are shown at logarithmic scale as a function of harmonic order ($H_{2n+1} = \omega_n/\omega_0$) have three distinctive characteristic regions. For lower photon energies (i.e., the first few harmonics) a rapid decrease of intensity is present. This is followed by a broad *plateau* of many harmonics where the intensities are approximately the same showing a relatively slow decrease. The high energy edge of the HHG spectrum presents an abrupt decrease, where the high harmonics "die out" within a few orders. The photon energy where this downturn takes place is referred to as the *cut-off* energy of the spectrum, and gives the last harmonic (highest photon energy) achievable with a relatively accessible intensity. The main goal of recent studies mainly deals with the extension of the cut-off energy of the HHG spectrum (i.e., obtain the higher and higher energies confined in an ultrashort pulse) by employing new experimental setups, which may be consisted of using two- (or) many-colour lasers, or different target systems

(molecules, metallic nanostructures, etc.) The typical cut-off energy obtained for atomic gasses is around the value $3.17U_p + I_p$, while for gold nanostructures this could have been extended even above $10U_p + 0.538\ W$, where the $W$ work function for gold is 5.1 eV [34]. Considering the achieved extensions of the plateau domain and the recent experimental developments that are able to select a certain harmonic from the train of attosecond bursts, the HHG opened new perspectives in the production of ultrashort coherent XUV and X-ray radiations.

CHAPTER 4.

# Photoelectron holography

By the production of high frequency ultrashort laser pulses laser induced *photoelectron holography* (PEH) has recently emerged as a promising technique for investigating the internal structure of laser irradiated atomic systems. This novel tool exploits the interference between different electronic wave packets (EWPs), which are emitted by the radiation field into the continuum, and where, due to the presence of the oscillating field, they follow different spatial paths. These different paths will lead to different phases accumulated by the ejected EWPs, and the resulted phase differences are detectable in the measured photoelectron spectra (i.e., in the angle-resolved momentum distribution of the ejected electrons) as constructive (maxima) and destructive (minima) interference patterns.

Similarly to the case of its optical analogy, i.e., optical holography [35], the laser induced photoelectron holography [36] captures information regarding the amplitude and phase of the scattered waves, for which in the case of PEH the role of the scattering objects are played by the electrons' parent ion (atom, molecule). However, in contrast with the traditional electron holography, where the electron's are "fired" from an electron gun of an electron microscope and maneuvered by optical (imaging) elements, in the case of PEH the electronic wave packets are the result of some ionization mechanisms induced by an intense (ultrashort) laser pulse, and are manipulated by the electric component of the same oscillating field.

By taking into account, that PEH is a state-of-the-art technique of the continuously developing field of laser science, which became experimentally accessible only in the last few years (first observations were made in 2011 [37]), elaborated theoretical investigations are desired for the deeper understanding of the underlying processes.

The theory behind the creation of PEH can be represented in the simplest way by employing the three-step model, according to which, first, the laser irradiated atomic system emits electronic wave packets into the continuum either by the tunneling or by OBI ionization process. Second, the ionized electron that appears in the continuum at a nonzero distance measured from the nuclei is accelerated away from its parent ion, and as the oscillating field changes its direction, is driven back by this to the vicinity of the ion. Finally, according to the third step, with a given differential cross section the returned EWP may rescatter elastically from the parent cores.

It has to be mentioned though, that a large portion of photoelectrons will miss the parent ion and will not interact or rescatter by this. This can be explained simply by the fact, that the photoelectrons are appearing in the continuum at different phases (different temporal parts) of the radiation field, then are traveling along different trajectories, and those electrons, that have larger transverse momenta will simply avoid the interaction with the ion. Given that the laser initiated continuum electronic waves are fully coherent, in the simplest scenario, the returning and rescattering electronic waves will form a *diffraction pattern*. Since the returning EWP travels in the vicinity of the parent ion, this pattern encodes the spatial information of the local electrostatic field, which is directly connected to the structure of the atomic or molecular target. The resulting diffraction pattern can be used then to recover structural information about the target. This self-imaging technique is known as the *laser-induced electron diffraction* (LIED) and it is analogous to the traditional electron diffraction technique, where high energy electron beams are used to gain structural information about the irradiated, laboratory-prepared samples. In addition to this, LIED can also be used as a high-potential tool for resolving *structural dynamics* of atomic systems. However, considering that the laser-induced electron diffraction is a strong-field process, in order to acquire relevant information about the structural dynamics of the irradiated systems, one has to remove first the influence of the oscillating field from the measured photoelectron spectrum, which can be done only via laborious procedures.

Alongside the LIED process, recent studies [37, 38, 39] have suggested that the well distinguishable radial fringe structures appearing in the photoelectron spectra are the consequence of an alternative (laser induced) process, according to which, the crucial role is played by the phase differences between the EWPs emitted during the same quarter-cycle of the radiation field, but which follow different paths in the continuum. It was shown [37] that the observed radial fringe structures are the consequence of the interference of these continuum EWPs. In [37] it was detailed, that for the appearance of the radial structures, the interference between two distinct EWPs are mainly responsible: the first one is the scattered wave, while the second one is an electronic wave, that is associated with a larger transverse momentum value, which implicitly implies a totally different electron trajectory than the first one. Due to the larger transverse momentum value the recollision to the parent ion of the second EWP is greatly reduced or simply entirely avoided.

Similarly to the traditional holography, where two distinct fully coherent electromagnetic waves are present, i.e., a scattered and a direct wave, in the laser induced PEH a scattered electronic wave interferes with a fully coherent (un- or weakly scattered) direct wave. Hence, the process itself can be considered the laser induced photoelectron holography of the atomic system, and the relevant information about the target may be extracted from the obtained interference pattern created by the (strongly) scattered and unscattered (or weakly scattered) wave. In the PEH the former EWP plays the role of the reference wave, whilst the later one the signal wave.

The photoelectron holography appearing as a secondary process succeeding the primary

(laser induced) ionization of the target arises as a modulation on the ionization probability density (or PES) map obtained for the target. Previous investigations [39] demonstrated that the *spatial interference* of the EWPs detectable in the photoelectron spectra is the result of the superposition of wave packets 'born' approximately at the same time (i.e., during the same quarter-cycle of the laser pulse), but driven by the oscillating field along different paths. During the excursion in the continuum, these EWPs accumulate different phases, which due to the coherent superposition induce the formation of radial ridge structures in the PES [18, 38, 39, 40, 37, 41, 42, 43, 44, 45, 46].

Using classical trajectory Monte-Carlo simulations [43] the assumption according to which two distinct, a direct (unscattered) and a scattered [38, 39, 37], EWP is present in the coherent superposition process was proven to be valid for the case of the hydrogen atom, where it was shown that the electrons can arrive at a given continuum state with a well defined momentum $\vec{k}$ along a weakly scattered and a strongly scattered trajectory. The two distinct trajectories are schematically represented on Figure 4.1.

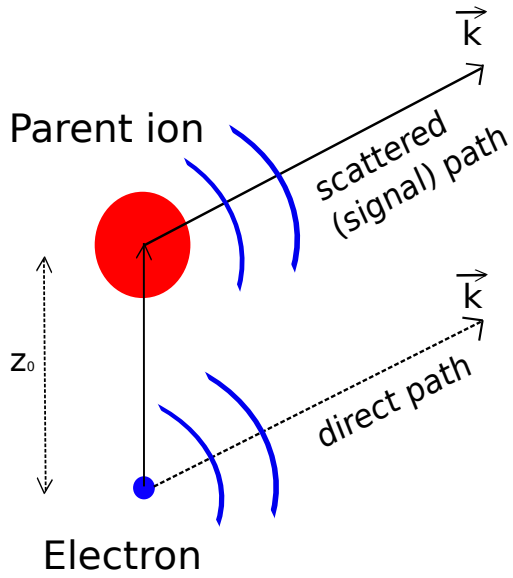


Figure 4.1: The schematics of the scattered and direct electron trajectories.

Calculations were made and it was found that the weakly scattered electron, after it had been driven back by the oscillating field, approached the parent ion to the minimum distance of 5 atomic units; while the strongly scattered electron approached the core more closely, by reaching an $\sim$ 1 a.u. separation distance from this. According to this picture, the weakly scattered EWPs play the role of the reference waves, while the strongly scattered EWPs are part of the signal waves, therefore the spatial interference pattern can be interpreted as the hologram of the irradiated system [37, 43].

It is worth mentioning, that even if both mechanisms of the laser-induced electron diffraction (LIED) [47, 48, 49, 50, 51] and the photoelectron holography are based on the scattering of the EWPs during their quiver motion in the oscillating field on the parent ion, in

the case of the LIED the reference wave is missing. This absence causes the extraction of structural [47, 48, 49, 50] and temporal [51] information regarding the irradiated atom or molecule from the PES resulted from the EWP diffraction (LIED) to be achieved only by laborious procedures [49]. In contrary, due to the existence of a reference wave in the case of PEH, in principle an easier extraction of structural information is possible. In this case the presence of the reference EWP leads to a more structured electron momentum distribution with clearly distinguishable and identifiable interference minima and maxima.

By reviewing the literature of previous experimental [38, 37, 41, 18] and theoretical [43, 52, 53, 44, 45, 46] investigations several aspects of the creation of the photoelectron holograms can be understood. Firstly, it was shown that for a given target the density of the interference minima is determined by the $z_0$ maximum distance measured from the parent ion that the liberated electron reached before the rescattering event. The value of $z_0$ can be directly controlled by the parameters of the driving field, i.e., increasing the wavelength or the intensity of the laser pulse results in an increased $z_0$ value. Secondly, it was recently demonstrated [45] for atomic targets that for a fixed driving field the features of the hologram were strongly influenced by the profile of the scattering potential (i.e., by the atomic species). With real optimism, in the near future it will be possible for experimentalists to take advantage of this high target sensitivity of the PEH and utilize the measured photoelectron momentum distribution maps to identify local potentials inside the laser irradiated samples. It was proven by first principle and classical trajectory calculations [45], that the phase accumulated by the scattered electron is strongly influenced by the depth of the binding potential experienced by the rescattering electron along the returning path.

Besides atomic targets, several studies on the photoelectron holography of molecular targets were also performed [54, 55, 56, 57, 58, 59, 60, 61, 62, 63], a large portion of which were focusing on smaller atomic systems, such as the $H_2^+$ molecule. The physics behind the creation of the photoelectron holograms in molecules and the features appearing in the PES can be more easily understood by investigating less complex targets. The $H_2^+$ molecule gives us the possibility to study the influence of the internuclear distance and the two-center interference of the EWPs on the molecular photoelectron holograms.

A significant portion of $H_2^+$ related works [55, 56, 58, 63] investigated the influence of the molecular axis orientation on the PEH at equilibrium internuclear distance, and found that the forward scattering photoelectron hologram (both the signal and reference wave packets being created during the same quarter cycle of the driver pulse) is only weakly influenced by it. This weak effect was explained by the observation that in the case of small molecules the electron scattering cross section in the forward scattering direction is mainly determined by the long-range Coulomb potential [61, 64] and the short-range effects are repressed by the long range contribution. However, it was later shown that the molecular axis orientation dependence of the forward scattering photoelectron hologram can be increased either by using circularly polarized driving fields [57, 58], or by increasing the molecular axis length [59, 62]. For the backward scattering direction the contribution of the short-range

part of the molecular Coulomb potential is larger, thus - as it was expected - the backward scattering PEH (where the signal and reference wave packets were created during different quarter cycles [54, 61]) is severely affected by the molecular axis orientation [61].

In contrast, investigations on the molecular axis length dependence of the forward scattering photoelectron holography are rather sparse. In [61] the indirect experimental evidence is presented on the molecular axis length dependence of the PEH. Furthermore, in the framework of a simplified model, where the $H_2^+$ was described by a 2D soft-core Coulomb potential, this effect was explicitly studied in [59] and [62]. However, in the first study [59] it is only marginally discussed, while in the second one [62] it is investigated in details only at large internuclear distances (in the region of the charge-resonance enhanced ionization).

In the above outlined context, the second, principal part of the present thesis is mainly dedicated to the investigation of the molecular axis length dependence of the forward scattering photoelectron hologram, where special attention is accorded to the physics of the molecular axis length dependence of the PEH. More precisely, this work concentrates mainly on the investigation of photoelectric holograms appearing as a result of the interaction between ultrashort XUV pulses and the $H_2^+$ target. The main goal was to acquire valuable knowledge regarding how the geometry (the internuclear distance) of the simplest molecule influences the nature of the HM pattern, and to identify the multi-center effects of the molecular binding potential on the holograms, as outlined in the second part of this thesis.

CHAPTER 5.

# Theoretical methods for investigating laser induced electron dynamics

In order to follow our line of inquire, in the following, the two most widely preferred theoretical approaches - used for single active electron calculations - will be briefly presented and each of these theoretical descriptions will be supplemented with results obtained by detailed calculations applied on the simplest target system, i.e., the hydrogen atom. The first approach is a semi-classical method, which is based on the *strong field approximation* (SFA) and where an extension of the simple SFA [32] will be concisely discussed. This method is usually a favored choice due to its simplicity (i.e., it implies computationally cheap calculations) when tunneling ionization and high harmonic spectra have to be calculated, but it is not a convenient approach for exact calculations regarding the ionization rates and electron wave packet dynamics. For these later processes, the second class of methods can be employed, that consists of calculations based on the numerical solution of the *time-dependent Schrödinger equation* (TDSE). Within the TDSE calculations two different procedures will be discussed, namely the direct and the iterative solution of the TDSE, both using a grid representations of the wave function in the momentum space.

## 5.1 Semi-classical approaches: Strong Field Approximation methods

According to the semi-classical picture of the Strong Field Approximation (SFA) [32], when the period of the intense laser field is sufficiently large and its electric field component reaches one of its extrema values (minimum or maximum), due to the high external field strength the deformation of the Coulomb field takes place and a potential barrier is created; through which the active bound electron tunnels out and appears in the continuum at time $t'$ with the energy

$$\mathcal{E}_{\vec{\mathcal{P}}}(t') = \frac{\left[\vec{\mathcal{P}} + \vec{A}(t')\right]^2}{2} + I_p. \tag{5.1}$$

$\vec{\mathcal{P}}$ is the canonical momentum, and by considering atomic units ($q = -|e| = -1$; $\hbar = 1$) the following relation was considered: $-q\vec{A}(t') = \vec{A}(t') = -\int_{-\infty}^{t'} \vec{E}(t'')dt''$. By entering the continuum the electron is treated semi-classically, where the electronic wave function accumulates a phase from the oscillating field, and after the excursion time the electron recollides with the parent ion by being reabsorbed on the ground state of the atom/molecule. The outcome of the reabsorptions are the production of attosecond high harmonic bursts. The time-dependent dipole moment of the electron is used to characterize these laser induced tunneling emission and reabsorption events [32, 65]:

$$\vec{d}(t) = -i \int_{t_0}^{t} \mathrm{d}t' \int \mathrm{d}\vec{k}\; d^*_{\mathrm{rec},\vec{r}}(\vec{k} + \vec{A}(t)) \exp\left[-iS_0(\vec{k}, t, t')\right] d_{\mathrm{ion},\vec{r}}(\vec{k} + \vec{A}(t'), t') + c.c., \quad (5.2)$$

where the second part *c.c.* stands for the complex conjugate of the first part, the substitution $\vec{\mathcal{P}} = \hbar\vec{k} = \vec{k}$ (using atomic units $\hbar = 1$) was considered. The physical interpretation of Eq. (5.2) is the following. First, the electron via the ionization process is ejected from the $|\varphi_0\rangle$ ground state to a continuum state $|\Psi_{\vec{k}}\rangle$ with the probability amplitude for make the transition at time $t'$: $d_{\mathrm{ion},z}(\vec{k} + \vec{A}(t'), t') = \langle\Psi_{\vec{k}}|\hat{U}_{\mathrm{laser}}(t')|\varphi_0\rangle = \langle\Psi_{\vec{k}}|zE(t')|\varphi_0\rangle$. Second, the wave function of the laser driven electron is propagated until the time $t$ in the continuum by neglecting the effects of the Coulomb potential during the short time interval between $t'$ and $t$, during which the wave function acquires a phase factor of $\exp\left[-iS_0(\vec{k}, t, t')\right]$, where the $S_0$ quasi-classical action is given by the following expression

$$S_0(\vec{k}, t, t') = \int_{t'}^{t} \mathrm{d}t'' \left\{ \left[\vec{k} + \vec{A}(t'')\right]^2 /2 + I_p \right\}. \quad (5.3)$$

The above quantity describes the motion of freely moving electron in the laser field with a constant asymptotic momentum $\vec{k}$. In the last step the continuum electron recombines at time $t$ with the parent ion and it gets reabsorbed on its initial ground state with the probability (transition) amplitude $d^*_{\mathrm{rec},z}(\vec{k} + \vec{A}(t)) = \langle\phi_0|-z|\Psi_{\vec{k}}\rangle$. Usually for the $|\Psi_{\vec{k}}\rangle$ continuum states the simple plane waves or the more accurate Volkov states are used.

Since the Eq. (5.2) implies the integration of a highly oscillating function of time, i.e. the exponential form of the semi-classical action, which from the numerical point of view represents a hard task, many calculations are restricted to the so called saddle-point calculations, where only the stationary points of $S_0$ are taking into account in the temporal integration. This approach can be considered valid until the major contribution to the integral over $\vec{k}$ are coming from these $\vec{k}_{st}$ stationary points satisfying the equation

$$\nabla_{\vec{k}} S_0(\vec{k}, t, t')|_{\vec{k}=\vec{k}_{st}} = 0. \quad (5.4)$$

By considering that $\nabla_{\vec{k}} S_0(\vec{k}, t, t')$ gives the difference between the position of the freed electron at time $t$ and $t'$, i.e., $\nabla_{\vec{k}} S_0 = \vec{r}(t) - \vec{r}(t')$ it follows that the stationary points of $S_0$ correspond to those $\vec{k}$ values for which the electron born at time moment $t'$ is redirected to

the same position by the laser field at time $t$ before the reabsorption event.

### 5.1.1 Theory and Results: SFA+ approach for HHG calculations

Until this point within the framework of the simple SFA only the recollision to the ground state was considered, however during the recapture mechanism also the other bound states may play a not negligible role. Moreover, due to the presence of the external field depending on the strength of its electric component the ground and the bound states may be Stark-shifted. In order to take into account these later considerations an extension of the SFA, the SFA+ model, will be shortly discussed, where the saddle-point procedure of the simple SFA is omitted, and the starting point of inquire consists in writing the $i\partial_t\Psi(t) = [\hat{H}_0 + U(t)]\Psi(t)$ TDSE using the Green propagator formalism. By rearranging the terms in the TDSE as

$$\left(i\frac{\partial}{\partial t} - \hat{H}_0\right)\Psi(x) = \hat{U}(x)\Psi(x) \tag{5.5}$$

on the *lhs* one ontains a linear operator $\hat{D} = i\partial_t - \hat{H}_0$, while on the *rhs* $\hat{U}(x)\Psi(x)$ is taken as the source term. Here the $x$ variable denotes all the three spatial and the one temporal coordinate, i.e., $x := \{\vec{r}; t\}$ The solution of this type of equations may be given as:

$$\Psi(x) = \Psi_0(x) + \int \mathrm{d}^4x G^+(x, x')U(x')\Psi(x'), \tag{5.6}$$

where the $G^+(x, x')$ function is the Green propagator, which satisfies the equation $(i\partial_t - \hat{H}_0)G^+(x, x') = \delta^4(x - x')$. By substituting for $\hat{H}_0$ the $\mathcal{E}_0$ ground energy and using the $U_{\text{laser}}(\vec{r}; t) \simeq U(t)$ dipole approximation, the coordinate dependence of the Green propagators will not be taken into account, hence only the following two forms of equations should be solved:

$$\begin{aligned}
[i\partial_t - \mathcal{E}_0]G_0^+(t, t') = \delta(t - t') \quad &\Rightarrow \quad G_0^+(t, t') = -i\theta(t - t')\exp\{-i(t - t_0)\mathcal{E}_0\} \\
\left[i\partial_t - \mathcal{E}_{\vec{k}}(t)\right]G^+(t, t') = \delta(t - t') \quad &\Rightarrow \quad G^+(t, t') = -i\theta(t - t')\exp\left\{-i\int_{t'}^{t}\mathcal{E}_{\vec{k}}(t'')\mathrm{d}t''\right\},
\end{aligned}$$

where $\mathcal{E}_{\vec{k}}(t'') = [\vec{k} + \vec{A}(\tau)]^2/2$ is the instantaneous kinetic energy of the ejected electron in the radiation field, while $\theta(t-t')$ is the step function [$\theta(t-t') = 1$ if $t \geq t'$ and equals 0 otherwise]. Within the present approach the TDSE can be given using the Green's propagators as follows

$$-i|\Psi(t)\rangle = G_0^+(t, t_0)|\Psi(t_0)\rangle + \int_{t_0}^{t}\mathrm{d}t' G^+(t, t')U(t')G_0^+(t', t_0)|\Psi(t_0)\rangle, \tag{5.7}$$

where $U(t) = \vec{A}(t)\cdot\vec{k} + \vec{A}^2(t)/2$ is the electron's interaction with the electromagnetic field in the velocity gauge and dipole approximation. The HHG spectrum can be computed by evaluating the mean value of the $z$ component (linearly polarized field in the $oz$ axis) of the

$\hat{a} = -(q/m_e)\partial V_c/\partial z = \partial V_c/\partial z$ dipole acceleration operator ($m_e = -q = 1$):

$$a(t) = \langle\Psi(t)|\hat{a}|\Psi(t)\rangle \simeq \langle\Psi(t)|\hat{B}\hat{a}|\hat{C}\Psi(t)\rangle + c.c. \tag{5.8}$$

where the HHG pulses are produced via continuum → bound transitions, with $\hat{B} = \sum_b^{\infty}|\varphi_b\rangle\langle\varphi_b|$ and $\hat{C} = \int \mathrm{d}\vec{k}|\vec{k}\rangle\langle\vec{k}|$ being the projection operators onto the bound and continuum states, respectively. By taking into account that the sum of the two projection operators equals the identity operator $\hat{I} = \hat{B} + \hat{C}$ and the commutation relation $\left[\hat{B}, \hat{C}\right]|\Psi\rangle = 0$ next to the equalities $\hat{B}^2 = \hat{B}$, $\hat{C}^2 = \hat{C}$ holds, after introducing the identity operator $(\hat{B} + \hat{C})$ in front of each quantity in Eq. (5.7) one obtains the projections onto the bound and the continuum states

$$-i\hat{B}|\Psi(t)\rangle = G_0^+(t,t_0)|\Psi(t_0)\rangle + \int_{t_0}^{t} \mathrm{d}t'\hat{B}G^+(t,t')\hat{B}U(t')\hat{B}G_0^+(t',t_0)|\Psi(t_0)\rangle \tag{5.9}$$

$$-i\hat{C}|\Psi(t)\rangle = \int_{t_0}^{t} \mathrm{d}t'\hat{C}G^+(t,t')\hat{C}U(t')\hat{B}G_0^+(t',t_0)|\Psi(t_0)\rangle. \tag{5.10}$$

In the deduction of the above equations the commutation relation $[\hat{H}_0, \hat{B}]|\Psi(t)\rangle = 0$ and the good approximation of $[\hat{H}, \hat{C}]|\Psi(t)\rangle \simeq 0$ were also considered. On the other hand, it is worth pointing out that the $\hat{B}U(t)\hat{B}$ operator describes the atomic excitations (note that in the simple SFA there is no ground state dressing, i.e., $\hat{B}U(t)\hat{B} = 0$), while $\hat{C}U(t')\hat{B}$ corresponds for the ionization of the electron. By using the relations in Eqs. (5.9)-(5.10) and following some mathematical steps the acceleration can be deduced as the sum of two interfering contributions

$$a(t) \simeq \langle\Psi(t)|\hat{B}\hat{a}\hat{C}|\Psi(t)\rangle + c.c. = a_b(t) + a_d(t) + c.c., \tag{5.11}$$

where $a_d(t)$ is associated with the transition from the continuum to the field dressed state, while $a_b(t)$ describes the dynamics of the transition between the continuum and the bare atomic ground. The later can be obtained for a well defined momentum $\vec{k}$ solving the deducible differential equation

$$\frac{\mathrm{d}a_b(\vec{k};t)}{\mathrm{d}t} = i\left[\mathcal{E}_0 - \mathcal{E}(\vec{k};t)\right]a_b(\vec{k};t) + iC_F\langle\varphi_0|\hat{a}|\vec{k}\rangle U(\vec{k};t)\langle\vec{k}|V_c|\varphi_0\rangle. \tag{5.12}$$

In the above equation for the case of the hydrogen atom the Coulomb potential $V_c = -1/r$, the Coulomb factor $C_F = [2Z^2/n^2E_0]$ ($n = 1$, $Z = 1$), and $\mathcal{E}(\vec{k},t) = k^2/2 + U(\vec{k};t)$ where $U(\vec{k};t) = A(t)k_z + A^2(t)/2$.

Finally, the net acceleration is calculated (Fig. 5.1) by evaluating the integration of the $a_b(\vec{k};t)$ contributions over all the momentum space:

$$a(t) = -\int \mathrm{d}\vec{k}\ \frac{k^2/2 - \mathcal{E}_0}{\Delta_s(k_z)}a_b(\vec{k},t) + c.c., \tag{5.13}$$

where in the denominator appears the energy levels shift, which is obtained as the time average of the interaction term over the collision time $\Delta_s(k_z) = \langle U(t) \rangle = \delta t_s^{-1} \int_{t-\delta t_s}^{t} U(k_z; t')\mathrm{d}t'$. Here the evaluation of the rescattering time $\delta t_s$ can be roughly approximated by dividing the size of the returning EWP by its velocity at the rescattering instance: considering the initial velocity of the tunnel ionized electron $v_i \simeq \sqrt{2|\mathcal{E}|}$ and multiplying it with the typical time of excursion in continuum $\tau \approx (3/4)T = (3/4)2\pi/\omega_0$ leads to the approximated size of the wave packet $(v_i\tau)$. Hence the time lapse of the rescattering is given by the relation

$$\delta t_s \approx \frac{v_i \tau}{v_{\mathrm{recoll}}} \simeq \frac{3\pi}{2\omega_0} \sqrt{\frac{|\mathcal{E}_0|}{3.17 U_p}}, \tag{5.14}$$

where the reabsorbed electrons have the approximate recolliding velocity of $v_{\mathrm{recoll}} \approx \sqrt{2 \times 3.17 U_p}$.

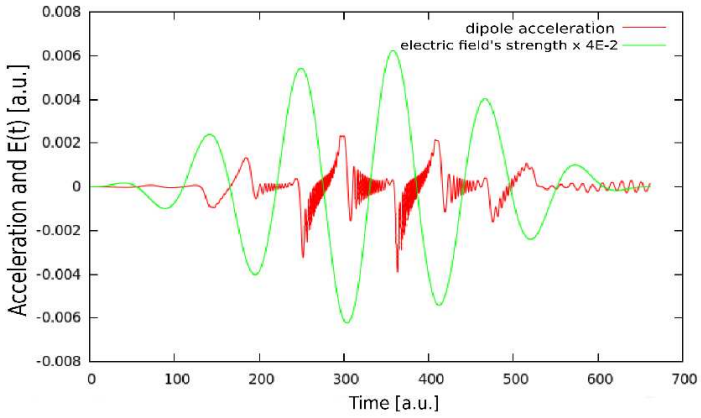


Figure 5.1: The electric field component of the laser field (green curve), and the calculated dipole acceleration (red curve) as a function of time according to Eq. (5.13).

As mentioned earlier in this section the HHG spectrum can be directly calculated from the Fourier transform of the dipole acceleration, which by using Larmor's formula will give the total power radiated by the non relativistic point charge $q$ as it accelerates:

$$P(\omega) = \frac{q^2}{6\pi\epsilon_0 c^3} \mathcal{F}\{a(t)\} = \frac{q^2}{6\pi\epsilon_0 c^3} a^F(w). \tag{5.15}$$

The differential equation (5.12) was solved by using a fourth-order Runge-Kutta method, the integral in Eq. (5.13) evaluated with the Simpson method for different laser pulse wavelengths, intensities, and pulse shapes (sinusoidal, Gaussian), and the spectra calculated according to the Larmor's formula are shown in Figure 5.2.

In subfigures Figure 5.2/(a)-(b) it can be observed that by increasing the amplitude of the radiation field strength also the plateau of the spectra increases. This is explained by the fact that for larger $E_0$ the electron acquires higher energy from the laser field prior to the recollision event. By comparing the subfigures 5.2/(a) and (b) one can observe that, when the wavelength is larger [i.e., 800 nm in subfigure (b)] higher harmonics are achieved,

since the cut-off energy of the 800 nm occurs between the 130 and 140 harmonic orders, whilst in the first case [i.e., 600 nm in subfigure (a)] this is located between low orders, 50 and 60. This dependence on the wavelength is further evidenced by plotting in subfigure 5.2/(c) the HHG spectra for fixed field intensity (electric field amplitude $E_0 = 0.2$ a.u.) but for different central wavelengths $\lambda$. It can be obviously observed that by increasing $\lambda$ the electron's ponderomotive energy $U_p$ also increases, since the high energy electrons are driven at larger maximum distance from the parent ion, thus there excursion time is increased, and they can gain more energy from the radiation field. [1]

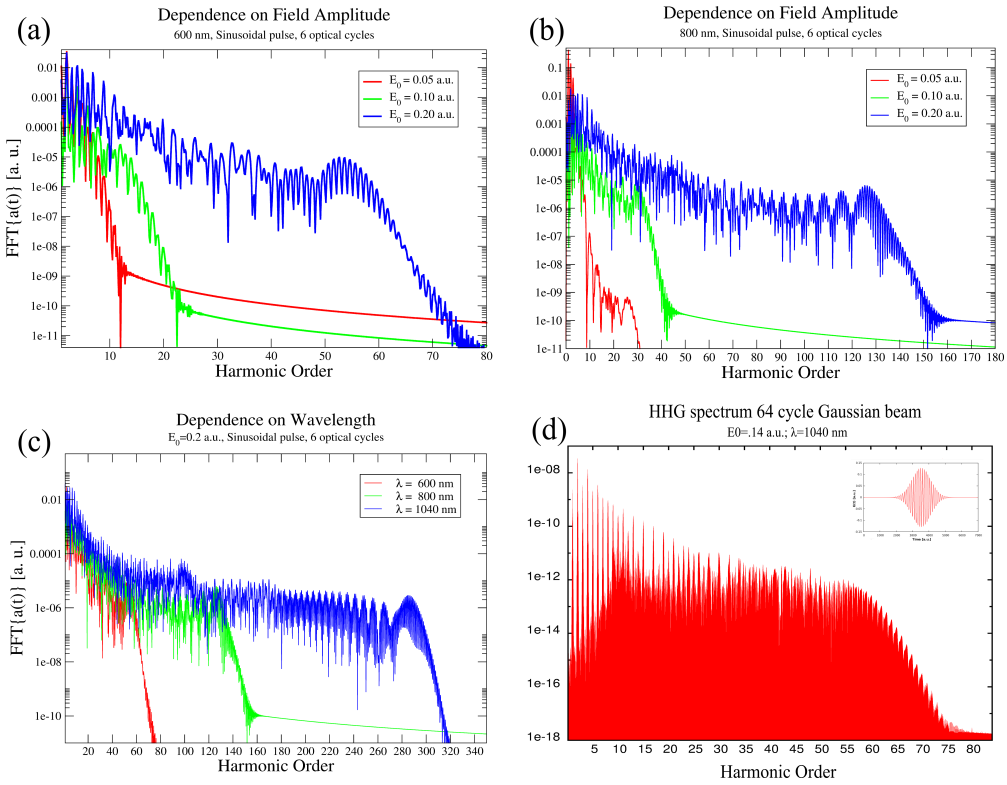


Figure 5.2: High harmonic spectra for the hydrogen atom using sinusoidal envelope pulses (a)-(c) and a Gaussian profile beam (d) for different laser field parameters. Sub-figures (a) and (b) show the cut-off order dependence of the plateau on the electric field's amplitude for a 6 cycle pulse having the central wavelength of 600 nm and 800 nm, respectively. On subfigure (c) for a fixed intensity the HHG spectra dependence as a function of radiation wavelength is illustrated. In subfigure (d) the harmonic response of a 64 cycle Gaussian beam is shown ($E_0 = 0.14$ a.u.; $\lambda = 1040$ nm).

[1] The results obtained by the implementation of the SFA+ method were presented and discussed at several international scientific meetings (conference poster presentations):
G. Zs. Kiss, K. Kovács, V. Toşa, *Laser - atom interaction beyond the strong field approximation model*, Processes in Isotopes and Molecules (PIM) 11th International Conference, Cluj-Napoca, Romania, 27-29 Sep (2017).
G. Zs. Kiss, V. Toşa, K. Kovács, *Theoretical Investigation Beyond the Strong Field Approximation Model*, TIM17 Physics Conference, Timioara, Romania, 25-27 May (2017).
G. Zs. Kiss, K. Kovács, V. Toşa, *Numerical investigations beyond the SFA model*, MEDEA Summer School: Ultrafast Dynamics with Intense Radiation Sources, Crete, Greece, 18-22 Oct. (2016).

## 5.2 Methods for the solution of the time-dependent Schrödinger equation (TDSE)

The most accurate results for the investigation of laser-matter interactions can be obtained by solving the time-dependent Schrödinger equation (TDSE). Since, even for the simplest case - hydrogen atom in external radiation field - there is no analytical solution, the only possible way remains the numerical integration of TDSE. Due to the high computer time and memory requirements needed by the numerical time propagation of the time dependent wave function (TDWF), this method is principally employed when the single active electron approximation may be safely considered. For multi-electron systems which interact with intense fields other methods should be employed, which are mostly based on the time-dependent density functional theory (DT-DFT).

In this section, first, the various types of wave function representations will be presented, which will be followed by a short overview of different time propagation methods that can be applied for the electronic TDWF. In the section's last part two distinct methods will be given for the numerical solution of TDSE: a direct and the iterative solution of the Shrödinger equation, both calculating the wave function in momentum space. The benchmark of the methods will be presented for the simplest target, the hydrogen atom.

### 5.2.1 Representation of the wave function

#### Spectral representation

When the solutions of time-dependent Schrödinger equation should be obtained it is a well established method to express the unknown wave function describing the particle and the operators assigned to physical quantities in terms of a complete set of functions, i.e., so-called *basis-functions*. Considering this, the wave function in coordinate space may be expressed as

$$\Psi(\vec{r};t) = \sum_{m=1}^{\infty} \varphi_m(\vec{r}) c_m(t) \tag{5.16}$$

where the $\{\varphi_m\}$ represent the basis functions, and the $c_m(t)$ expansion coefficients can be calculated by multiplying the above expression with $\varphi_n^*(\vec{r})$ and integrating over $\vec{r}$ as follows:

$$\int_{\vec{r}} \varphi_n^*(\vec{r})\Psi(\vec{r};t)\mathrm{d}\vec{r} = \sum_{m=1}^{\infty} c_n(t) \int_{\vec{r}} \varphi_n^*(\vec{r})\varphi_m(\vec{r})\mathrm{d}\vec{r} = \sum_{m=1}^{\infty} S_{nm} c_m(t). \tag{5.17}$$

The $S_{mn}$ values are the elements of the so-called *overlap matrix* built from the basis-functions, and in cases when the used $\{\varphi_n\}$ functions form an orthonormal set, i.e., $S_{mn} = \delta_{mn}$ the calculation of the expansion coefficients is reduced to

$$c_n(t) = \langle \varphi_n | \Psi(t) \rangle = \int_{\vec{r}} \varphi_n^*(\vec{r})\Psi(\vec{r};t)\mathrm{d}\vec{r}. \tag{5.18}$$

From the computational point of view, by taking into account the impossibility of handling infinite number of basis functions, the expansion of the *exact* wave function has to be truncated at $N < \infty$, and the wave function written as

$$\Psi(\vec{r};t) \simeq \sum_{n=1}^{N} \varphi_n(\vec{r}) c_n(t), \tag{5.19}$$

This approach is called as a finite basis representation (FBR), when the dynamics taking place in the Hilbert space, which is complete for $N \to \infty$, is reduced to an $N$-dimensional subspace. The subspace needs to be "complete" enough in order to represent the whole dynamics of the system, which can be achieved by choosing wisely when the appropriate set of the basis functions is selected, and by increasing the dimensionality $N$ of the subspace till convergence in the dynamics is reached. Using the projection operator $\hat{P}_N = \hat{P}_N^\dagger = \sum_{n=1}^{N} |\varphi_n\rangle\langle\varphi_n|$ which projects the quantum state $|\Psi\rangle$ of the Hilbert space onto the $N$-dimensional subspace as $|\Psi\rangle_N \to \hat{P}|\Psi\rangle$, and the Hamiltonian as $\hat{H}_N \to \hat{P}_N \hat{H} \hat{P}_N^\dagger$, the time-dependent Schrödinger equation reads as:

$$\begin{aligned} &i\frac{\partial}{\partial t}|\Psi(t)\rangle_N = \hat{H}_N|\Psi(t)\rangle_N \Rightarrow \\ &i\frac{\partial}{\partial t}\sum_{n=1}^{N}|\varphi_n\rangle\langle\varphi_n|\Psi(t)\rangle = \sum_{l=1}^{N}\sum_{m=1}^{N}\sum_{n=1}^{N}|\varphi_l\rangle H_{lm}(t)\langle\varphi_m|\varphi_n\rangle\langle\varphi_n|\Psi(t)\rangle \end{aligned} \tag{5.20}$$

where the notation

$$H_{lm} = \langle\varphi_l|\hat{H}(t)|\varphi_m\rangle \tag{5.21}$$

was used. By projecting Eq. (5.20) onto $|\varphi_k\rangle$ and using the expression (5.18) next to the orthonormal condition

$$\langle\varphi_k|\varphi_n\rangle = \langle\varphi_k|\hat{I}|\varphi_n\rangle = \int \mathrm{d}\vec{r}\langle\varphi_k|\vec{r}\rangle\langle\vec{r}|\varphi_n\rangle = \int \mathrm{d}\vec{r}\varphi_k^*(\vec{r})\varphi_n(\vec{r}) = \delta_{kn} \tag{5.22}$$

one can obtain a set of coupled differential equations for the $c_k(t)$ expansion coefficients

$$i\frac{\mathrm{d}}{\mathrm{d}t}c_k(t) = \sum_{m=1}^{N} H_{km}(t)c_m(t), \tag{5.23}$$

By calculating the $c_k(t)$ time-dependent coefficients the solution of the TDSE is obtained according to the expression (5.19), where the $\varphi_k(\vec{r})$ functions can be, in principle, any kind of functions that form a basis: e.g., eigenfunctions of the $\hat{H}_0$ Hamiltonian, Slater type orbitals (STO), or analytical polynomial functions such as the Laguerre, Hermite, Lagrange or Legendre polynomials. A favored choice is the use of the eigenfunctions of the field-free Hamiltonian ($\psi_k \equiv \varphi_k$), since in this case the matrix elements of the Hamiltonian are

calculated as

$$H_{km}(t) = \langle\psi_k|\hat{H}_0 + \hat{U}_{\rm int}(t)|\psi_m\rangle = \epsilon_m\delta_{km} + \langle\psi_k|\hat{U}_{\rm int}(t)|\psi_m\rangle, \tag{5.24}$$

where $\epsilon_m$ is the eigenenergy corresponding to the $|\psi_m\rangle$ eigenstate of $\hat{H}_0$, and the contributions from the field-free part are obtained exactly.

The ***discrete variable representation*** (DVR) method is related to the spectral representation of the wave function. In coordinate space a wave function in its spectral representation is written as

$$\Psi(\vec{r}) = \langle\vec{r}|\Psi\rangle = \sum_{m=1}^{N}\langle\vec{r}|\varphi_m\rangle\langle\varphi_m|\Psi\rangle = \sum_{m=1}^{N} a_m\langle\vec{r}|\varphi_m\rangle, \tag{5.25}$$

where the expansion coefficients

$$a_m = \langle\varphi_m|\Psi\rangle = \int\langle\varphi_m|\vec{r}\rangle\langle\vec{r}|\Psi\rangle\mathrm{d}\vec{r} \tag{5.26}$$

describe the wave function, and the $\{|\varphi_m\rangle\}$ is an orthonormalized basis of Hilbert space (usually it is complete when $N \to \infty$). The basis functions satisfy the orthonormal relation:

$$\langle\varphi_m|\varphi_n\rangle = \int\langle\varphi_m|\vec{r}\rangle\langle\vec{r}|\varphi_n\rangle d\vec{r} = \delta_{nm}. \tag{5.27}$$

Using the Shrödinger equation one may derive from the Rayleigh-Ritz variational principle the following matrix eigenvalue problem:

$$\sum_{m=1}^{N}\hat{\mathcal{H}}_{nm}a_m = a_n E, \tag{5.28}$$

which can be solved once the $\hat{\mathcal{H}}_{nm} = \langle\varphi_n|\hat{\mathcal{H}}|\varphi_m\rangle$ matrix elements have been calculated. Since $N < \infty$ the eigenvalues of Eq. (5.28) will always represent an upper bound to the true solution for $N \to \infty$. The main idea of the DVR is to choose a basis for which the overlap integrals in (5.27) can be evaluated *exactly by numerical quadratures*. The classical orthogonal polynomials up to order $N-1$ fulfill this requirement. For each of these basis sets, there is an associated Gaussian quadrature of order $N$ in which the product of two of these functions can be integrated exactly.

First let the integration be only in one dimension ($\vec{r} \to x$). It can be easily proven that the product of two of these functions is at most of $(2N-2)^{th}$ order, which may be integrated exactly by an $N^{th}$ order quadrature at grid points $x_k$ with weights $w_k$. According to this idea, the integral (5.26) for the case of one dimension is replaced with the sum:

$$\tilde{a}_m = \sum_{j=1}^{N} w_j\langle\varphi_m|x_j\rangle\langle x_j|\Psi\rangle, \tag{5.29}$$

and the DVR remains orthonormal under the quadrature rule $\langle\varphi_m|\varphi_n\rangle = \sum_{j=1}^{N}\langle\varphi_m|x_j\rangle\langle x_j|\varphi_n\rangle = \delta_{nm}$. An important advantage of these representations is that the potential operator matrix is diagonal

$$\hat{V}_{nm} = \langle\varphi_m|\hat{V}|\varphi_n\rangle = \int \varphi_m^*(x)V(x)\varphi_n(x)dx \approx \sum_j^N w_j\varphi_m^*(x_j)V(x_j)\varphi_n(x_j). \tag{5.30}$$

For the case $\{\varphi_m(x)\} \rightarrow \{f_i(x)\}$, where $f_j(x_i) = \delta_{ij}/\sqrt{w_i}$, while the $\{f_i(x)\}$ DVR basis remains orthonormal, since

$$\langle f_i|f_j\rangle = \int f_i^*(x)f_j(x)dx \stackrel{!}{=} \sum_{m=1}^{N} w_m f_i^*(x_m)f_j(x_m) = \delta_{ij}. \tag{5.31}$$

By introducing Eq. (5.29) into the one dimensional case of Eq. (5.25) one obtains for the 1D wave function the following expression

$$\Psi(x) = \langle x|\Psi\rangle = \sum_{m=1}^{N}\tilde{a}_m\langle x|\varphi_m\rangle \approx \sum_{m=1}^{N}\sum_{j=1}^{N} w_j\langle x|\varphi_m\rangle\langle\varphi_m|x_j\rangle\langle x_j|\Psi\rangle. \tag{5.32}$$

From here by imposing that $\langle x|\Psi\rangle = \sum_{j=1}^{N}\langle x|f_j\rangle\langle f_j|\Psi\rangle$ the DVR basis functions are obtained as $f_j(x) = \sqrt{w_j}\sum_{m=1}^{N}\langle x|\varphi_m\rangle\langle\varphi_m|x_j\rangle$, and the wave function simply expressed as

$$\Psi(x) = \langle x|\Psi\rangle = \sum_{j=1}^{N}\langle x|f_j\rangle\langle f_j|\Psi\rangle = \sum_{j=1}^{N}\tilde{\Psi}_j f_j(x), \tag{5.33}$$

where the $\tilde{\Psi}_j = \langle f_j|\Psi\rangle$ coefficients are connected to the values of the wave function via $\tilde{\Psi}_j = \sqrt{w_j}\Psi(x_j)$. The coefficients of the basis functions $f_j$ give the values of the wave function at the grid points in coordinate space, which are the quadrature points of the underlying Gaussian quadrature. A consequence of this, is that the coordinate operator is diagonal in the DVR basis:

$$\langle f_i|\hat{x}|f_j\rangle = \delta_{ij}x_i. \tag{5.34}$$

Such a DVR basis is efficiently represented by an interpolating polynomial, which for a given order is unique and can be expressed by using Lagrange polynomials:

$$P_i(x) = \prod_{j\neq i}\frac{x - x_j}{x_i - x_j}, \quad \text{with} \quad P_i(x_j) = \delta_{ij}, \tag{5.35}$$

and $f_j(x) = P_j(x)/\sqrt{w_j}$. The main advantage is that the potential matrix will remain diagonal within the accuracy of the quadrature approximation

$$V_{ij} = \langle f_i|\hat{V}|f_j\rangle \stackrel{!}{\approx} V(x_i)\delta_{ij}, \tag{5.36}$$

and the action of a linear operator, e.g., an n$^{th}$ order derivation operator of the form $\hat{D} = \partial^n/\partial x^n$, on the wave function can be calculated in an efficient way as

$$\hat{D}\Psi(x) = \frac{\partial^n \Psi(x)}{\partial x^n} = \sum_{j=1}^{N} \tilde{\Psi}_j \frac{\partial^n f_j}{\partial x^n}(x), \tag{5.37}$$

since the action of $\hat{D}$ (e.g., the derivatives) on the basis functions have to be computed only once at the start of the time propagation of the TDSE.

### Grid representation

The grid methods are related to the spectral representation (presented in the previous subsections) in the sense that for the basis functions the $\delta(\vec{r}' - \vec{r})$ Dirac delta functions can be introduced, and since the $\vec{r}$ coordinates are continuum variables, the wave function is given in the integral form as

$$\Psi(\vec{r}) = \int \mathrm{d}\vec{r}' \ \Psi(\vec{r}')\delta(\vec{r}' - \vec{r}). \tag{5.38}$$

In real physical systems the $\Psi(\vec{r})$ wave function describing an electron, an atom, or a group of atoms has an infinite extent and an exponentially decaying behavior at infinities. This implicitly means that practically the wave function itself is mainly constraint in a finite volume around the nuclei. Resulting from the interaction with an external radiation field the wave function spreads out in the space and reaches far distances measured from the origin (the central of mass of the target system). However, this extent of the laser driven wave function can be estimated by knowing the field's parameters. Accordingly, in computer simulations where handling infinities is impossible, the configuration space need to be truncated at certain values: e.g., when Cartesian coordinate representation is used the $\vec{r} \to \{x, y, z\}$ coordinates are chosen from the well defined intervals $x \in [x_{\min}, x_{\max}], y \in [y_{\min}, y_{\max}], z \in [z_{\min}, z_{\max}]$. These considered intervals should take into account the laser induced dynamics of the system, as already pointed out a few lines earlier, while the used truncations will mean that the whole dynamics is investigated inside a simulation "box" or grid. Not only the size of the grid, but also the density (the distance between the gridpoints) can play a crucial role in wave packet dynamics, since the higher components of the wave function can be resolved by using higher grid densities. If both the size and density of the simulation grid is the appropriate one (the calculated wave functions converged), one may safely consider the use of wave function's grid representation at this given set of gridpoints,

$$\Psi(\vec{r}) \to \Psi \simeq [\Psi(r_1), \Psi(r_2), \ldots, \Psi(r_N)]^T \tag{5.39}$$

where the $r_1$, $r_2$, ..., $r_N$ points are usually distributed on an equidistant grid[2].

[2]However, in principle the gridpoints can be placed in any fashion inside the simulation box.

Next to the wave function the Hamiltonian of the system should be also discretized, which depending on the chosen gauge and the nature of the problem, typically contains operators depending only on the coordinate itself, or operators which imply first or second order derivations. One of the main advantage of the grid approach is that the coordinate operators and any function of it can be expressed by simple diagonal matrices. However, the representation of operators containing any order of derivation is not straightforward, and the n$^{th}$ order derivative of the wave function in a given point $r_i$ can be approximated by the values of the wave function in the neighbouring gridpoints: $\{\Psi(r_{i\pm1}), \Psi(r_{i\pm2}), \dots\}$. This approximations can be done within the framework of the *finite difference* method developed by Euler.

In this simple and frequently used ***finite difference*** (FD) method the coordinates are placed on an equally-spaced grid

$$r_i = r_1 + (i-1)\cdot\Delta r, \quad i = \overline{1,N}, \tag{5.40}$$

where the grid spacing is defined as $\Delta r = (r_N - r_1)/(N-1)$. In order to evaluate the derivation of the wave function in a given $r_i$ gridpoint, first the Taylor expansion of $\Psi$ around $r_i$ evaluated in the neighboring points is employed

$$\begin{aligned}
\Psi(r_{i+1}) &= \Psi(r_i) + \delta r\Psi^{'}(r_i) + \frac{\delta r^2}{2}\Psi^{''}(r_i) + \frac{\delta r^3}{6}\Psi^{'''}(r_i) + \dots \\
\Psi(r_{i-1}) &= \Psi(r_i) - \delta r\Psi^{'}(r_i) + \frac{\delta r^2}{2}\Psi^{''}(r_i) - \frac{\delta r^3}{6}\Psi^{'''}(r_i) + \dots
\end{aligned} \tag{5.41}$$

By subtracting the above two equations and using the discrete value $\Delta r \leftarrow \delta r$, the first order derivation of the wave function in the $r_i$ gridpoint can be deduced as

$$\Psi^{'}(r_i) = \frac{\Psi(r_{i+1}) - \Psi(r_{i-1})}{2\Delta r} - \mathcal{O}(\Delta r^2\Psi^{'''}(r_i)), \tag{5.42}$$

whilst by adding them together, the second order derivation is obtained as a *three point central difference* formula:

$$\Psi^{'}(r_i) = \frac{\Psi(r_{i+1}) - 2\Psi(r_i) + \Psi(r_{i-1})}{\Delta r^2} - \mathcal{O}(\Delta r^4\Psi^{(4)}(r_i)). \tag{5.43}$$

As one can see, these two operators can be represented by tridiagonal matrices, which from the numerical point of view means that the amount of computations needed for differentiating the wave function is significantly reduced. However, the accuracy of this method is a low one. This can be improved either by increasing the grid density (i.e., decreasing $\Delta r$), or by using higher order formulas (i.e, five, seven, nine, etc), which on the other hand will diminish the sparseness of the Hamiltonian matrix.

### 5.2.2 Temporal propagation algorithms for the wave function

The time evolution of a quantum system is described by the $\Psi(\vec{r}) \rightarrow \Psi(\vec{r};t)$ time dependent wave function, which is governed by the time-dependent Shrödinger equation (TDSE)

$$i\frac{\partial}{\partial t}\Psi(\vec{r};t) = \hat{\mathcal{H}}(t)\Psi(\vec{r};t), \tag{5.44}$$

where atomic units [$\hbar = e = m_e = 1/(4\pi\epsilon_0) = 1$] were used, $\hat{\mathcal{H}}(t)$ is the time-dependent Hamiltonian of the system, and the initial state of the wave function $\Psi(\vec{r};t=0) \equiv \Psi_0(\vec{r})$ is usually known (or in certain circumstances it has to be determined as well). By using the assumption that in a short time interval $(t, t' = t + \delta t)$ the Hamiltonian does not change too much, i.e., $\delta\hat{\mathcal{H}}(t) \sim 0$, the formal solution of the TDSE on this small interval reads as:

$$\Psi(\vec{r};t' = t + \delta t) = \hat{U}(t',t)\Psi(\vec{r};t) = e^{-i(t'-t)\hat{\mathcal{H}}(t)}\Psi(\vec{r};t), \tag{5.45}$$

where $\hat{U}(t',t) = \hat{U}(t+\delta t, t) = \exp\{-i\hat{\mathcal{H}}(t)\delta t\}$ is the *evolution operator*, that describes the time evolution of the wave function.

The widely used temporal propagation methods differ from each other by the way they approximate the evolution operator. In the following a few of these commonly used methods will be concisely given.

#### Explicit and implicit Euler methods

The starting point of this method consists in the Taylor expansion of the evolution operator

$$\hat{U}(t+\Delta t, t) \simeq \exp\left(-i\Delta t\hat{\mathcal{H}}(t)\right) = \sum_{n=0}^{\infty}\frac{1}{n!}\left(-i\Delta t\hat{\mathcal{H}}(t)\right)^n. \tag{5.46}$$

By retaining only the first order term from this Taylor expansion one obtains the Euler propagator form for $\hat{U}$:

$$\hat{U}(t+\Delta t, t) \approx \hat{I} - i\Delta t\hat{\mathcal{H}}(t) \tag{5.47}$$

This scheme is referred to as the *explicit* (or forward) Euler method since the wave function at time $t + \Delta t$ is obtained explicitly from the wave function at a previous time moment $t$. Applying Eq. (5.47) on the wave function one obtains:

$$\Psi(\vec{r};t+\Delta t) = \Psi(\vec{r};t) - i\Delta t\hat{\mathcal{H}}(t)\Psi(\vec{r};t) + \mathcal{O}(\Delta t^2\hat{\mathcal{H}}(t)^2) \tag{5.48}$$

The main advantage of this approach lies in its simplicity. Although, it also has several disadvantages: it is unstable (i.e., if $\Delta t$ is not sufficiently small the high energy components of the wave function tend to blow up exponentially), it is not unitary (i.e. it does not conserves the norm of the wave function), which makes it unfeasible for application. This instability can be improved by considering the inverse time propagation from the time $t + \Delta t$ to $t$, and

the unitary property of the evolution operator $\hat{U}(t+\Delta t,t)=\hat{U}(t,t+\Delta t)^{-1}=\hat{U}(t,t+\Delta t)^{\dagger}$.

$$\begin{aligned}\hat{U}(t,t+\Delta t)\Psi(\vec{r};t+\Delta t) &= \Psi(\vec{r};t)\Rightarrow \\ \Psi(\vec{r};t+\Delta t) &= \left[\hat{I}+i\Delta t\hat{\mathcal{H}}(t)\right]^{-1}\Psi(\vec{r};t)\end{aligned} \tag{5.49}$$

The above expression is known as the *implicit* (or backward) Euler method, which gives a numerically more stable approach than the previous scheme, although computationally it is more expensive since in every time propagation step it involves a matrix inverse calculation.

**Crank-Nicolson (CN) scheme**

Another preferred implicit propagation scheme is the Crank-Nicolson (CN) approach, for which the unitary time propagation is obtained by combining a forward and a backward propagation to an intermediate state at $t+\Delta t/2$:

$$\begin{aligned}\Psi\left(\vec{r};t+\frac{\Delta t}{2}\right) &= e^{-i\frac{\Delta t}{2}\mathcal{H}(t)}\Psi(\vec{r};t) \\ \Psi\left(\vec{r};t+\frac{\Delta t}{2}\right) &= e^{i\frac{\Delta t}{2}\mathcal{H}(t+\Delta t)}\Psi(\vec{r};t+\Delta t)\end{aligned} \tag{5.50}$$

By assuming that $\mathcal{H}(t)\approx\mathcal{H}(t+\Delta t)$, and performing the Taylor expansion for both the operators of Eq. (5.50), the CN time propagator is obtained as

$$\Psi(\vec{r};t+\Delta t)\simeq\hat{U}^{CN}(t+\Delta t,t)\Psi(\vec{r};t)=\frac{\left[\hat{I}-i\frac{\Delta t}{2}\hat{\mathcal{H}}(t)\right]}{\left[\hat{I}+i\frac{\Delta t}{2}\hat{\mathcal{H}}(t)\right]}\Psi(\vec{r};t). \tag{5.51}$$

The main advantage of the CN approach is that it is unconditionally stable and unitary. Though, its main drawback feature is that each time step requires the calculation of the matrix inverse $\left[\hat{I}+i(\Delta t/2)\hat{\mathcal{H}}(t)\right]^{-1}$, which is a computationally time consuming procedure.

**Lie-Trotter-Suzuki product formula (LTSPF) and Split-operator method**

The main idea behind this method lies the division of the Hamiltonian into two parts $\hat{\mathcal{H}}(t)=\hat{\mathcal{H}}_1+\hat{\mathcal{H}}_2$, where $\hat{\mathcal{H}}_1$ and $\hat{\mathcal{H}}_2$ not necessarily commute. In the first order approximation the evolution operator $\hat{U}(t,t+\Delta t)=\exp\{-i\Delta t(\hat{\mathcal{H}}_1+\hat{\mathcal{H}}_2)\}$ reads as

$$\hat{U}_1(t,t+\Delta t)=e^{-i\Delta t\hat{\mathcal{H}}_1}e^{-i\Delta t\hat{\mathcal{H}}_2}, \tag{5.52}$$

while in the second order is given by

$$\begin{aligned}\hat{U}_2(t,t+\Delta t) &= \hat{U}_1^T\left(t,t+\frac{\Delta t}{2}\right)\hat{U}_1\left(t,t+\frac{\Delta t}{2}\right)= \\ &= \exp\left(-i\frac{\Delta t}{2}\hat{\mathcal{H}}_2\right)\exp\left(-i\Delta t\hat{\mathcal{H}}_1\right)\exp\left(-i\frac{\Delta t}{2}\hat{\mathcal{H}}_2\right).\end{aligned} \tag{5.53}$$

Even higher order approximations can be introduced for the LTSPF approach, however for now we may stop at this level without discussing the higher order terms, since already the second order is unconditionally stable and unitary.

The second order of the LTSPF is referred to as the *split-operator method*, where usually the time dependent Hamiltonian is partitioned into a part which contains the momentum of the target ($\hat{\mathcal{H}}_{\vec{p}}$) and a second part which contains operators depending only on the coordinate ($\hat{\mathcal{H}}_{\vec{r}}$). A straightforward partitioning choice using coordinate representation is the kinetic energy operator term and the second term containing all potential energy operators: $\hat{\mathcal{H}} = \hat{\mathcal{T}} + \hat{\mathcal{V}}(t)$, i.e., $\hat{\mathcal{H}}_1 = \hat{\mathcal{T}}$ and $\hat{\mathcal{H}}_2 = \hat{\mathcal{V}}(t)$.

According to this approach, the split-operator propagator has the following form

$$\hat{U}^{split}(t + \Delta t, t) = e^{-i\frac{\Delta t}{2}\hat{\mathcal{V}}(t)} e^{-i\Delta t\hat{\mathcal{T}}} e^{-i\frac{\Delta t}{2}\hat{\mathcal{V}}(t)} \tag{5.54}$$

which is applied on the $\Psi(\vec{r}; t)$ wave function according to the following steps: (i) first, the rightmost diagonal $e^{-i\frac{\Delta t}{2}\hat{\mathcal{V}}(t)}$ is applied on $\Psi(\vec{r}; t)$; (ii) the obtained wave function is transformed into momentum space by using fast Fourier Transform (FFT); (iii) the diagonal $e^{-i\Delta t\hat{\mathcal{T}}}$ in momentum space is then applied on the momentum space wave function; (iv) the new momentum space wave function is transformed back into coordinate space; (v) finally, the leftmost $e^{-i\frac{\Delta t}{2}\hat{\mathcal{V}}(t)}$ diagonal is applied.

### 5.2.3 Direct solution of the TDSE (in momentum space)

The most accurate results can be achieved by the direct solution of the TDSE [66], i.e., by the temporal propagation of the wave function. The time-dependent wave function which satisfies the TDSE

$$i\frac{\partial}{\partial t}\Psi(\vec{r};t) = \left[\frac{\hat{\mathcal{P}}^2}{2} + \hat{U}_{\rm int}(t) + V(\vec{r})\right]\Psi(\vec{r};t), \tag{5.55}$$

can be expressed in terms of the Volkov wave functions

$$\Psi(\vec{r};t) = \int \mathrm{d}\vec{k}\; c(\vec{k};t)\Psi_V(\vec{k},\vec{r};t), \tag{5.56}$$

where $\vec{k}$ is the momentum of the electron, $c(\vec{k};t)$ are the expansion coefficients in the basis of the Volkov wave functions ($\Psi_V$). Within the dipole approximation [$\vec{A}(\vec{r};t) \approx \vec{A}(t)$, and $\vec{E}(t) = -(\mathrm{d}/\mathrm{d}t)\vec{A}(t)$] the Volkov wave functions are the solutions of the TDSE for a charged particle in a radiation field:

$$i\frac{\partial}{\partial t}\Psi(\vec{k},\vec{r};t) = \left[\frac{\hat{\mathcal{P}}^2}{2} + \vec{r}\cdot\vec{E}(t)\right]\Psi_V(\vec{k},\vec{r};t), \tag{5.57}$$

where we have used that the laser-electron interaction term in the dipole approximation reads as $\hat{U}_{\rm int} = \vec{r}\cdot\vec{E}(t)$. The Volkov wave functions [as the solutions of Eq. (5.57)] have the following analytical form:

$$\Psi_V(\vec{k},\vec{r};t) = \exp\left\{-\frac{i}{2}\int_0^t \left[\vec{k}+\vec{A}(t')\right]^2 \mathrm{d}t' + i\left[\vec{k}+\vec{A}(t)\right]\cdot\vec{r}\right\}, \tag{5.58}$$

where the vector potential of the electromagnetic field is calculated as $\vec{A}(t) = -\int_0^t \mathrm{d}t'\vec{E}(t')$. Finally, after introducing the analytical form of the Volkov wave functions into Eq. (5.56), and the expression of the time-dependent wave function into the TDSE (5.55), by performing some basic algebraic calculations the following coupled integro-differential equation for the expansion coefficients can be obtained

$$\begin{aligned}\frac{\partial c(\vec{k};t)}{\partial t} &= \frac{\exp\{\frac{i}{2}[k^2 t + 2\vec{k}\cdot\vec{F}(t)]\}}{i(2\pi)^3}\int \mathrm{d}\vec{k}' c(\vec{k}';t)\exp\left\{\frac{-i}{2}[k'^2 t + 2\vec{k}'\cdot\vec{F}(t)]\right\}\times \\ &\times \int \mathrm{d}\vec{r}\, V(\vec{r})\exp\{i(\vec{k}'-\vec{k})\cdot\vec{r}\},\end{aligned} \tag{5.59}$$

where $\vec{F}(t) = \int_0^t \mathrm{d}t'\vec{A}(t')$.

*The direct - momentum space - TDSE method for the hydrogen atom*

As the simplest benchmark of the numerical method the single electron system - i.e., the

hydrogen atom - may be considered, in the case of which the Coulomb potential is spherically symmetrical: $V(\vec{r}) = -1/r$, and its Fourier transform [last integral of Eq. (5.59)] can be evaluated analytically:

$$\int \mathrm{d}\vec{r}\, V(\vec{r}) \exp\{i(\vec{k'} - \vec{k}) \cdot \vec{r}\} = \frac{-4\pi}{(\vec{k'} - \vec{k})^2}. \tag{5.60}$$

Equation (5.59) can be solved numerically in 3 dimensions, where $c(\vec{k};t) \equiv c(k_x, k_y, k_z; t)$, and given in the explicit form as

$$\begin{aligned} \frac{\partial c(k_x, k_y, k_z; t)}{\partial t} &= \frac{-i}{(2\pi)^3} \exp\left\{ \frac{i}{2} \left[ (k_x^2 + k_y^2 + k_z^2)t + 2k_z F(t) \right] \right\} \times \\ \times \iiint \mathrm{d}k'_x \mathrm{d}k'_y \mathrm{d}k'_z &\frac{c(k'_x, k'_y, k'_z)}{\exp\left\{ \frac{i}{2} \left[ (k_x'^2 + k_y'^2 + k_z'^2)t + 2k'_z F(t) \right] \right\}} \left( \frac{-4\pi}{(\vec{k'} - \vec{k})^2} \right), \end{aligned} \tag{5.61}$$

where $\{k_x,\ k_y,\ k_z\}$ are the Cartesian coordinates of the momentum.

### 5.2.4 Iterative solution of the TDSE (in momentum space)

At the basis of the iterative solution of the TDSE (iTDSE model) lies the momentum-space strong-field approximation (MSSFA) method [67]. In the MSSFA the Coulomb potential is considered only as a first order perturbation next to the laser-electron interaction and the electron's kinetic energy term. It was shown for the case of the hydrogen atom [67, 68] that the MSSFA approach is reliable only when half-cycle laser pulses are considered. As long as it provided accurate results in the halc-cycle regime, it totally failed for many-cycle radiation fields. This failure is the direct consequence of the non-unitary time-propagation of the wave function, which is manifested in an erroneous electron dynamics making the MSSFA model (as a first order perturbation approach) unreliable.

The iTDSE method is an extension of the MSSFA, and can be interpreted as a high order perturbation model. It implies the gradual introduction of higher order terms till convergence is achieved. By the introduction of sufficiently high perturbation terms, in order to acquire accurate results comparable with the experimental data and with the results obtained by the numerical integration of the TDSE, it may represent an alternative tool to the 'exact' solution.

The starting point of the iTDSE method corresponds with the first step of the momentum space TDSE (presented in the previous subsection), and the time-dependent wave function is expressed in the basis of the Volkov wave functions [the same expression as Eq. (5.56)]:

$$\Psi = \int \mathrm{d}\vec{k}\ c(\vec{k};t) \Psi_{\mathrm{V}}(\vec{k}, \vec{r}; t),$$

where $\vec{k}$ is the momentum of the electron, $c(\vec{k};t)$ represent the expansion coefficients, and $\Psi_{\mathrm{V}}$ the Volkov wave functions as the exact solutions of the TDSE for the charged particle

in radiation fields. The coupled differential equation

$$\frac{\partial c(\vec{k};t)}{\partial t} = \frac{\exp\{\frac{i}{2}[k^2 t + 2\vec{k}\cdot\vec{F}(t)]\}}{i(2\pi)^3} \int \mathrm{d}\vec{k}' c(\vec{k}';t) \exp\left\{\frac{-i}{2}[k'^2 t + 2\vec{k}'\cdot\vec{F}(t)]\right\} \times \\ \times \int \mathrm{d}\vec{r}\, V(\vec{r}) \exp\{i(\vec{k}'-\vec{k})\cdot\vec{r}\}, \tag{5.62}$$

which was derived from the TDSE [ $i(\partial/\partial t)\Psi = \hat{H}\Psi$] by basic algebraic calculation may be written formally as:

$$c^{(n)}(\vec{k};t) = c^{(n)}(\vec{k};t_s) + \int_{t_s}^{t} \mathrm{d}t' \frac{\exp\{\frac{i}{2}[k^2 t' + 2\vec{k}\cdot\vec{F}(t')]\}}{i(2\pi)^3} \times \\ \times \int \mathrm{d}\vec{k}' c^{(n-1)}(\vec{k}';t') \exp\left\{\frac{-i}{2}[k'^2 t' + 2\vec{k}'\cdot\vec{F}(t')]\right\} \mathcal{F}(\vec{k}',\vec{k}), \tag{5.63}$$

where $\vec{F}(t) = \int_0^t \mathrm{d}t' \vec{A}(t')$ with $\vec{A}(t) = -\int_0^t \mathrm{d}t' \vec{E}(t')$ being the vector potential in dipole approximation, and the notation $\mathcal{F}$ was used to represent the Fourier transform of the $V(\vec{r})$ Coulomb potential [i.e., the last integral of Equation (5.62)], which couples the different expansion channels $c(\vec{k})$. The positive integer $n$ represents the order of the solution of the iTDSE model, where the $c^{(n)}(\vec{k})$ solution depends on the values calculated for all momentum $\vec{k}'$ in the previous iteration step: $c^{(n-1)}(\vec{k}')$. The exponential terms in Equation (5.63) may be grouped together inside a $Q(\vec{k},\vec{k}',t)$ function such that the time-dependent part become separated according to

$$c^{(n)}(\vec{k};t) = c^{(n)}(\vec{k};t_s) + \int \mathrm{d}\vec{k}' \mathcal{F}(\vec{k},\vec{k}') c^{(n-1)}(\vec{k}';t_s) \int_{t_s}^{t} \mathrm{d}t' \exp\{iQ(\vec{k},\vec{k}',t)\}, \tag{5.64}$$

where it was considered that $c^{(n-1)}(\vec{k}';t) \simeq c^{(n-1)}(\vec{k}';t_s)$ was time invariant between $t_s$ and $t$.

The main task of this method is the efficient calculation of the last integral, since $Q(t)$ is a highly oscillatory function of time. In order to overcome this unpleasant difficulty from the numerical point of view, and to reduce the computer time of the calculations an efficient procedure was developed [68], which will be briefly presented here in the following lines for the case of the hydrogen atom as the target of the laser field.

### *The iTDSE method for the hydrogen atom*

In the case of the hydrogen atom the function $\mathcal{F}$ related to the Fourier transform of the $V(\vec{r}) = -1/r$ Coulomb potential reads as

$$\mathcal{F}(\vec{k},\vec{k}') = -4\pi/(\vec{k}'-\vec{k})^2. \tag{5.65}$$

By taking into account the possibility to reduce the dimensionality (3D $\rightarrow$ 2D) of the studied

system, i.e., the interaction of a linearly polarized laser pulse [$\hat{\epsilon} \equiv (0, 0, \epsilon_z = 1)$] with the electron being initially in its spherical symmetric $1s$ ground state, the two momentum vectors in Cartesian coordinates may be transformed into the cylindrical coordinate system as:

$$\begin{aligned} \vec{k} &\rightarrow (k_x = k_\rho, k_y = 0, k_z) \\ \vec{k}' &\rightarrow (k'_x = k'_\rho \cos\varphi_{k'}, k'_y = k'_\rho \sin\varphi_{k'}, k'_z) \end{aligned} \tag{5.66}$$

where by considering the reduced dimensionality the momentum $\vec{k}$ becomes defined only in the $x0\rho$ plane, while the integration over $\mathrm{d}\vec{k}'$ should be done all over the 3D momentum space. Considering this, the expression for $\mathcal{F}$ leads to:

$$\mathcal{F}(\vec{k}, \vec{k}') = -4\pi/(\vec{k}'^2 + \vec{k}^2 - 2k_\rho k'_\rho \cos\varphi_{k'} - 2k_z k'_z). \tag{5.67}$$

By knowing that the volume element of the cylindrical coordinate system is given as $\mathrm{d}\vec{k}' = k'_\rho \mathrm{d}k_\rho \mathrm{d}k_z \mathrm{d}\varphi_{k'}$, the integration over $\varphi_{k'}$ can be performed as

$$\overline{\mathcal{F}} = \int_0^{2\pi} \mathrm{d}\varphi_{k'}\ \mathcal{F}(\vec{k}, \vec{k}') = \frac{-8\pi^2}{\sqrt{(k'_\rho - k_\rho)^2 + (k'_z - k_z)^2}\sqrt{(k'_\rho + k_\rho)^2 + (k'_z - k_z)^2}}. \tag{5.68}$$

As one can observe in the expression Eq. (5.67) of the Coulomb potential's Fourier transform a singularity occurs when $\vec{k}' = \vec{k}$. This can be treated numerically by introducing a small $\alpha \rightarrow 0$ parameter into Eq. (5.69):

$$\overline{\mathcal{F}}_\alpha(k_\rho, k_z, k'_\rho, k'_z) = \lim_{\alpha\to 0} \frac{-8\pi^2}{\sqrt{(k'_\rho - k_\rho)^2 + (k'_z - k_z)^2 + \alpha^2}\sqrt{(k'_\rho + k_\rho)^2 + (k'_z - k_z)^2 + \alpha^2}} \tag{5.69}$$

leading to the final form of the 2D TDSE:

$$\begin{aligned} c^{(n)}(k_\rho, k_z; t) = c^{(n)}(k_\rho, k_z; t_s) \ &+ \ \int_{-\infty}^{\infty} \mathrm{d}k'_z \int_0^{\infty} \mathrm{d}k'_\rho\ k'_\rho\ \overline{\mathcal{F}}_\alpha(k_\rho, k_z, k'_\rho, k'_z) c^{(n-1)}(k'_\rho, k'_z; t_s) \times \\ &\times \ \int_{t_s}^{t} \mathrm{d}t' \exp\{iQ(k_\rho, k_z, k'_\rho, k'_z; t)\}. \end{aligned} \tag{5.70}$$

As it was already mentioned earlier the most resource consuming task is to calculate the highly oscillating temporal integral [i.e., the last integral of Eq. (5.70)]. In order to facilitate the solution of this problem we proposed a method, where we transformed the problem of the numerical integration into a problem of solving a linear system of equations by using the Levin's method [69], which involves the solution of a smooth Ordinary Differential Equation (ODE). By introducing the constant function $f(t) = 1$, the temporal integral may be given

in the following form:

$$\int_{t_s}^{t} \mathrm{d}t' \; f(t)e^{iQ(t)} = \int_{t_s}^{t} \mathrm{d}t' \left[w(t)e^{iQ(t)}\right]' = w(t)e^{iQ(t)} - w(t_s)e^{iQ(t_S)}, \tag{5.71}$$

and from the simple relation of $f(t)e^{iQ(t)} = \left[w(t)e^{iQ(t)}\right]'$ is it straightforward that

$$e^{iQ(t)}\left[w'(t) + iw(t)Q'(t) - f(t)\right] = 0 \quad \overset{\text{hence}}{\Longrightarrow} \quad w'(t) + iw(t)Q'(t) = 1. \tag{5.72}$$

The values of $w(t)$ satisfying the above ODE have to be obtained in the limits of $\{t_s, t\}$. This can be done by expanding

$$w(t) = \sum_{j=1}^{\mathrm{N_{quad}}} \alpha_j P_j(t) \tag{5.73}$$

in the basis built from the Lagrange-polynomials $P_j(t) = \prod_{k\neq j}^{\mathrm{N_{quad}}}(t - t_k)/(t_j - t_k)$ defined on the $t_1, t_2, \ldots, t_{\mathrm{N_{quad}}}$ Gauss-Lobatto quadrature points, and by solving the linear system of equation obtained for the $\alpha_j$ expansion coefficients

$$\sum_{j=1}^{\mathrm{N_{quad}}} \alpha_j \left[P_j'(t) + iQ'(t)P_j(t)\right] = 1. \tag{5.74}$$

In this way, the values $w(t)$ and $w(t_s)$ obtained in a relative short time, as well as the value of the temporal integral of the rapidly oscillating function [Eq. (5.71)].

### 5.2.5 Comparison of the implemented TDSE methods

In order to compare the results obtained by using the previously presented, different, TDSE methods, for the laser radiation the simplest target - the hydrogen atom - was considered, and the laser field described by an ultrashort half-cycle "quick" pulse, the electric component of which is given analytically with the expression

$$E(t) = \begin{cases} E_0 \sin\left(\omega t + \varphi_0\right) \sin^2\left(\frac{\pi t}{\tau}\right), & \text{if } t \in [0, \tau], \\ 0, & \text{otherwise,} \end{cases} \tag{5.75}$$

where $\tau = 5$ a.u. (pulse duration), $\omega = 0.05$ a.u., and $\phi_0 = -\omega\tau/2 - \frac{\pi}{2}$. The temporal profile and the Fourier transform of the pulse is illustrated in Figure 5.3.

First, the results obtained with the momentum-space strong field approximation (MSSFA) and the iterative solution of the TDSE is compared, by carefully analysing the numerical convergence of the wave function. In Figure 5.4 the norms of the wave function as a function of propagation time for different laser field amplitudes are plotted. As one can observe the norm calculated by the MSSFA and the low order iteration procedures is not conserved - i.e., it increases rapidly - suggesting that these approaches are not reliable when considering intense laser fields. This behaviour is obvious given that the MSSFA is a first order per-

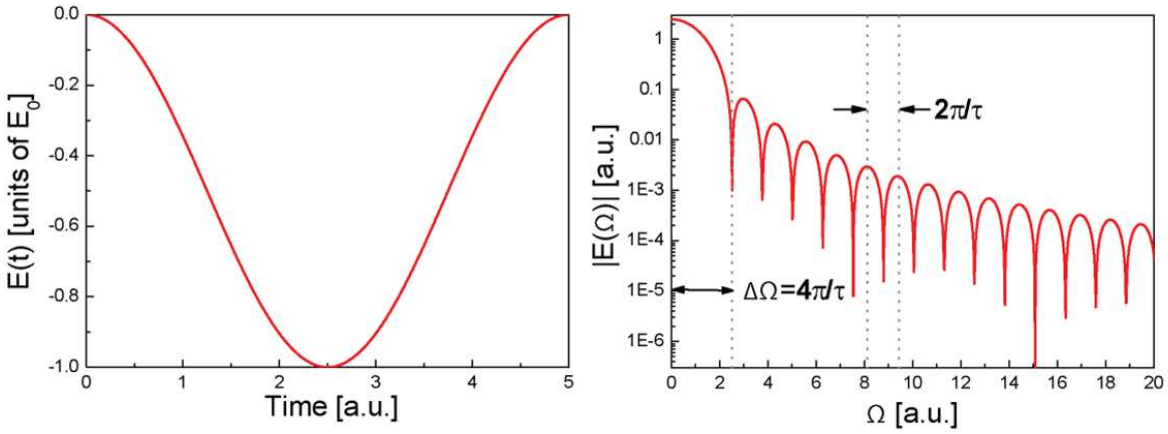


Figure 5.3: The temporal profile of the half-cycle pulse (left) and its Fourier transform (right). $E_0 = 1$ a.u., $\omega = 0.05$ a.u., $\tau = 5$ a.u., $\phi_0 = -\omega\tau/2 - \pi/2$.

turbative method, which inherently results in a non unitary time propagation. However, by increasing the iteration steps, i.e., introducing and approaching higher order perturbation terms, the norm gets closer and closer to the exact (desired) value of 1. Starting from the $4^{th}$ iteration step practically the norm is already near the value 1.

Further investigations were done by calculating the occupation probabilities (OPs) of different bound states at the end of the laser pulse ($t = \tau$). Figure 5.5/(a) shows these quantities obtained with the MSSFA ($1^{st}$ order iTDSE) and higher order iTDSE calculations, next to the data acquired by solving directly the TDSE. A good agreement for the first 8 bound states of the hydrogen atom was found between the results obtained with the $10^{th}$ order iteration and the exact TDSE, suggesting the iTDSE as a possible alternative tool for the direct solution of the Schrödinger equation. Since the iTDSE model is practically a high order perturbation approach, by the inclusion of sufficiently high order terms similar results to the direct solution's can be obtained.

The laser induced ionization probability densities are obtained by projecting the time-

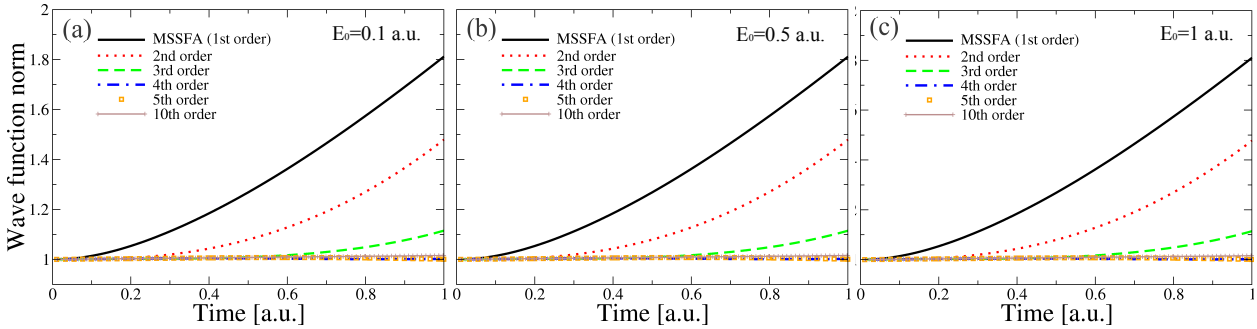


Figure 5.4: The norm of the hydrogen atom wave function calculated for different iterative orders (MSSFA and iTDSE model) as a function of time and field amplitudes: (a) $E_0 = 0.1$ a.u., (b) $E_0 = 0.5$ a.u., (c) $E_0 = 1$ a.u.. The parameters of the ultrashort laser field: the pulse duration $\tau = 1$ a.u., the carrier angular frequency $\omega = 0.05$ a.u..

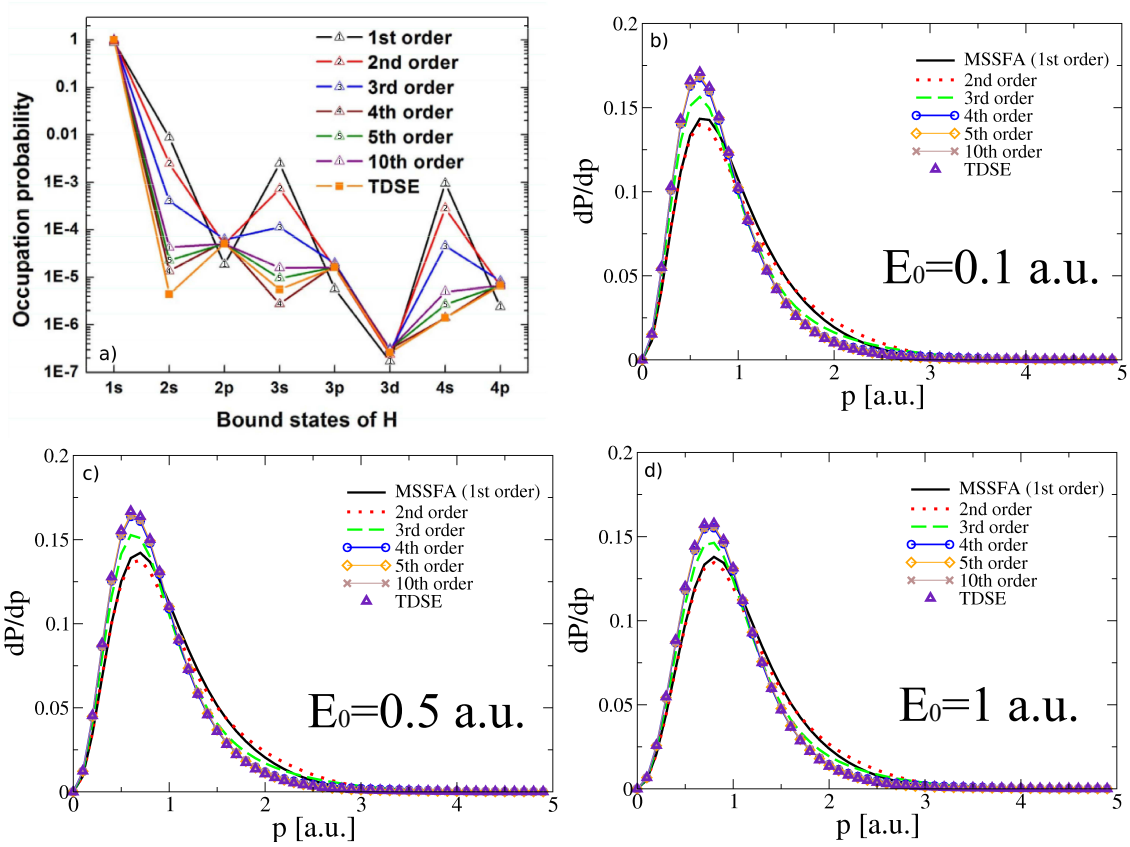


Figure 5.5: The occupation probability of different electronic bound states calculated at $t = \tau$ (a); the ejected electron spectra as a function of electron momentum for different field amplitudes (laser intensities): (b) $E_0 = 0.1$ a.u.; (c) $E_0 = 0.5$ a.u; (d) $E_0 = 1$ a.u..

dependent wave function onto the continuum states with momentum $\vec{k}$:

$$\frac{\mathrm{d}P}{\mathrm{d}\vec{k}}(\vec{k}) = \left|\langle\psi_{\vec{k}}(\vec{r})|\Psi(\vec{r};t)\right|^2. \tag{5.76}$$

These $\psi_{\vec{k}}(\vec{r})$ continuum states may be described by approximate wave functions (i.e., plane waves) or by the exact Coulomb functions. In Figure 5.6 the electron spectra calculated for different continuum state representation is plotted. By comparing the results obtained with the direct TDSE (TDSE model) propagated wave function projected onto the exact scattering states (Coulomb functions: TDSE-C model) with the reference data found in the literature [70], a very good agreement was found. However the convergent iTDSE approach gave very similar results for high energy electrons even when the continuum states were represented by the simple plane waves. An unphysical behavior (a shoulder-like feature) at low electron energies was observed, which is due to the fact that the final wave functions still had contributions from the bound states at the end of the laser pulse, and these remnant contributions are not orthogonal to the plane waves. This unphysical feature was eliminated after removing (by the application of the Gram-Schmidt procedure) the bound states from the final wave function (TDSE-O model). In the Volkov approach the interaction with the parent ion was neglected $[V(\vec{r}) \to 0]$ next to the interaction with the intense radiation field,

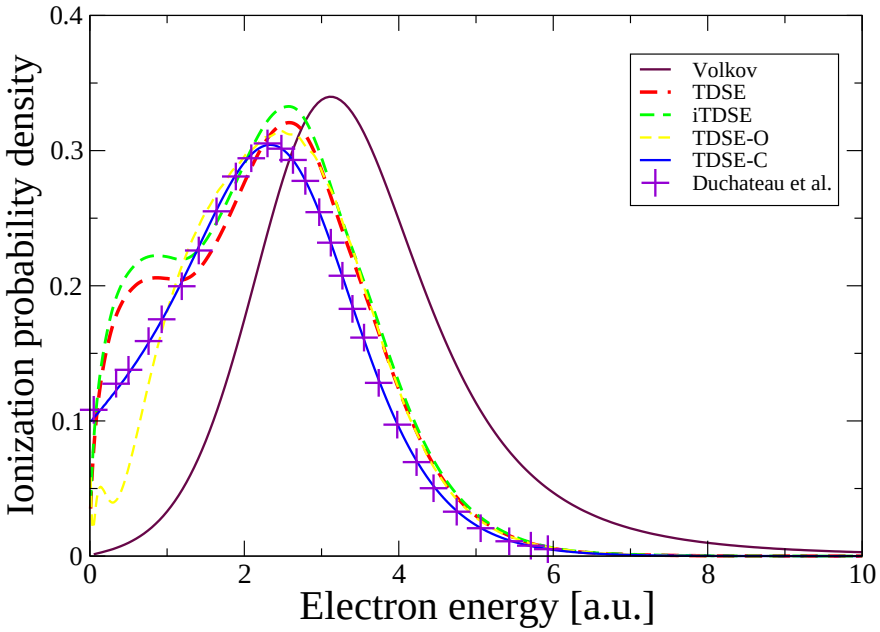


Figure 5.6: The ionization probability density as a function of ejected electron energy calculated at the end of the laser pulse using different TDSE methods. The parameters of the laser field are: $\tau = 5$ a.u., $E_0 = 1$ a.u., $\omega = 0.05$ a.u..

and by applying this approximate method only qualitatively similar results were obtained to the the exact ones (those obtained by the direct solution of the TDSE).

Detailed theoretical descriptions regarding the results obtained for the hydrogen atom by using the presented TDSE methods were presented at several international conferences and published in the following articles [3].

[3]Publications:
ISI articles:
G. Zs. Kiss, S. Borbély, L.Nagy, *Momentum Space Iterative Solution of the Time-Dependent Schrödinger Equation*, AIP Conf. Proc. **1564**, 78 (2013).
S. Borbély, G. Zs. Kiss, L. Nagy, *The Excitation and Ionization of the Hydrogen Atom In Strong Laser Fields*, Central European Journal of Physics **8**, 249 (2010).

BDI article:
Kiss Gellért Zsolt *et al.*, (in Hungarian) *"Numerikus módszerek intenzív lézertér és atomok közötti kölcsönhatás elméleti tanulmányozására"*, Conf. proc.: "A fizika, matematika és művészet találkozása az oktatásban, kutatásban" / ISBN 978-963-284-346-9, ELTE TTK (2013).

International conference (oral presentation):
G. Zs. Kiss, S. Borbély, L. Nagy, *The Numerical Solution of The Time-Dependent Schrödinger Equation for Atoms in Intense Laser Fields*, PHYSICS CONFERENCE TIM-12 organized by the West University of Timişoara, 27-30 November 2012, Timişoara, Romania

CHAPTER 6.

# TDSE for diatomic molecules

The interaction between an external laser field and a diatomic molecule considered with a single active electron (SAE) can be accurately investigated by solving the molecular time-dependent Schrödinger equation (TDSE) [71]:

$$i\frac{\partial}{\partial t}\Psi_{\rm mol}(\vec{r},\vec{R};t) = \hat{H}_{\rm mol}(t)\Psi_{\rm mol}(\vec{r},\vec{R};t) = \left[\hat{H}^0_{\rm mol} + \hat{H}^{\rm int}_{\rm mol}(t)\right]\Psi_{\rm mol}(\vec{r},\vec{R};t), \tag{6.1}$$

where $\Psi_{\rm mol}(\vec{r},\vec{R};t)$ represents the molecular wave function in the coordinate space, $\vec{r}$ is the electron's position vector, $\vec{R}$ represent the nuclear coordinates, and $\hat{H}_{\rm mol}(t)$ is the time-dependent Hamiltonian. The Hamiltonian has a field-free part ($\hat{H}^0_{\rm mol}$) and a time-dependent term, which describes the interaction with the external laser field: $\hat{H}^{\rm int}_{\rm mol}(t)$. The contributing parts are discussed in more details in the following sections.
Throughout this work atomic units were considered (see Appendix I.) !

## 6.1 The Hamiltonian

### 6.1.1 The field-free Hamiltonian

First, let us focus our attention on the field-free part of the molecular Hamiltonian. As it is well known from elementary quantum mechanics [72], the time-independent Hamiltonian of a diatomic molecule having a single active electron may be separated into two main contributions: a nuclear part and an electronic part:

$$\hat{H}^0_{\rm mol}(t) = \hat{H}^0_n + \hat{H}^0. \tag{6.2}$$

The nuclear part ($\hat{H}_n$) can be given as the sum:

$$\hat{H}^0_n = \left(-\frac{\nabla^2_R}{2M_{\rm A}} - \frac{\nabla^2_R}{2M_{\rm B}}\right) + \frac{Z_{\rm A}Z_{\rm B}}{R}, \tag{6.3}$$

where the terms in the parenthesis describe the kinetic energies of the two nuclei having masses $M_{\rm A}$ and $M_{\rm B}$, respectively; $\nabla_R = \partial/\partial\vec{R}$ is the nabla operator, while the second (last) term of Eq. (6.3) is the Coulomb potential describing the electrostatic repulsion between

the two positively charged nuclei, having net electric charges $Z_{\rm A} > 0$ and $Z_{\rm B} > 0$. $R$ is the nuclear coordinate and represents the internuclear separation.
The electronic part can be given as:

$$\hat{H}^0 = \hat{T} + \hat{V}, \tag{6.4}$$

where $\hat{T}$ is the kinetic energy operator of the electron, while $\hat{V}$ describes the Coulomb attraction between the electron and the two nuclei:

$$\hat{T} = \frac{p^2}{2\mu} = \frac{-\nabla^2}{2\mu} \tag{6.5}$$

$$\hat{V} = \hat{V}_{\rm A} + \hat{V}_{\rm B} = -\frac{Z_{\rm A}}{r_{\rm A}} - \frac{Z_{\rm B}}{r_{\rm B}}. \tag{6.6}$$

In the case of multi-electron molecular system, within the SAE approximation model $\hat{V}$ becomes a pseudopotential, that also includes the shielding of the nucleus by the rest of the electrons. In Eqs. (6.5) and (6.6) the values $r_{\rm A}$ and $r_{\rm B}$ represent the distances of the electron measured from the two nuclei, while $\mu$ is the reduced mass of the system: $\mu = (m_e)M/(m + M) \simeq m_e$, where $M = M_{\rm A} + M_{\rm B}$, and $m_e$ represents the mass of the electron.

### 6.1.2 Interaction with the laser field

In the present work I considered the interaction between few-cycle (ultrashort) XUV laser fields and a diatomic molecule ($H_2^+$). For this case the Born-Oppenheimer approximation [73] can be safely applied, thus the electronic and nuclear dynamics can be separated according to

$$\Psi_{\rm mol}(\vec{R}, \vec{r}; t) = \Psi^{\{\vec{R}\}}(\vec{r}; t)\chi(\vec{R}; t), \tag{6.7}$$

where $\Psi^{\{\vec{R}\}}(\vec{r}; t) \rightarrow \Psi(\vec{r}; t)$ is the electronic wave function, $\chi(\vec{R})$ represents the nuclear wave function, $\vec{r}$ is the position vector of the active electron, and $\vec{R}$ represent the nuclear coordinates.

Furthermore, the fixed nuclei approximation (fixed $R$) was considered since the vibrational period ($\sim 10^4$ a.u.) of the target is much larger than the duration of the considered driving field (i.e., 28.26 a.u.), thus the calculations may be restricted to the solution of the electronic TDSE for fixed internuclear separation.
For a fixed $R$ one may write the **electronic TDSE** as follows:

$$i\frac{\partial}{\partial t}\Psi(\vec{r}; t) = \left[\hat{H}_0 + \hat{U}_{\rm int}(t)\right]\Psi(\vec{r}; t), \tag{6.8}$$

where the time-dependent Hamiltonian has two contributions: the $\hat{H}_0$ field-free and the $\hat{U}_{\rm int}$ interaction (with the laser field) term.

As already seen previously in Sec. 6.1 [Eqs. (6.4)-(6.6)], the field-free Hamiltonian is

calculated as:

$$\hat{H}_0 = \hat{T} + \hat{V} = \left(\frac{-\nabla^2}{2\mu}\right) + \left(-\frac{Z_\mathrm{A}}{r_\mathrm{A}} - \frac{Z_\mathrm{B}}{r_\mathrm{B}}\right). \tag{6.9}$$

For the interaction between the electron and the laser field the dipole approximation [74, 75] was considered, since the typical size of the used wave lengths was few orders of magnitude ($> 10^2$) larger than the typical size of the molecule, hence the electron-laser interaction term can be described using the dipole approximation in length gauge as:

$$\hat{U}_\mathrm{int} = \vec{r}\vec{E}(t); \tag{6.10}$$

with $\vec{E}(t)$ being the electric vector component of the laser field.

In this work linearly polarized $\vec{E}(t) = (0, 0, E_z = E(t))$ pulses with sine-square envelope were considered, which can be described with the following analytical form:

$$E(t) = \begin{cases} E_0 \sin\left(\omega t + \varphi_\mathrm{CEP}\right) \sin^2\left(\frac{\pi t}{\tau}\right), & \text{if } t \in [0, \tau], \\ 0, & \text{otherwise;} \end{cases} \tag{6.11}$$

where $\omega$ is the carrier frequency, $\tau$ is the pulse duration, $\varphi_\mathrm{CEP}$ is the carrier-envelope-phase, and $E_0$ represents the amplitude of the electric field.

## 6.2 Coordinate systems for laser-molecule interaction

In order to describe the studied system one may consider the use of different coordinate systems, such as the Cartesian $[x, y, z \in (-\infty, \infty)]$, the cylindrical $(\rho, z, \varphi)$, polar $(r, \theta, \varphi)$ or the prolate spheroidal coordinate $(\xi, \eta, \varphi)$ system (PSC). The coordinate transformations between them can be found in Appendix II.

The use of each coordinate system may have advantageous and disadvantageous features regarding the numerical complexity of the studied problem. In the present case, where a single active electron is present, the use of the prolate spheroidal coordinates was considered the best choice [see Eqs. (6.13)], since these coordinates offer us a major advantage, such that the field-free solutions ($H_0$) can be fully separated for the molecule:

$$\Psi_0 = \mathcal{X}(\xi)\mathcal{H}(\eta)\Phi(\varphi); \tag{6.12}$$

a property which is exploited later on during the numerical solution of the Schrödinger equation.

The **prolate spheroidal coordinates (PSC)** are defined as follows:

$$\begin{aligned} \xi &= \frac{r_\mathrm{A} + r_\mathrm{B}}{R} \in [1, \infty); \\ \eta &= \frac{r_\mathrm{A} - r_\mathrm{B}}{R} \in [-1, 1]; \\ \varphi &\quad \text{(azimuthal angle)} \in [0, 2\pi]; \end{aligned} \tag{6.13}$$

[as already pointed out: $R$ is the internuclear separation, while $r_{\mathrm{A}}$ and $r_{\mathrm{B}}$ are the electron's distances measured from the two nuclei (A and B)].

This total separability can not be achieved by working with the other coordinate systems. However, numerous studies found in the literature [76, 77] implying interactions between laser fields and diatomic molecules having a single active electron consider the use of the cylindrical coordinates:

$$\rho \in [0, \infty),\ z \in (-\infty, \infty),\ \varphi \in [0, 2\pi], \tag{6.14}$$

where the field-free solutions can be only partly separated: $\Psi_0 = \phi(\rho, z)\Phi(\varphi)$. An another disadvantage of using the cylindrical coordinates lies in the fact that the real (physical) infinite coordinate space (i.e., simulation box) should be truncated in three different directions, at positions $z_{\min}$; $z_{\max}$, and $\rho_{\max}$, whilst in the case of the PSC system, this should be done at only one point, at $\xi_{\max} < \infty$ (implying the lowest possible number of truncations). This later condition implicitly reduces the possibility of numerical errors that may occur at the edges of the configuration space during the time propagation of the electronic wave packets (EWPs) by using the prolate spheroidal coordinates.

In addition to that, the Hamiltonian will became more sparser by using PSC, hence it is numerically more efficient to work with this coordinate system.

## 6.3 TDSE in the prolate spheroidal coordinates

The geometry of the studied system and the prolate spheroidal coordinates [Eq. (6.13)] can be seen in Figure 6.1, where $(x'y'z')$ represents the frame attached to the molecule, such that the two nuclei A and B lie on the $0z'$ axis having the coordinates $(0, 0, R/2)$ and $(0, 0, -R/2)$, with $R$ being the internuclear separation. On the other hand, the $0z$ axis of the $(xyz)$ frame is attached in the direction of the polarization vector of the linearly polarized laser field, while the two axis $0y'$ and $0y$ coincide. The angle between the molecular axis and the polarization of the laser field is denoted with $\theta_R$.

The operators of the electronic Hamiltonian [Eqs. (6.21)-(6.8)] using the PSC will have the following form [78]:

- The operator of the Coulomb-potential:

$$\hat{V} = -\frac{2}{R}\left[\frac{Z_{\mathrm{A}}(\xi - \eta) + Z_{\mathrm{B}}(\xi + \eta)}{\xi^2 - \eta^2}\right]. \tag{6.15}$$

- The kinetic energy operator:

$$\hat{T} = -\frac{\nabla^2}{2\mu} = \frac{2}{\mu R^2}\left[\frac{\hat{T}_\xi + \hat{T}_\eta}{J(\xi, \eta)} - \frac{\partial_\varphi^2}{(\xi^2 - 1)(1 - \eta^2)}\right], \tag{6.16}$$

where $J(\xi, \eta) = \xi^2 - \eta^2$ is the Jacobian, while $\hat{T}_\xi$ and $\hat{T}_\eta$ differential operators have the

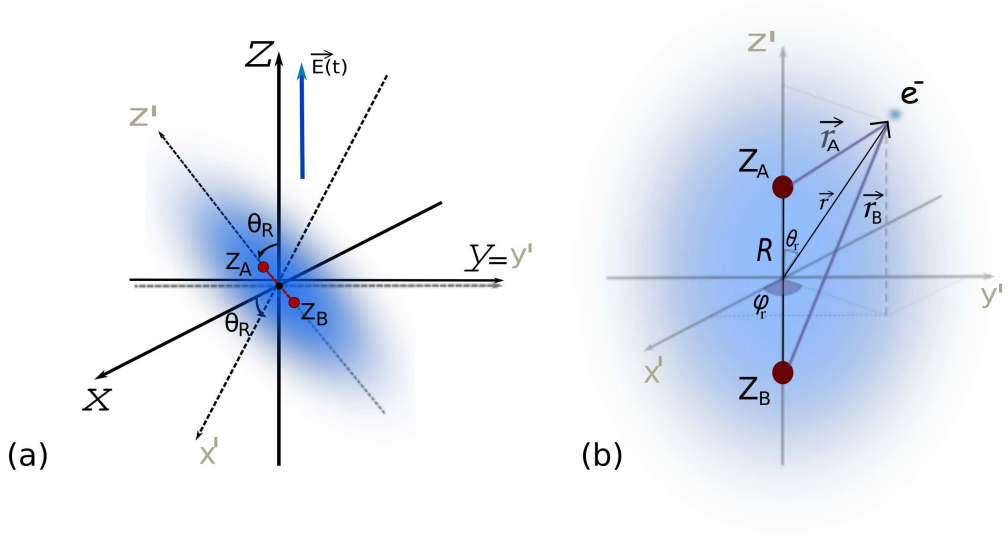


Figure 6.1: The geometry of the studied system in the frame attached to the laser polarization axis (subfigure a) and in the frame attached to the molecular axis (subfigure b). The (x'y'z') molecular framework is rotated by the angle $\theta_R$ around the Oy=Oy' axis. The electric component of the incident laser field is linearly polarized in the Oz direction.

following expressions:

$$\hat{T}_\xi = -\frac{\mathrm{d}}{\mathrm{d}\xi}(\xi^2-1)\frac{\mathrm{d}}{\mathrm{d}\xi};\ \hat{T}_\eta = -\frac{\mathrm{d}}{\mathrm{d}\eta}(1-\eta^2)\frac{\mathrm{d}}{\mathrm{d}\eta}. \tag{6.17}$$

- The laser-electron interaction operator:

$$\begin{aligned}\hat{U}_{\mathrm{int}}(t) &= \vec{r}\vec{E}(t) = E(t)z = E(t)[z'\cos\theta_R + x'\sin\theta_R] = \\ &= E(t)\left[\frac{R}{2}\xi\eta\cos\theta_R + \frac{R}{2}\sqrt{(\xi^2-1)(1-\eta^2)}\sin\theta_R\right].\end{aligned} \tag{6.18}$$

with $\vec{E}(t) = \hat{\epsilon}E(t)$ being the linearly polarized [i.e., $\hat{\epsilon} \equiv (0,0,\epsilon_z = 1)$] electric component of the external laser field, and $\theta_R$ the angle between the molecular axis and the $\hat{\epsilon}$ polarization vector (see Fig. 6.1b). $x'$ and $z'$ are the components of the electron position vector $\vec{r}$ in the coordinate system fixed to the molecular frame (see Fig. 6.1a). This term can also be transformed into the prolate spheroidal coordinate system after expressing $x'$, $z'$ as a function of $\{\xi,\eta,\varphi\}$: $z' = (R/2)\xi\eta$; $x' = (R/2)\sqrt{(\xi^2-1)(1-\eta^2)}\cos\varphi$ (see Appendix II.).

This laser-electron interaction term was derived using the dipole approximation [i.e., the spatial dependence of the vector potential is neglected due to the fact that the laser's wavelength is much larger than the typical size of the molecule, thus $\vec{A}(\vec{r};t) \approx \vec{A}(t)$], and it's expressed in length gauge.

By taking into account the separability of the field-free wave function [Eq. (6.12)] the

following *ansatz* is used for the time-dependent wave function (TDWF):

$$\Psi(t) = \sum_{m=-\infty}^{\infty} \Psi^{(m)}(\xi,\eta;t)\frac{e^{im\varphi}}{\sqrt{2\pi}}, \tag{6.19}$$

where $m \in \mathbb{Z}$.

After inserting the TDWF [Eq. (6.19)] into the electronic TDSE [Eq. (6.8)], then using the expressions of the contributing parts of the Hamiltonian operator [Eqs. (6.15)-(6.18)]; by doing some algebra operations one can deduce the **TDSE in the prolate spheroidal coordinate system**:

$$\begin{aligned} i\frac{\partial\Psi^{(m)}(\xi,\eta;t)}{\partial t} &= \hat{H}_0^{(m)}\Psi^{(m)}(\xi,\eta;t) + E(t)\frac{R}{2}\xi\eta\cos\theta_R\Psi^{(m)}(\xi,\eta;t) + \\ &+ \frac{E(t)R}{2}\sqrt{(\xi^2-1)(1-\eta^2)}\sin\theta_R\frac{\Psi^{(m-1)}(\xi,\eta;t)+\Psi^{(m+1)}(\xi,\eta;t)}{2}, \end{aligned} \tag{6.20}$$

where

$$\hat{H}_0^{(m)} = \left[\frac{2}{m_e R^2}\left(\frac{\hat{T}_\xi+\hat{T}_\eta}{\xi^2-\eta^2} + \frac{m^2}{(\xi^2-1)(1-\eta^2)}\right) - \frac{2}{R}\left(\frac{Z_{\mathrm{A}}(\xi-\eta)+Z_{\mathrm{B}}(\xi+\eta)}{\xi^2-\eta^2}\right)\right]. \tag{6.21}$$

Equation (6.20) is a set of coupled partial differential equations, where the couplings (last term in the equation) between the different (neighbouring) channels labelled with quantum number $m$ occur if the angle between the molecular axis and the polarization vector of the external electric field is different from 0 (i.e., $\sin\theta_R \neq 0$).

## 6.4 TDSE on Finite Element Discrete Variable Representation grids

For the discretization of the $\Psi^{(m)}(\xi,\eta)$ wave function I have used the finite element discrete variable representation (FE-DVR) method for both the $\xi$ and $\eta$ coordinates. According to FE-DVR method the configuration space ($\xi \in [1,\xi_{\max}]$; $\eta \in [-1,1]$) was divided into smaller sub-domains, or finite elements (FEs), and the WF expanded in the basis of local DVR functions in each FE (see Fig. 6.2). The number of DVR functions considered in each FEs was constant: $\mathrm{N_{fun}} = \mathrm{N_{fun}}^{\{\xi\}} = \mathrm{N_{fun}}^{\{\eta\}}$ .

The DVR functions defined in the $\alpha^{th}$ FE had the following general (writing $x$ instead of $\xi$ and $\eta$) analytical form:

$$f_p^{(\alpha)}(x) = \begin{cases} \frac{L_1^{(\alpha)}(x)+L_{N_{\mathrm{fun}}}^{(\alpha-1)}(x)}{\sqrt{w_1^{(\alpha)}+w_{N_{\mathrm{fun}}}^{(\alpha-1)}}}, & p=1; \\ \frac{L_p^{(\alpha)}(x)}{\sqrt{w_p^{(\alpha)}}}, & p=2,\cdots \mathrm{N_{fun}}-1; \\ \frac{L_{N_{\mathrm{fun}}}^{(\alpha)}(x)+L_1^{(\alpha+1)}(x)}{\sqrt{w_{N_{\mathrm{fun}}}^{(\alpha)}+w_1^{(\alpha+1)}}}, & p=\mathrm{N_{fun}}, \end{cases} \tag{6.22}$$

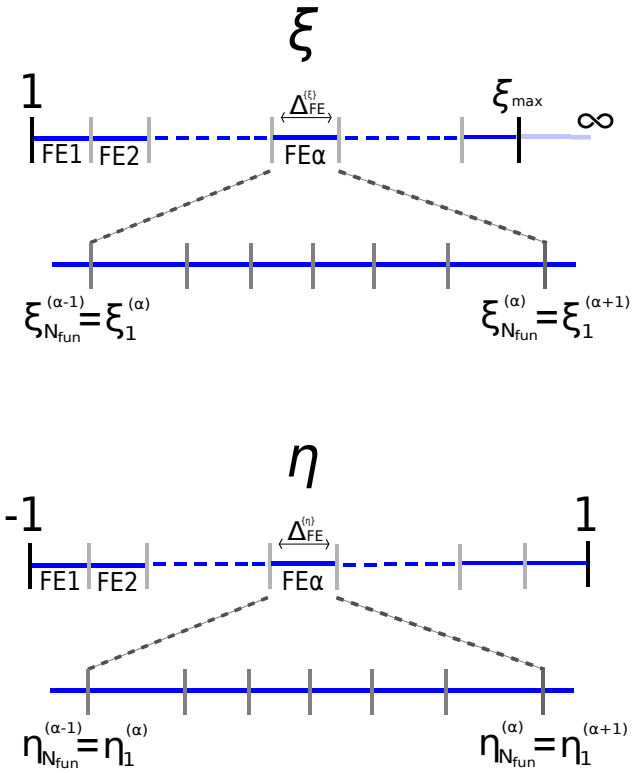


Figure 6.2: The FE-DVR grid used for the $\xi$ and $\eta$ coordinates.

where

$$L_p^{(\alpha)}(x) = \mathcal{P}_p^{(\alpha)}(x)\theta(x - x_1^{(\alpha)})\theta(x_{N_{\text{fun}}}^{(\alpha)} - x), \tag{6.23}$$

and $\mathcal{P}_p(x)$ represents the Lagrange interpolating polynomials:

$$\mathcal{P}_p(x) = \prod_{k\neq p}^{N_{\text{fun}}} \frac{x - x_k}{x_p - x_k}, \tag{6.24}$$

which have the property $\mathcal{P}_p(x_q) = \delta_{pq}$. In Equation (6.23) the use of the Heaviside (step)-function ensured that $L_p^{(\alpha)}(x)$ had nonzero values only inside the $\alpha^{th}$ FE, since:

$$\theta(x - x_0) = \begin{cases} 1, & x \geq x_0; \\ 0, & \text{otherwise.} \end{cases} \tag{6.25}$$

Since the Hamiltonian contains at most second order derivatives, it was sufficient to ensure the continuity at the finite element boundaries, which was achieved by the use of the so-called "bridge" functions (i.e., the basis functions when $p = 1, \text{N}_{\text{fun}}$). In each FE the Lagrange interpolating polynomials were defined using a set of local gridpoints, i.e., the Gauss-Lobatto quadrature points and their associated weights $w_p^{(\alpha)}$.

Using the FE-DVR method the main advantage consists in the following. Since the underlying configuration space is divided into smaller FEs, in each of which the wave function is represented in a local DVR basis, the kinetic energy matrix will not be 'full' as in the

standard DVR approach, but will be made up of several blocks which overlap at only several points. The sparsity of the matrix facilitates the numerical calculations of matrix-vector products, and the diagonalization of the Hamiltonian. For a local potential [e.g., $U_{\rm int}(t)$, $V$] the matrix remains diagonal.

### 6.4.1 Using the matrix formalism

In order to obtain the final symmetrical form of the Hamiltonian (see below at the *Symmetrization of the Hamiltonian* subsection), and to simplify the numerical calculations when scalar products (e.g., calculation of the wave function norm or transition amplitudes) are needed, I employed the following substitution for the time-dependent wave function:

$$\Psi^{(m)}(\xi_i,\eta_j;t)=\psi_{ij}^{(m)}(t)\Big/\sqrt{(R^3/8)w_i^{\{\xi\}}w_j^{\{\eta\}}J(\xi_i,\eta_j)}, \tag{6.26}$$

where the global indexing of $i\equiv(\alpha^{\{\xi\}},p^{\{\xi\}})$ and $j\equiv(\alpha^{\{\eta\}},p^{\{\eta\}})$) was considered, and $w_i^{\{\xi\}}$ and $w_j^{\{\eta\}}$ are the weights associated to the corresponding Gauss-Lobatto quadrature points $\xi_i$ and $\eta_j$, respectively (see Fig. 6.2); while $J(\xi_i,\eta_j)=(\xi_i^2-\eta_j^2)$ is the Jacobian calculated in the given gridpoints.

Equation (6.26) can be easily obtained, after one uses the following wave function expansion in terms of the $f_{i'}(\xi)$ and $g_{j'}(\eta)$ local DVR functions (6.22) defined on the $\xi_{i'}$ and $\eta_{j'}$ gridpoints:

$$\Psi^{(m)}(\xi,\eta;t)=\sum_{i'=1}^{\mathrm{N}_\xi}\sum_{j'=1}^{\mathrm{N}_\eta}\psi_{i'j'}^{(m)}(t)f_{i'}(\xi)g_{j'}(\eta)/\sqrt{(R^3/8)J(\xi_{i'},\eta_{j'})}, \tag{6.27}$$

where $\mathrm{N}_\xi$ and $\mathrm{N}_\eta$ are the total number of gridpoints considered on the two coordinate axis, and by knowing that the DVR functions satisfy the following equations: $f_{i'}(\xi_i)=\delta_{ii'}/\sqrt{\omega_{i'}^{\{\xi\}}}$ and $g_{j'}(\eta_j)=\delta_{jj'}/\sqrt{\omega_{j'}^{\{\eta\}}}$.

As already mentioned before using the substitution (6.26) for the TDWF the evaluation of scalar products (i.e., integrals) of the form:

$$\langle\Psi_1^{(m)}|\Psi_2^{(m)}\rangle=\sum_{ij}[\psi_{1ij}^{(m)}]^*\psi_{2ij}^{(m)} \tag{6.28}$$

becomes numerically *cheaper*, since the number of multiplications in the scalar products is minimized, i.e., reduced to 1.

By considering the substitution (6.26) and inserting Equation (6.19) into the TDSE (6.8), and after performing some basic algebraic operations one can obtain the **TDSE in the matrix formalism** (i.e., the *projection* of Equation (6.20) on the FE-DVR basis):

$$i\frac{\partial\psi_{ij}^{(m)}(t)}{\partial t}=\sum_{m'i'j'}H_{iji'j'}^{mm'}(t)\psi_{i'j'}^{(m')}(t), \tag{6.29}$$

where the coupling (Hamiltonian) matrix elements are decomposed as follows:

$$H^{mm'}_{iji'j'}(t) = T^{mm'}_{iji'j'} + V^{mm'}_{iji'j'} + U^{mm'}_{iji'j'}(t)., \tag{6.30}$$

and their explicit forms can be found listed in Table 6.1, at the end of the current subsection. The TDWF labelled with the quantum number $m$ is given formally as the column matrix:

$$\left|\psi^{(m)}(\xi,\eta)\right\rangle \rightarrow \begin{bmatrix} \psi^{(m)}(\eta_1,\xi_1) \\ \psi^{(m)}(\eta_2,\xi_1) \\ \vdots \\ \psi^{(m)}(\eta_{N_\eta},\xi_1) \\ \psi^{(m)}(\eta_1,\xi_2) \\ \psi^{(m)}(\eta_2,\xi_2) \\ \vdots \\ \psi^{(m)}(\eta_{N_\eta},\xi_2) \\ \vdots \\ \vdots \\ \psi^{(m)}(\eta_1,\xi_{N_\xi}) \\ \psi^{(m)}(\eta_2,\xi_{N_\eta}) \\ \vdots \\ \psi^{(m)}(\eta_{N_\eta},\xi_{N_\xi}) \end{bmatrix}.$$

Equation (6.29) can be also written in the explicit form, i.e., the value of TDWF in the $(\xi_i,\eta_j)$ coordinate is governed by the following equation:

$$\begin{aligned} i\frac{\partial}{\partial t}\psi^{(m)}_{ij}(t) &= \sum_{i',j'}\left\{\frac{2}{m_e R^2} J^{-1/2}_{ij} J^{-1/2}_{i'j'}\left[\delta_{jj'}\langle f_i|\hat{T}_\xi|f_{i'}\rangle + \delta_{ii'}\langle g_j|\hat{T}_\eta|g_{j'}\rangle\right]\right. \\ &+ \left.\delta_{ii'}\delta_{jj'}\left[\frac{2m^2}{m_e R^2(\xi_i^2-1)(1-\eta_j^2)} + V_{ij} + E(t) z'_{ij}\cos\theta_R\right]\right\}\psi^{(m)}_{i'j'}(t) + \\ &+ \sum_{i',j'}\left\{\delta_{ii'}\delta_{jj'}E(t)x'_{ij\{\varphi=0\}}\sin\theta_R\right\}\frac{\psi^{(m-1)}_{i'j'}(t) + \psi^{(m+1)}_{i'j'}(t)}{2}, \end{aligned} \tag{6.31}$$

where $z'_{ij} = (R/2)\xi_j\eta_j$ and $x'_{ij\{\varphi=0\}} = (R/2)\sqrt{(\xi_i^2-1)\left(1-\eta_j^2\right)}$.

In order to obtain Equation (6.31) and the matrix elements listed in Table 6.1 the following procedure was considered when evaluating integrals:

$$\begin{aligned} \langle f_i|A(\xi,\eta)|f_{i'}\rangle &= \int_1^\infty \mathrm{d}\xi\ f_i(\xi)A(\xi,\eta)f_{i'}(\xi) \simeq \\ &\simeq \sum_{k=1}^{\mathrm{N}_\xi}\omega_k^{\{\xi\}} f_i(\xi_k)A(\xi_k,\eta)f_{i'}(\xi_k) = \delta_{ii'}A(\xi_i,\eta), \end{aligned} \tag{6.32}$$

and in a similar way:

$$\langle g_j|B(\xi,\eta)|g_{j'}\rangle = \int_{-1}^{1} \mathrm{d}\eta\ g_j(\eta)B(\xi,\eta)g_{j'}(\eta) \simeq \delta_{jj'}B(\xi,\eta_j), \tag{6.33}$$

where $A(\xi,\eta)$ and $B(\xi,\eta)$ are the general representations of two non-differentiating operators.

Table 6.1: The Matrix elements of the coupling matrices [Eq. (6.30)]: (A) Kinetic-energy; (B) Coulomb-potential; (C) laser-electron interaction.

(A)

$$T^{mm'}_{iji'j'} = \delta_{mm'}\left\{\frac{2}{m_eR^2}\frac{\langle f_i|\hat{T}_\xi|f_{i'}\rangle\delta_{jj'}+\langle g_j|\hat{T}_\eta|g_{j'}\rangle\delta_{ii'}}{\sqrt{J_{ij}}\sqrt{J_{i'j'}}} + \delta_{ii'}\delta_{jj'}\left[\frac{2m^2}{m_eR^2(\xi_i^2-1)(1-\eta_j^2)}\right]\right\}$$

(B)

$$V^{mm'}_{iji'j'} = \delta_{mm'}\delta_{ii'}\delta_{jj'}V(\xi_i,\eta_j)$$

(C)

$$U^{mm'}_{iji'j'}(t) = \delta_{ii'}\delta_{jj'}\Big[\delta_{mm'}z'_{ij}E(t)\cos\theta_R + \frac{(\delta_{m-1,m'}+\delta_{m+1,m'})}{2}x'_{ij\{\varphi=0\}}E(t)\sin\theta_R\Big],$$

where $z'_{ij} = (R/2)\xi_j\eta_j$, and $x'_{ij\{\varphi=0\}} = (R/2)\left(\xi_i^2-1\right)^{-1/2}\left(1-\eta_j^2\right)^{-1/2}$.

### 6.4.2 Symmetrization of the Hamiltonian matrix

In order to obtain physically accurate results the $\hat{H}(t)$ operator should be represented by a Hermitian matrix, i.e., a symmetric matrix in the FE-DVR representation. By taking into account that in the expansion of the $\Psi^{(m)}(\xi,\eta;t)$ the $f_i(\xi)$ and $g_j(\eta)$ basis functions are real, we seek for a symmetric Hamiltonian matrix. In the right-hand side of Equation (6.31) the matrix elements of the Coulomb interaction operator ($V_{ij}$) and the laser-interaction operators are symmetrical (diagonal matrices), but the kinetic-energy matrix should be symmetrized. The symmetrization can be done by integrating by parts the $\langle f_i|\hat{T}_\xi|f_{i'}\rangle$, $\langle g_j|\hat{T}_\eta|g_{j'}\rangle$ elements:

$$\begin{aligned}(\hat{T}_\eta)_{jj'} = \langle g_j|\hat{T}_\eta|g_{j'}\rangle &= -\int_{-1}^{1}\mathrm{d}\eta\ g_j(\eta)\frac{\mathrm{d}}{\mathrm{d}\eta}\left[(1-\eta^2)\frac{\mathrm{d}}{\mathrm{d}\eta}g_{j'}(\eta)\right] = \\ &= -\left[(1-\eta^2)g_jg'_{j'}\right]\Big|_{-1}^{+1} + \int_{-1}^{1}\mathrm{d}\eta(1-\eta^2)g'_jg'_{j'}\end{aligned} \tag{6.34}$$

The similar operation can be done with the $\xi$ dependent elements:

$$\begin{aligned}(\hat{T}_\xi)_{ii'} = \langle f_i|\hat{T}_\xi|f_{i'}\rangle &= -\int_1^\infty \mathrm{d}\xi\ f_i(\xi)\frac{\mathrm{d}}{\mathrm{d}\xi}\left[(\xi^2-1)\frac{\mathrm{d}}{\mathrm{d}\xi}f_{i'}(\xi)\right] = \\ &= -\left[(\xi^2-1)f_i f'_{i'}\right]\Big|_1^\infty + \int_1^\infty \mathrm{d}\xi(\xi^2-1)f'_i f'_{i'} \end{aligned} \tag{6.35}$$

In Equation (6.34) only the last (symmetric) term remains, because when $\eta = \pm 1$ the term $1-\eta^2$ is zero. On the other hand, the value for $(\hat{T}_\xi)_{ii'}$ matrix element can also be approximated with the numerical value of the last integral, first because when $\xi = 1$ the term $\xi^2 - 1$ is zero, second when $\xi$ goes to infinity the $\lim_{\xi\to\infty} f_i^{(\text{Last FE})}(\xi) = 0$ equality can be considered as a valid approximation, since the value infinity lies outside of the last FE on the truncated FE-DVR grid.

According to the above considerations one will obtain a symmetric Hamiltonian by applying the Gauss integration quadrature to evaluate the integrals in Equations (6.34)-(6.35)

$$\langle g_j|\hat{T}_\eta|g_{j'}\rangle = \int_{-1}^{1}\mathrm{d}\eta(1-\eta^2)g'_j g'_{j'} \approx \sum_l \tilde{w}_l\ (1-\eta_l^2)g'_j(\eta_l)g'_{j'}(\eta_l); \tag{6.36}$$

$$\langle f_i|\hat{T}_\xi|f_{i'}\rangle \approx \int_1^\infty \mathrm{d}\xi(\xi^2-1)f'_i f'_{i'} \approx \sum_k w_k\ (\xi_k^2-1)f'_i(\xi_k)f'_{i'}(\xi_k), \tag{6.37}$$

and inserting the results into Equation (6.31).

In both expressions of Eqs. (6.36)-(6.37) the calculation of the first order derivative of

Table 6.2: The first order derivative of the Lagrange interpolating polynomial given in a general form (A) and calculated in the $x_l^{(\alpha)}$ FE-DVR grid point (B).

(A)

$$\begin{aligned}\frac{\mathrm{d}}{\mathrm{d}x}\mathcal{P}_p^{(\alpha)}(x) &= \frac{\mathrm{d}}{\mathrm{d}x}\left(\prod_{\substack{n=1\\n\neq k}}^{\mathrm{N_{fun}}}\frac{x-x_n^{(\alpha)}}{x_k^{(\alpha)}-x_n^{(\alpha)}}\right) \\ &= \sum_{\substack{n=1\\n\neq k}}^{\mathrm{N_{fun}}}\frac{1}{x_k^{(\alpha)}-x_n^{(\alpha)}}\prod_{\substack{i=1\\i\neq k,n}}^{\mathrm{N_{fun}}}\frac{x-x_i^{(\alpha)}}{x_k^{(\alpha)}-x_i^{(\alpha)}}. \end{aligned} \tag{6.38}$$

(B)$x \to x_l^j$

$$\frac{\mathrm{d}\mathcal{P}_p^{(\alpha)}}{\mathrm{d}x}(x_l^{(\alpha)}) = \begin{cases} \sum\limits_{\substack{n=1\\n\neq l}}^{\mathrm{N_{fun}}}\frac{1}{x_k^{(\alpha)}-x_n^{(\alpha)}}, & \text{for } \boldsymbol{x_l^{(\alpha)} = x_k^{(\alpha)}} \\ \frac{1}{x_k^{(\alpha)}-x_l^{(\alpha)}}\prod\limits_{\substack{p=1\\p\neq k,l}}^{\mathrm{N_{fun}}}\frac{x_l^{(\alpha)}-x_p^{(\alpha)}}{x_k^{(\alpha)}-x_p^{(\alpha)}}, & \text{for } \boldsymbol{x_l^{(\alpha)} \neq x_k^{(\alpha)}}. \end{cases} \tag{6.39}$$

Lagrange polynomials is involved, which can be obtained by performing some analytical calculations:

$$\begin{aligned}\frac{\mathrm{d}}{\mathrm{d}x}L_p^{(\alpha)}(x) &= \frac{\mathrm{d}\mathcal{P}_p^{(\alpha)}(x)}{\mathrm{d}x}\theta(x-x_1^{(\alpha)})\theta(x_{N_{\mathrm{fun}}}^{(\alpha)}-x) \\ &+ \mathcal{P}_p^{(\alpha)}(x)\left[\theta(x_{N_{\mathrm{fun}}}^{(\alpha)}-x)\delta(x-x_1^{(\alpha)})-\theta(x-x_1^{(\alpha)})\delta(x_{N_{\mathrm{fun}}}^{(\alpha)}-x)\right], \quad (6.40)\end{aligned}$$

where the first order derivative of the Lagrange interpolating polynomial was calculated analytically and listed in Table 6.2. The shape of both matrices $(\hat{T}_\xi)$ and $(\hat{T}_\eta)$ constructed from the matrix elements calculated in Eqs. (6.36)-(6.37) will be sparse, with large off-diagonal regions having values of zero (see Fig. 6.3). From the numerical point of view it is advantageous to have a sparse Hamiltonian, because the matrix-vector multiplications will be cheaper. On the other hand, I have further optimized the code by employing a proper parallelization (using OpenMPI) along the $\xi$ configuration space (i.e., the same number of FEs were distributed on each CPU).

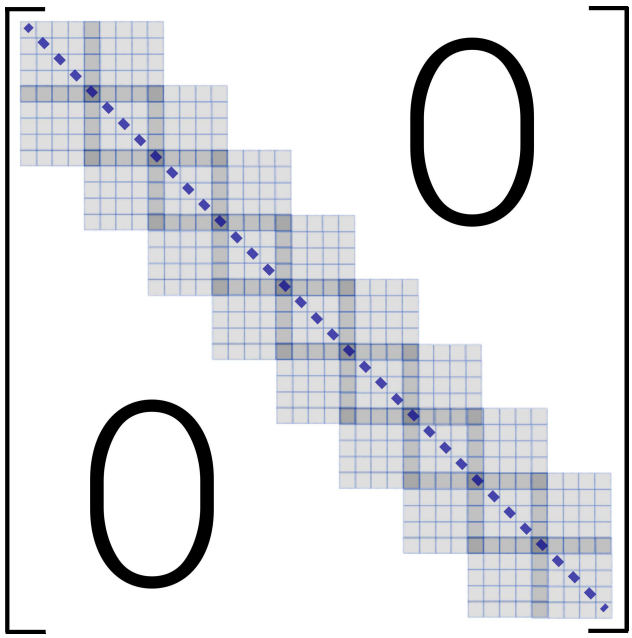


Figure 6.3: The shape (internal structure) of the $T_\xi$, $T_\eta$ matrices of the full $H(t)$ Hamiltonian in the present representation.

Finally it is worth mentioning, that by using the FE-DVR grid a high accuracy can be achieved with the help of much less gridpoints than in the case of the finite difference (FD) grid. The other advantage of FE-DVR lies in its flexibility which means that the size of each FE can be adjusted in the configuration space. During the numerical simulation in the regions of configuration space where the main physical processes take place a higher local grid density can be used. Outside of this region a sparser grid can be employed.

## 6.5 Temporal propagation of the wave function

At the early stages of the numerical code's development the fourth order Runge-Kutta method[79, 80] was used for solving the TDSE since its implementation does not require laborious procedures. Despite the fact, that it is not the most efficient TDSE solver technique - when high accuracy results are needed in the shortest time - it was used in the beginning to test the correctness of other components of the code and to acquire relevant data as well. After these primary tests a state-of-the-art method was implemented, the *short-iterative Lanczos (SIL)* method, which is an elaborate technique used worldwide in leading theoretical groups. The SIL algorithm gives the possibility to set the precision of the time propagation, either by using an adaptive time step scheme, or by adaptively increasing the local configuration space where the TDSE is solved. This algorithm will be briefly presented in this section.

### The short-iterative Lanczos method

SIL is an explicit propagation method, which approximates the evolution operator $[\hat{U}(t)]$, yet it still calculates $\hat{U}(t)$ by a direct exponentiation of $\hat{H}$. It is worth mentioning that the Lanczos method implies Hermitian (i.e., symmetrical Hamiltonian in our case) operators.

At the basis of the Lanczos propagator lies the construction of a local subspace of the full Hilbert space, the so-called *Krylov subspace*, which was originally proposed to calculate eigenstates and eigenenergies of large matrices [81]. In the present work the Krylov-subspace is constructed by the repeated action of the Hamiltonian on the initial $|\Psi_0\rangle = |\Psi(\vec{r};t)\rangle$ state, during which an $\mathrm{N_K} = n+1$ dimensional subspace is created:

$$K_{n+1}(t) = \left\{ |\Psi_0\rangle, \hat{\mathbf{H}}|\Psi_0\rangle, \hat{\mathbf{H}}^2|\Psi_0\rangle, \ldots, \hat{\mathbf{H}}^n|\Psi_0\rangle \right\} \tag{6.41}$$

With the increase of the subspace size, the precision of the approximated evolution operator also increases, however, this does not mean a linear dependence, since the most probable paths the exact WF will follow are in the direction of $|\Psi_0\rangle$ and the $\hat{\mathbf{H}}|\Psi_0\rangle$ vectors (states), and by increasing the order of the vectors ($n$) these individual $|\mathcal{K}_n\rangle \equiv \hat{\mathbf{H}}^n|\Psi_0\rangle$ paths become less and less probable. Thus, by increasing the size of the Krylov-subspace convergence will be obtained within a proposed error tolerance. It is convenient to transform the vectors of $K_{n+1}(t)$ into an orthonormal set of $Q_{n+1}$ vectors that will span $K_{n+1}$:

$$Q_{n+1}(t) = \{|q_0\rangle, |q_1\rangle, |q_2\rangle, \ldots, |q_n\rangle\}, \tag{6.42}$$

where $|q_0\rangle = |\Psi_0\rangle/||\Psi_0||$, and $\langle q_k|q_l\rangle = \delta_{kl}$, while the individual $|q_k\rangle$ vectors were obtained by employing the Gram-Schmidt orthogonalization procedure as:

$$|q_k\rangle = |\mathcal{K}_k\rangle - \sum_{l=0}^{k-1} \frac{\langle \mathcal{K}_k|q_l\rangle}{\langle q_l|q_l\rangle}|q_l\rangle, \quad \text{for } k \geq 1. \tag{6.43}$$

In this $Q_{n+1}(t)$ basis the $(n+1)\times(n+1)$ sized $(\hat{\mathbf{h}})$ Hamiltonian (Hessenberg) matrix was built up with the $\alpha_k = \langle q_k|\hat{\mathbf{H}}|q_k\rangle$ matrix elements on the main diagonal, and $\beta_{k-1,k} = \beta_{k,k+1} \equiv \langle q_k|\hat{\mathbf{H}}|q_{k+1}\rangle$ on the two secondary diagonals:

$$(\hat{\mathbf{h}}) = \mathbf{Q}^{\mathrm{T}}\mathbf{H}\mathbf{Q} = \begin{pmatrix} \alpha_0 & \beta_0 & 0 & \cdots & 0 \\ \beta_0 & \ddots & \ddots & \ddots & \vdots \\ 0 & \ddots & \ddots & \ddots & \vdots \\ \vdots & \ddots & \ddots & \ddots & \beta_{n-1} \\ 0 & \cdots & 0 & \beta_{n-1} & \alpha_n \end{pmatrix}.$$

The formal solution of the time-dependence Schrödinger equation leads to:

$$|\Psi(\mathbf{r};t+\delta t)\rangle = \hat{U}(t+\delta t,t)|\Psi(\mathbf{r};t)\rangle, \tag{6.44}$$

where by assuming that over the time interval $(t, t+\delta t)$ the Hamiltonian is time independent the evolution operator can be approximated as:

$$\hat{\mathbf{U}}(t+\delta t,t) = e^{-i\hat{\mathbf{H}}(t)\delta t}. \tag{6.45}$$

In the constructed Krylov subspace the time evolution operator is approximated as $\hat{\mathbf{U}} \simeq \hat{\mathbf{U}}^Q = \exp\{-i\hat{\mathbf{H}}^Q(t)\delta t\} = \mathbf{Q}\ \exp\{-i\hat{\mathbf{h}}\delta t\}\mathbf{Q}^\dagger$, where $\mathbf{Q}$ contains as columns the $|q_i\rangle$ basis vectors. By the assumption that $(\hat{\mathbf{h}})$ is diagnosable, the TDWF can be written as

$$|\Psi(\mathbf{r};t+\delta t)\rangle = \mathbf{Q}\left[\mathbf{\Phi}^\dagger\ \mathrm{diag}\left(e^{-i\epsilon_1\delta t},\ldots,e^{-i\epsilon_{n+1}\delta t}\right)\mathbf{\Phi}\right]\mathbf{Q}^\dagger|\Psi(\mathbf{r};t)\rangle, \tag{6.46}$$

where the columns of the $\mathbf{\Phi}$ matrix are built up from the $\{|\Phi_1\rangle, |\Phi_2\rangle, \ldots, |\Phi_{n+1}\rangle\}$ eigenvectors of the $(\hat{\mathbf{h}})$ operator, while $\epsilon_1,\ldots,\epsilon_{n+1}$ represent their corresponding eigenenergies. By using the equality $\mathbf{Q}^\dagger|\Psi(\vec{r};t)\rangle \equiv \mathbf{Q}^\dagger|q_0\rangle = (1,0,\cdots,0)^T$ , and the orthonormal property $\langle q_k|q_l\rangle = \delta_{kl}$, the expression leads to the form of:

$$|\Psi(\vec{r};t+\delta t)\rangle = \mathbf{Q}\mathbf{\Phi}^\dagger\mathrm{diag}\left(e^{-i\epsilon_1\delta t},\ldots,e^{-i\epsilon_{n+1}\delta t}\right)|\Phi_1\rangle. \tag{6.47}$$

After performing the multiplications in Equation (6.46) the final form of the SIL scheme can be expressed as

$$|\Psi(\vec{r};t+\delta t)\rangle = \sum_{k=0}^{n}\sum_{j=1}^{n+1}\Phi_{k+1}(j)e^{-i\epsilon_j\delta t}\Phi_1(j)|q_k\rangle, \tag{6.48}$$

where $\Phi_k$ is the $k$-th eigenvector of $\hat{\mathbf{h}}$.

## Error estimation of the time propagation

Within the presented time-propagation scheme the convergent $\Psi(t+\delta t)$ time-dependent wave function can be obtained in two distinct ways. In the first approach the $\delta t \to \Delta t$ time step is fixed all over the simulation time, and in each propagation step the desired convergence of the newly calculated $\Psi(t+\Delta t)$ wave function is obtained by gradually increasing the size of the Krylov-subspace. The second possibility to achieve convergent results is to fix the size of the Krylov-subspace and in each propagation step gradually decrease the $\Delta t$ time step, till a desired accuracy is reached.

In the present work the Equation (6.48) was solved by taking into account the first error estimation procedure, when the time step $\Delta t$ was fixed during the simulation and adjustable Krylov subspace size was used. For this approach a $\delta_{\mathrm{rel}}$ parameter was introduced and defined as

$$\delta_{\mathrm{rel}}^{(\mathrm{N_K}+1)} = \frac{\|\Psi^{(\mathrm{N_K}+1)}(t_i+\Delta t) - \Psi^{(\mathrm{N_K})}(t_i+\Delta t)\|}{\|\Psi^{(\mathrm{N_K})}(t_i+\Delta t)\|}, \tag{6.49}$$

which estimates the the relative error of the time propagation step. Starting from a lower value (typically 5 or 7) for the initial $\mathrm{N_K}$ size of the Krylov subspace in each discrete $t_{i+1}$ time moment the wave function $\Psi^{(\mathrm{N_K})}(t_i+\Delta t)$ is calculated according to the procedure described a few lines earlier, and in the same step also a more accurate $\Psi^{(\mathrm{N_K}+1)}(t_i+\Delta t)$ wave function is calculated for the larger $\mathrm{N_K}+1$ sized, i.e., more complete than the previous Krylov-subspace. The numerator in Eq. (6.49) measures the norm of the difference between the two wave functions calculated by using different subspace sizes. This value gets smaller and smaller as $\mathrm{N_K}$ is increased. Then this norm is compared to the norm of the wave function calculated with the lower subspace size $\Psi^{(\mathrm{N_K})}(t_i+\Delta t)$, which practically should be equal to 1 independently from the considered iteration step. This gradual increase of the $\mathrm{N_K}$ is repeated until the calculated $\delta_{\mathrm{rel}}^{(\mathrm{N_K}+1)}$ is brought below the desired propagation error tolerance: $\delta_{\mathrm{rel}}^{(\mathrm{N_K}+1)} < \varepsilon_{\mathrm{tol}}^{(\mathrm{prop})}$. Finally, it is worth mentioning that this approach inherently implies to run at least twice the short-iterative Lanczos scheme in each time step in order to be able to calculate a relative estimated error according to Eq. (6.49).

In the present case an error tolerance of $\varepsilon_{\mathrm{tol}}^{(\mathrm{prop})} = 10^{-8}$ was used, and the time step was fixed to $\Delta t = 10^{-3}$.

## 6.6 Calculation of physical quantities

By solving the TDSE [Eqs. (6.41)-(6.48)] the time dependent wave function $\Psi(\vec{r};t)$ is obtained, which includes all the information about the studied system, (i.e., the active electron of $H_2^+$ molecule interacting with the external radiation field).

According to the elementary quantum mechanics, information regarding a physical observable $A$ (i.e., the value of the physical quantity) is extracted from the TDWF as

$$\langle A\rangle = \frac{\langle\Psi|\hat{A}|\Psi\rangle}{\langle\Psi|\Psi\rangle}, \tag{6.50}$$

where $\langle A\rangle$ represents the expected value of $A$ and $\hat{A}$ is the operator assigned to the quantity $A$. $\langle\Psi|\Psi\rangle$ means the square of the wave function's norm.

### 6.6.1 The norm of the wave function

The scalar product $S = \langle\Psi|\Psi\rangle$ represents the square of the wave function's norm, where the norm by definition is:

$$N = \sqrt{S} = \sqrt{\langle\Psi|\Psi\rangle}. \tag{6.51}$$

In the present approach $S$ is calculated as:

$$\langle\Psi|\Psi\rangle = \int_1^\infty \mathrm{d}\xi \int_{-1}^1 \mathrm{d}\eta \int_0^{2\pi} \mathrm{d}\varphi\ \frac{R^3}{8}(\xi^2-\eta^2)\Psi^*(\xi,\eta,\varphi;t)\Psi(\xi,\eta,\varphi;t), \tag{6.52}$$

where by taking into account Equation (6.19), $S$ will have the following analytical form:

$$\begin{aligned}\langle\Psi|\Psi\rangle &= \int\int \mathrm{d}\xi\mathrm{d}\eta\frac{R^3}{8}(\xi^2-\eta^2)\sum_{m,m'}\left[\Psi^{(m)}(\xi,\eta;t)\right]^*\Psi^{(m')}(\xi,\eta;t)\int \mathrm{d}\varphi\frac{e^{-im\varphi}}{\sqrt{2\pi}}\frac{e^{im'\varphi}}{\sqrt{2\pi}} = \\ &= \sum_m\int\int \mathrm{d}\xi\mathrm{d}\eta\frac{R^3}{8}(\xi^2-\eta^2)\left[\Psi^{(m)}(\xi,\eta;t)\right]^*\Psi^{(m)}(\xi,\eta;t),\end{aligned} \tag{6.53}$$

where the property

$$\int_0^{2\pi}\mathrm{d}\varphi e^{-i(m-m')\varphi} = (2\pi)\delta_{m,m'} \tag{6.54}$$

was used. By using the Gauss quadratures and introducing the substitution of the wave function [Eq. (6.27)], the calculation of the scalar product can be reduced to a simple final

expression:

$$\begin{aligned}\langle\Psi|\Psi\rangle &\simeq \sum_m \sum_k \omega_k^{\{\xi\}} \sum_l \omega_l^{\{\eta\}} \frac{R^3}{8}(\xi_k^2-\eta_l^2)\left[\Psi^{(m)}(\xi_k,\eta_l;t)\right]^* \Psi^{(m)}(\xi_k,\eta_l;t) = \\ &= \sum_m \sum_{k,l} \omega_k^{\{\xi\}}\omega_l^{\{\eta\}} \frac{R^3}{8}(\xi_k^2-\eta_l^2) \sum_{i',j'} \frac{\left[\psi_{i'j'}^{(m)}(t)\right]^* f_{i'}(\xi_k) g_{j'}(\eta_l)}{\sqrt{(R^3/8)J(\xi_{i'},\eta_{j'})}} \sum_{i,j} \frac{\psi_{ij}^{(m)}(t) f_i(\xi_k) g_j(\eta_l)}{\sqrt{(R^3/8)J(\xi_i,\eta_j)}} \equiv \\ &= \sum_m \sum_{k,l} \left[\psi_{kl}^{(m)}(t)\right]^* \psi_{kl}^{(m)}(t). \end{aligned} \tag{6.55}$$

Hence, throughout of the present work the norm of the TDWF was calculated as:

$$N = \sqrt{\sum_m \sum_{k,l} \left|\psi_{kl}^{(m)}(t)\right|^2}, \tag{6.56}$$

and its value was initialised to 1, i.e., the norm of the $|1s\sigma_g\rangle$ initial (ground) state.

### 6.6.2 Occupation probabilities of electronic bound states

During the interaction with the laser field the depletion of the $|1s\sigma_g\rangle$ initial (ground) state next to the population dynamics (increase or decrease as a function of time) of higher energy bound states were also calculated. First, because it gives us an intuitive picture relating at which part of the laser pulse the major electron dynamics are taking place, what is the physics behind these initiated dynamics (ionization mechanism, excitations by photon-absorptions). Second, in the photoelectron spectra calculation it will play a crucial role to identify properly all the bound states (BS) that remained populated after the conclusion of the laser pulse, since the removal of these states from the TDWF is the key to obtain correct photoelectron spectra.

Prior to switching the laser field on, a large number ($\approx 200$) of bound states have been calculated by the orthogonalization of the ($\hat{H}_0$) field-free Hamiltonian, and the symmetry of each obtained BS ($|\varphi_b\rangle \in \{|1s\sigma_g\rangle, |2p\sigma_u\rangle, |2s\sigma_g\rangle, \dots\}$) was automatically identified after counting the nodal planes in both the $\xi$ and $\eta$ coordinate directions. Next to the BS wave functions [eigenfunctions of ($\hat{H}_0$)] the BS energies [eigenvalues of ($\hat{H}_0$)] have also been obtained.

The time evolution of the bound state $|\varphi_b\rangle$ is governed by the $\hat{H}_0$ Hamiltonian according to the time-independent Schrödinger equation:

$$|\phi_b(t)\rangle = e^{-i\hat{H}_0 t}|\varphi_b\rangle \equiv e^{-i\varepsilon_b t}|\varphi_b\rangle, \tag{6.57}$$

where $|\varphi_b\rangle$ is the $b$ -th BS and $\varepsilon_b$ is its corresponding energy ($b \in \{0,1,2,\dots\}$; $|\varphi_0\rangle \equiv |1s\sigma_g\rangle$). The occupation probability as a function of time of the $b$-th BS was calculated as the square

of the TDWF projection onto this state as:

$$P_b(t) = \left|\left\langle \phi_b(t) \middle| \Psi(\xi,\eta,\varphi,t)\right\rangle\right|^2, \tag{6.58}$$

where in a similar way as in Eqs. (6.52)-(6.55) using the present approach is calculated using the PSC coordinates and FE-DVR grid method:

$$P_b(t) = \left| \sum_m \sum_{k,l} (\varphi_b^{(m)})^*_{kl} \psi^{(m)}_{kl}(t) \right|^2, \tag{6.59}$$

where $(\varphi_b^{(m)})_{kl}$ is the value of the bound wave function in the $\xi_k$ and $\eta_l$ gridpoints.

### 6.6.3 The expected position of the ejected electron

Next to the investigation of the occupation probabilities of different electronic bound states, an another important quantity, the the time-dependent position of continuum electronic wave packets ($\overline{r}$), will play a significant role in the photoelectron spectra calculation, as it will be discussed in more details in the following subsection.
In accordance with the general form of Eq. (6.50), $\overline{r}$ is calculated in the present approach as follows:

$$\overline{r}(t) = \frac{\langle \Psi_{\text{free}}(t)|r|\Psi_{\text{free}}(t)\rangle}{\langle \Psi_{\text{free}}(t)|\Psi_{\text{free}}(t)\rangle}, \tag{6.60}$$

where $|\Psi_{\text{free}}\rangle$ represents the free part of the wave function after the BSs with not negligible $P_b(t)$ contributions [Eq. (6.59)] have been removed from the TDWF.
**The continuum part of the electron's wave function** was calculated by employing the Gram-Schmidt procedure:

$$|\Psi_{\text{free}}(t)\rangle = |\Psi(t)\rangle - \sum_b \langle \phi_b(t)|\Psi(t)\rangle \; |\phi_b(t)\rangle, \tag{6.61}$$

where the scalar product in the last term (i.e., the projection of the TDWF onto the $|\phi_b(t)\rangle$ bound state) was calculated in a similar way as in the Equation (6.59).

By considering the present method the position of the ejected electron is obtained by the following expression:

$$\overline{r}(t) = \frac{\sum_{m,k,l} \left[\tilde{\psi}^{(m)}_{kl}(t)\right]^* \left(\frac{R}{2}\sqrt{\xi_k^2+\eta_l^2-1}\right) \tilde{\psi}^{(m)}_{kl}(t)}{\sum_{m,k,l} \left[\tilde{\psi}^{(m)}_{kl}(t)\right]^* \tilde{\psi}^{(m)}_{kl}(t)}, \tag{6.62}$$

where $\tilde{\psi}^{(m)}_{kl}(t)$ is the value of the wave function's continuum part in the $\xi_k$ and $\eta_l$ gridpoints after the substitution (6.27) was considered, and it was used that $r = (R/2)\sqrt{\xi^2+\eta^2-1}$.

### 6.6.4 Calculating the photoelectron spectrum

It is important to obtain relevant information from *ab initio* calculations that are also routinely acquirable with experimental setups. The measurement of the fully differential momentum distribution of the ionized electron, i.e., of the photoelectron spectrum (PES), represents an effective tool that gives us the most complete information regarding the ionization of laser irradiated targets. In these experiments [82, 83], the ejected electrons are directed in an angle resolved time of flight mass spectroscopy, and their initial momenta and ejection angles are measured.

Since, the laser induced PESs can be routinely obtained in experiments, and carry relevant information about the studied system, this work focuses mainly on the calculation of this observable quantity.

The photoelectron spectra is obtained by projecting the propagated TDWF onto the exact scattering states of the laser targeted system:

$$\frac{\mathrm{d}P}{\mathrm{d}\vec{k}}(\vec{k};t) = \left|\langle\Psi_{\vec{k}}(\vec{r})|\Psi(\vec{r};t)\rangle\right|^2, \tag{6.63}$$

where $\Psi_{\vec{k}}(\vec{r})$ is the continuum wave function representing the exact scattering state of the ionised electron with momentum $\vec{k}$. The solution of Eq. (6.63) gives the probability density of finding an electron with momentum inside the $[\vec{k}, \vec{k}+\mathrm{d}\vec{k}]$ interval at the time moment $t$.

Due to the two-center nature of the diatomic molecule, the exact scattering states can be obtained only via numerically laborious procedures [84] (they do not have analytical form), hence in the present approach I have considered the one-center Coulomb wave functions which became identical with the exact continuum functions in the asymptotic region. This means that the used approximate states differ significantly from the exact ones only at the vicinity of the two nuclei, but they are the same at large electron distances. By calculating the ejected electron's position according to Equations (6.60)-(6.62) the obtained $\overline{r}(t)$ distance delivers us useful information regarding the departure of the ejected wave packet as a function of time.

The approximate PES calculated using one-center Coulomb wave functions can be brought near the exact one by further propagating in time the TDSE after the conclusion of the laser pulse ($\mathcal{T} > \tau$), since the slow momentum electrons will also have sufficient time to move away from that region (the neighborhood of the two nuclei) where their one-center Coulomb description is incorrect. A sufficiently large $\overline{r}(\mathcal{T}) \gg R$ distance of the continuum wave packet (the larger the ratio $\overline{r}/R$, the smaller the difference between the exact and approximate scattering states) may be used as an indicator for obtaining the convergent photoelectron spectrum.

By taking into account the aforementioned considerations, the projection of the TDWF onto the one center Coulomb wave function $[\Psi_{\vec{k}}(\vec{r}) \to \Psi_{\mathrm{C}}(\vec{k};\vec{r})]$ was employed. On the other hand, since the approximate scattering states $|\Psi_{\mathrm{C}}(\vec{k},\vec{r})\rangle$ are not orthogonal to the bound

states of the molecular target, and the $|\Psi(\vec{r};t)\rangle$ may have contributions from the BSs after the end of the laser pulse, undesired errors may appear in the PES image. In order to eliminate these artificial errors from the TDWF the bound states were removed according to Eq. (6.61) and the spectrum calculated for the continuum part of the wave function $\Psi(\vec{r};t) \to \Psi_{\text{free}}(\vec{r};t)$ as

$$\frac{\mathrm{d}P}{\mathrm{d}\vec{k}}(\vec{k};t) = \left|\langle\Psi_{\mathrm{C}}(\vec{k},\vec{r})|\Psi_{\text{free}}(\vec{r};t)\rangle\right|^2. \tag{6.64}$$

The $\Psi_{\mathrm{C}}(\vec{k},\vec{r})$ Coulomb wave functions, which describe the one-center continuum states of the electron with momentum $\vec{k}$, are obtained by solving the stationary Schrödinger equation for the hydrogen atom:

$$\left(-\frac{\nabla^2}{2} + \frac{\mathrm{Z}}{r}\right)\psi_{\vec{k}}(\vec{r}) = \frac{|\vec{k}|^2}{2}\psi_{\vec{k}}(\vec{r}), \tag{6.65}$$

where Z is the product of the electric charge of the electron and of the field source ($\mathrm{Z} = -1$ in the case of H), while $|\vec{k}|^2/2$ is the asymptotic energy of the electron.

The Coulomb wave function has the following analytical form [72]:

$$\Psi_{\mathrm{C}}(\vec{k},\vec{r}) = \frac{1}{\sqrt{(2\pi)^3}}\frac{1}{kr}\sum_{l=0}^{\infty}(2l+1)i^l e^{i\sigma_l}F_l(\gamma,kr)P_l(\cos\theta_{\vec{k},\vec{r}}), \tag{6.66}$$

where $\sigma_l = \mathrm{Arg}\left[\Gamma(l+i\gamma+1)\right]$ is the Coulomb-phase shift with the $\gamma = (e^2/4\pi\epsilon_0\hbar)Z_{\mathrm{A}}Z_{\mathrm{B}}(m_e/k)$ Sommerfeld parameter (in atomic units: $\gamma = Z_{\mathrm{B}}Z_{\mathrm{B}}/k$) and $\Gamma$ is the gamma function. $F_l(\gamma,kr)$ represents the regular Coulomb function and $\theta_{\vec{k},\vec{r}}$ the angle between the electron's position vector ($\vec{r}$) and its momentum ($\vec{k}$). The last term in Eq. (6.66) is the Legendre polynomial and can be expressed in terms of the spherical harmonics as

$$P_l(\cos\theta_{\vec{k},\vec{r}}) = \frac{4\pi}{2l+1}\sum_{m=-l}^{l}Y_{lm}(\theta,\varphi)Y^*_{lm}(\theta_k,\varphi_k). \tag{6.67}$$

where $Y_{lm}$ represents the spherical harmonic, while $\theta_k$ the polar angle and $\varphi_k$ the azimuthal angle of the momentum vector $\vec{k}$. By substituting Eq. (6.67) into Eq. (6.66) one obtains the Coulomb wave function as a function of the polar coordinates of the electron's position vector $\vec{r} \equiv \{r,\theta,\varphi\}$ and of its momentum $\vec{k} \equiv \{k,\theta_k,\varphi_k\}$:

$$\Psi_{\mathrm{C}}(\vec{k},\vec{r}) = \sqrt{\frac{2}{\pi}}\frac{1}{kr}\sum_{l=0}^{\infty}\sum_{m=-l}^{l}i^l e^{i\sigma_l}F_l(\gamma,kr)Y_{lm}(\theta,\varphi)Y^*_{lm}(\theta_k,\varphi_k). \tag{6.68}$$

### Calculating the PES when the laser field is polarised along the molecular axis

The calculation of the PESs will be simplified if the angle between the incident's electric field and the molecular axis is zero ($\theta_R$=0). In this case the couplings between different $\Psi^{(m)}$

channels in the TDSE will not be present ($\sin\theta_R = 0$), and only the initial channel of $\Psi^{(m=0)}$ will remain populated. This is happening due to the fact that the initial $|1s\sigma_g\rangle$ state obeys cylindrical symmetry, thus it is $\varphi$ independent, i.e. $m = 0$.

By introducing the notation $A(\vec{k};t)$ for the transition amplitude and using the previous statements the projection onto the continuum states gets simplified:

$$\begin{aligned} A(\vec{k};t) &= \langle\Psi_{\rm C}(\vec{k})|\Psi_{\rm free}(t)\rangle = \left\langle \Psi_{\rm C}(\vec{k}) \middle| \sum_{m=0}^{\infty} \Psi_{\rm free}^{(m)}(\xi,\eta;t)\frac{e^{im\varphi}}{\sqrt{2\pi}} \right\rangle \\ &= \frac{1}{\sqrt{2\pi}} \left\langle \Psi_{\rm C}(\vec{k}) \middle| \Psi_{\rm free}^{(m=0)}(\xi,\eta;t) \right\rangle, \end{aligned} \tag{6.69}$$

where inside the scalar product only the $\xi$ and $\eta$ integrations have to be calculated. Moreover, for this laser-molecule geometry the calculation of the Coulomb wave function is reduced as well, where in the general form [Equation (6.68)] the sum over $m$ is eliminated, next to the $\varphi_k$ dependence:

$$\Psi_{\rm C}(k,\theta_k;r,\theta) = \sum_{l=0}^{\infty} \sqrt{\frac{2}{\pi}}\frac{1}{kr} i^l e^{i\sigma_l} F_l(\gamma,kr) Y_{l0}(\cos\theta)\ Y_{l0}(\cos\theta_k). \tag{6.70}$$

By writing the transition amplitude formally in the expansion of the spherical harmonics $Y_{l0}(\cos\theta_k)$:

$$A(k,\theta_k;t) = \sum_{l=0}^{\infty} a_l(k;t) Y_{l0}(\cos\theta_k)^*, \tag{6.71}$$

the expansion coefficients

$$\begin{aligned} a_l(k;t) &= (2\pi)\int \mathrm{d}\xi \int \mathrm{d}\eta \frac{R^3}{8}(\xi^2-\eta^2) \left[\sqrt{\frac{2}{\pi}}\frac{1}{kr} i^l e^{i\sigma_l} F_l(\gamma,kr) Y_{l0}(\cos\theta)\right]^* \frac{\Psi_{\rm free}^{(0)}(\xi,\eta;t)}{\sqrt{2\pi}} = \\ &= \frac{R^3}{4}\int \mathrm{d}\eta \int \mathrm{d}\xi (\xi^2-\eta^2) \left[\frac{1}{kr} i^l e^{i\sigma_l} F_l(\gamma,kr) Y_{l0}(\cos\theta)\right]^* \Psi_{\rm free}^{(0)}(\xi,\eta;t) \end{aligned} \tag{6.72}$$

are calculated by using the Gauss quadratures:

$$a_l(k;t) = \frac{R^3}{4}\sum_i \omega_i^{\{\xi\}} \sum_j \omega_j^{\{\eta\}} (\xi_i^2-\eta_j^2) \left[\frac{1}{kr}(-i)^l e^{-i\sigma_l} F_l(\gamma,kr_{ij}) Y_{l0}(\cos\theta_{ij})\right] \Psi_{\rm free}^{(0)}(\xi_i,\eta_j;t), \tag{6.73}$$

where the following substitutions were also considered: $r_{ij} = \frac{R}{2}\sqrt{\xi_i^2+\eta_j^2-1}$; $\cos\theta_{ij} = \xi_i\eta_j/\sqrt{\xi_i^2+\eta_j^2-1}$.

## 6.7 A possible extension of the method: the inclusion of the nuclear motion

The method presented in this section for describing the laser induced EWP dynamics inside the molecule can be further advanced by the inclusion of the nuclear dynamics. When considering larger wavelength radiations (e.g., IR regime) depending on the field strength next to the rapid motion of the light electron the laser will also exerts the nuclei to start to vibrate.

In these circumstances the whole molecular system is described by the molecular Hamiltonian, which governs the time evolution of the molecular wave function:

$$i\frac{\partial}{\partial t}\Psi_{\mathrm{mol}}(\vec{R},\vec{r};t) = \left[\hat{H}_{\mathrm{e}} + \hat{H}_{\mathrm{n}} + \hat{U}_{\mathrm{int}}(t)\right]\Psi_{\mathrm{mol}}(\vec{R},\vec{r};t), \tag{6.74}$$

where $\vec{R}$ are the nuclear coordinates, $\hat{H}_e = -\Delta_e/2 - Z_{\mathrm{A}}/r_{\mathrm{A}} - Z_{\mathrm{B}}/r_{\mathrm{B}}$ is the electronic Hamiltonian with $r_{\mathrm{A}}$ and $r_{\mathrm{B}}$ being the distances measured from the nuclei with positive electric charge $Z_{\mathrm{A}}$ and $Z_{\mathrm{B}}$, respectively. $\hat{U}_{\mathrm{int}}(t)$ describes the interaction with the laser field, while the nuclear part of the Hamiltonian reads as

$$\hat{H}_{\mathrm{n}} = -\frac{\Delta_{\mathrm{A}}}{2M_{\mathrm{A}}} - \frac{\Delta_{\mathrm{B}}}{2M_{\mathrm{B}}} + \frac{Z_{\mathrm{A}}Z_{\mathrm{B}}}{R}, \tag{6.75}$$

where $M_1$ and $M_2$ represent the mass of the two nuclei. In the kinetic energy terms of the nuclei [first and second term of Eq. (6.75)] $\Delta_{\mathrm{A,B}} = \partial^2/\partial\vec{R}^2_{\mathrm{A,B}}$ is the Laplace operator, while the last $Z_{\mathrm{A}}Z_{\mathrm{B}}/R$ expression gives the electrostatic potential that repels the two nuclei separated by distance $R$.

Since the motion of the light electron is much pronounced (much faster) than of the nuclei, the Bohr-Oppenheimer approximation can be considered, and the time-dependent Close-Coupling (TDCC) method applied on the molecular wave function

$$\Psi_{\mathrm{mol}}(\vec{R},\vec{r};t) = \sum_i \sum_{v_i} d_{iv_i}(t)\varphi_i(\vec{r},R)\chi_{v_i}(R), \tag{6.76}$$

where the dynamics of the nuclei is detached from the motion of the electron. Moreover, in this TDCC approach the the molecular wave function is expressed in terms of $\chi_{v_i}(R)$ molecular vibrational states and $\varphi_i(\vec{r},R)$ electronic states, while the time dependence is separated into a separate variable (expansion coefficient) $d_{iv_i}(t)$. This picture takes into account that the motion of the nuclei is instantaneously effected by the actual distribution of the electron cloud that surrounds the molecule. It considers that the vibration of the nuclei ($\chi_{v_i}(R)$) follows the potential energy curve (or potential energy surface in the case of multi atomic systems) of the molecule defined with the function $\mathcal{E}_0(R)$, where $\mathcal{E}_0$ is the electron's lowest energy in the spatial configuration $R$ (i.e., when the distance between the two nuclei has the value $R$). In addition to this, during the interaction with the external field

laser induced nuclear vibrations may appear also on higher energy curves (electron energy levels), after a $\chi_{v_i} \to \chi_{v_j}$ $(j > i)$ transition was induced by the field. From the other point of view, as the nuclei change their position due to the modified electron distribution, the light electrons will adjust quickly their dynamics to the new nuclear configuration.

By introducing the molecular wave function Eq. (6.76) into the Schrödinger equation [Eq. (6.74)], and performing two integrations of the form $\int \mathrm{d}R\chi^*_{v_j}(R)$ and $\int \mathrm{d}\vec{r}\varphi^*_j(\vec{r};R)$ on both sides of the equation, the following expression for the expansion coefficients can be deduced (identical to the TDCC solution of the molecular TDSE):

$$\begin{aligned} i\frac{\partial}{\partial t}d_{jv_j}(t) &= \mathcal{E}_j(R)d_{jv_j}(t) + \frac{1}{R}d_{jv_j}(t) + \\ &+ \sum_i\sum_{v_i} d_{iv_i}(t) \underbrace{\int \mathrm{d}\vec{r}\varphi^*_j(\vec{r}) \int \mathrm{d}R\ \chi^*_{v_j}(R) \left[-\frac{\Delta_\mathrm{A}}{2M_\mathrm{A}} - \frac{\Delta_\mathrm{B}}{2M_\mathrm{B}}\right] \varphi_i(\vec{r})\chi_{v_i}(R)}_{T_{jv_jiv_i}} + \\ &+ \sum_i\sum_{v_i} d_{iv_i}(t) \underbrace{\int \mathrm{d}R\chi^*_{v_j}(R)\ \langle\varphi_j|\hat{U}_\mathrm{int}(t)|\varphi_i\rangle(R)\ \chi_{v_i}(R)}_{U_{jv_jiv_i}(t)}, \end{aligned} \tag{6.77}$$

where the $\langle\chi_{v_j}(R)|\chi_{v_i}(R)\rangle = \delta_{v_iv_j}$ and $\langle\varphi_j|\varphi_i\rangle = \delta_{ij}$ orthonormal properties have been used. By taking into account that dynamics of the molecule can be modelled by the vibration of the system's reduced mass ($\mu$) which is attached to a fixed wall by a 'string', the whole motion of the system can be included in the electron's kinetic potential by using the substitution $m_e \to \mu$, hence the nuclear kinetic energy term can be avoided from Eq. (6.77): $T_{jv_jiv_i} \to 0$. As a consequence, the coupled differential equation leads to the simplified form of:

$$i\frac{\partial}{\partial t}d_{jv_j}(t) = \left[\mathcal{E}_j(R) + \frac{1}{R}\right] d_{jv_j}(t) + \sum_i\sum_{v_i} d_{iv_i}(t) \int dR\chi^*_{v_j}(R)\ \langle\varphi_j|\hat{U}_\mathrm{int}(t)|\varphi_i\rangle_{(R)}\ \chi_{v_i}(R). \tag{6.78}$$

The crucial part of the present method is to obtain accurate and convergent $|\varphi_j(R)\rangle$ electronic bound states for a wide array of discretized $R_i$ internuclear separation points located in the $R_i \in (0, R_\mathrm{max})$ range ($R_\mathrm{max} < \infty$), and also precise values for the $\mathcal{E}_j(R)$ energy curves. Provided that, the calculated electronic bound states are the correct ones, also the laser induced transition amplitudes

$$\langle\varphi_j|\hat{U}_\mathrm{int}(t)|\varphi_i\rangle_{(R)} = \langle\varphi_j|\vec{r}\cdot\vec{E}(t)|\varphi_i\rangle_{(R)} \tag{6.79}$$

calculated within the dipole approximation and by using length gauge can be considered accurate (representing the essence of the present approach). Both the 'exact' bound states and the accurate energy curves can be obtained after performing rigorous convergence tests by orthogonalization the efficiently constructed $\hat{H}(0)$ Hamiltonian matrix [i.e., Eq. (6.30) after setting $t \to 0$].

CHAPTER 7.

# The $H_2^+$ molecule in ultrashort XUV laser fields

## 7.1 Numerical details

This section is dedicated to the numerics, where first, the numerical parameters of the spacial discretization of the wave function and Hamiltonian will be reviewed. Second, in parallel with the previous one, the numerical details regarding the time propagation will be discussed.

Since in the case of grid representation based numerical simulations the whole laser induced dynamics of the investigated quantum system is restricted into a finite space, i.e., simulation box, the size of this 'box' should be correctly chosen. This means that the grid size should be sufficiently large in order to include all the relevant physical processes taking place during the action of the oscillating field. Considering that the used laser field is an ultrashort XUV pulse and by taking into account the values of the ionization potential of the molecule in the range $R \in (1 \text{ a.u.}, 4 \text{ a.u.})$ at the first attempt the size of the simulation box was considered to be sufficiently large when $r_{\max} \simeq 600$ a.u., which value is directly related to the $\xi_{\max}$ parameter through the relation $\xi_{\max} = 2r_{\max}/R$. The space in which the $\eta = (r_A - r_B)/R$ coordinate is chosen is given by definition: $\eta \in [-1, 1]$. In order to avoid the singularities appearing in the Hamiltonian operator when $\eta = \pm 1$, in the first and last finite element (FE) of the $\eta$ grid the Gauss-Radau quadrature points (only one endpoint of the FE is a gridpoint) were used. For the remaining (non-edge) $\eta$ FEs' both edge points were chosen as quadrature points: resulting that $\eta_{N_{\text{fun}}}^{FE_i} \equiv \eta_1^{FE_{i+1}}$. This was done by using the so-called *Gauss-Radau quadratures*. The similar considerations were done in the case of the $\xi$ grid, whereas only for the first FE were used Gauss-Legendre points to avoid the singularity at $\xi \to 1$.

Another important parameter is the grid density of both the $\xi$ and $\eta$ grids. The density of the $\xi$ grid was deduced from the desired $\Delta r$ input parameter, where for the total number of $\xi$ gridpoints the $N_\xi$ is given as the integer part of $r_{\max}/\Delta r$. From $N_\xi$ and from the fixed number of the interpolating polynomials $N_{\text{fun}}^{\{\xi\}} = N_{\text{fun}}^{\{\eta\}} = 7$ the total number of FEs on the $\xi$ grid was obtained. These $\xi$ FEs were distributed evenly by using OpenMPI parallelization

on a multi-CPU platform. If the obtained value for the total number of $\xi$ FEs could not be allocated evenly on the requested number of CPUs, the value of $r_{\max}$ was increased until this optimal partition could have been performed. For the $\eta$ grid 0.1 sized FEs were used, which gives an average $\Delta\eta = 0.1/\mathrm{N}_{\mathrm{fun}}^{\{\eta\}} \simeq 0.014$ average $\eta$ grid density.

During the numerical integration of the time-dependent wave function, depending on the laser field's parameters, at a given time moment the larger velocity part of the continuum electronic wave packets may reach the edges of the simulation box. Since, in the present case the prolate spheroidal coordinates were used, this may occur only at a single endpoint, at the truncated value of the $\xi$ coordinate space, i.e. at $\xi = \xi_{\max} < \infty$. Reaching the boundary the wave function will be reflected, which will produce unphysical features in the calculated photoelectron spectra. In order to eliminate these undesired reflections from the edge of the simulation grid a complex absorbing potential (CAP) was introduced which was defined as:

$$V_{\mathrm{CAP}} = -i \exp\left[\alpha_{\mathrm{absorb}} \log\cos\frac{\xi - \xi_{\mathrm{cut}}}{\xi_{\max} - \xi_{\mathrm{cut}}}\right], \text{ for } \xi \geq \xi_{\mathrm{cut}}, \tag{7.1}$$

where by setting $\xi_{\mathrm{cut}} = 95\%\xi_{\max}$ we ensured that the CAP acts only on the outermost part of the TDWF. The value of the absorbing coefficient was set to $\alpha_{\mathrm{absorb}} = 10^6$. The proper size of the $\xi$ simulation box was ensured by keeping the norm of the absorbed part of the wave function below $10^{-10}$.

## 7.2 Electronic bound states and energies of $H_2^+$

The starting point of our investigation lies in the fact that for the correct solution of the TDSE, first, the accurate initial value of the wave function should be obtained [i.e., the electronic ground state's wave function: $\Psi(\vec{r}; t = 0) = \varphi_0 = \varphi_{1s\sigma_g}(\vec{r})$]. Moreover, in order to acquire information (during the time propagation procedure) related to the population of the excited bound states, also the wave function and energies of these states should be obtained with a sufficiently high accuracy.

In order to fulfill these requirements, the discretized version of the field-free electronic Hamiltonian (6.21) matrix is orthogonalized after setting $t \to 0$ in the matrix from of $\hat{H}(t)$ [Eq. (6.30)], i.e., when the laser field is absent: $U(t) = E(t) = 0$. In order to obtain correct results the optimal values for the numerical parameters of the wave function representation should be identified, i.e., the optimal values of $\Delta r$, $\Delta\eta$, and $r_{\max}$. During the diagonalization of the large-sized (typically consisting of more than $10^6 \times 10^6$ elements) time-independent $H(0)$ Hamiltonian matrix using parallelized procedures built in the SLEPc library package [85] a few hundreds of bound state wave functions could be obtained in a relatively short time: ranging from few tens of minutes up to several hours. Obviously, the requested CPU time for the diagonalization procedure practically depends on the size of the matrix (i.e., on the grid size and grid density), the number of requested eigenfunctions, and the number of employed CPUs.

### 7.2.1 Identification of bound state symmetry

Once the requested bound state wave functions were obtained, the symmetry property of each eigenstate was identified in the following way. First, the calculated complex eigenfunctions were rotated into the real plane by applying on them the

$$\hat{R}(-\alpha_j) = e^{-i\alpha_j(\vec{r})} \tag{7.2}$$

rotation operator, where $\alpha_j = \mathrm{Arg}[\varphi_j] = -\epsilon_j$ [1] is the argument of the $\varphi_j(\vec{r})$ complex function associated with the bound state with energy $\epsilon_j$.

Since $\alpha_j$ has the same value for all $\vec{r}_k \to \{\xi_k, \eta_k\}$ gridpoints, after the multiplication with $\hat{R}(-\alpha_j)$ each complex number written in the general form of $\varphi_i(\vec{r}_k) = |\varphi_i(\vec{r}_k)| \cdot e^{i\mathrm{Arg}[\varphi_i(\vec{r}_k)]}$ will have only real part (the imaginary part vanishes). Second, the number of the radial ($n_\xi$) and angular ($n_\eta$) nodal planes of each rotated

$$\varphi_j^{\mathrm{RE}}(\vec{r}) = \hat{R}(-\alpha_j)\varphi_j(\vec{r}) \tag{7.3}$$

real wave function was counted in the prolate coordinates, from which the symmetry of the investigated bound state was directly obtained: i.e., the principle and the azimuthal quantum numbers are given by the relations $n = n_\xi + n_\eta + 1$ and $l = n_\eta$, where $n_\xi$ and $n_\eta$ are the number of nodal planes counted inside the intervals $\xi \in [1, \xi_{\max} \to \infty]$ and $\eta \in [-1, 1]$, respectively. In the prolate spheroidal coordinate system these symmetry properties translate to the WF patterns illustrated in Fig. 7.1/(I), where the "+" indicates positive, while the "-" sign negative $\varphi^{\mathrm{RE}}$ wave function values. The Fig. 7.1/(II) shows the contour-plot of the calculated $4d\sigma_g$ state's wave function in the $(\xi, \eta)$ coordinate system.

In Figure 7.2 the $\varphi_j^{\mathrm{RE}}(\vec{r})$ wave functions of the first six energy level bound states are plotted along the $0z'$ molecular axis for the $R = 2$ a.u. internuclear separation [the nuclear coordinates are: $(x, y, z) \equiv (0, 0, \pm R/2)$]. The plots were done after the electronic wave functions had been transformed from the prolate spheroidal coordinate system into the Cartesian coordinate system. As it was expected the wave functions are concentrated in the vicinity of the two nuclei, and by the increase of the bound energies the spread of the wave functions also increases. A second straightforward observation is that at infinite distances ($r \to \pm\infty$) all the wave functions tend to zero. By considering the symmetry properties of the wave functions, it can be observed, that the wave functions of the *ungerade* states ($2p\sigma_u$, $3p\sigma_u$, etc.) cross the $0z'$ molecular axis at the value $z' = 0$ (i.e., $r_{\mathrm{A}} = r_{\mathrm{B}} = R/2$) where $\varphi_j(z' = 0) = 0$, while for the *gerade* states ($1s\sigma_g$, $2s\sigma_g$, $3s\sigma_g$, $3d\sigma_g$, etc.) when $z' = 0$ the wave functions have non-zero values.

[1] This property can be proven by solving the time-independent Schrödinger equation $i\frac{\partial}{\partial t}\varphi = \hat{H}_0\varphi$ which leads to $\varphi(\vec{r};t) = e^{-i\hat{H}_0(t-t_0)}\varphi(\vec{r};t) \to \varphi_j(\vec{r};t) = e^{-i\epsilon_j(t-t_0)}\varphi_j(\vec{r};t_0)$. This results that the phase of the bound state wave function is independent on the coordinate. In the expression of the coordinate independent argument the $t = t_0 + 1$ time moment was considered.

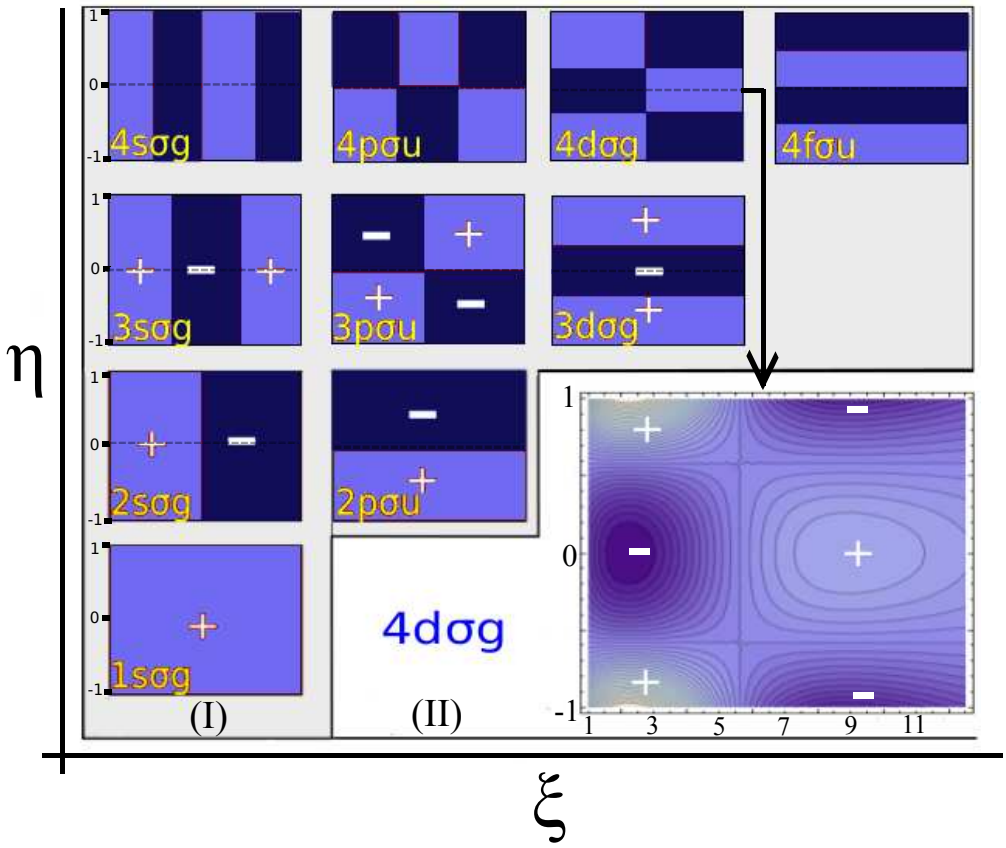


Figure 7.1: (I) The distribution of positive and negative regions in the $(\xi, \eta)$ prolate spheroidal coordinates of the $\varphi^{\mathrm{RE}}$ wave functions starting from the symmetry $n = 1$ up-to 4 (inclusive). (II) The contour-plot image of the calculated $4d\sigma_g$ state's wave function ($R = 2$ a.u.).

### 7.2.2 The convergence of bound state energies and wave functions

All these bound states and bound state energies were obtained after performing rigorous convergence tests as illustrated in the table (Fig 7.3) below, where the results obtained for the equilibrium distance $R = 2$ a.u., for a smaller $R = 0.1$ a.u. and for a larger $R = 12$ a.u. internuclear separation are shown. The convergence of the eigenfunctions are illustrated only for the case of equilibrium distance ($R = 2$ a.u.) and for the ground ($1s\sigma_g$), the first excited ($2p\sigma_u$) and for two other low-lying bound states ($4d\sigma_g$, $4f\sigma_u$) as a function of average radial grid density.

The results were considered convergent, if the relative differences of the calculated eigenenergies in the $i^{th}$ step satisfied the condition $\delta^{\mathcal{E}}_{\mathrm{rel}} < 10^{-4}$, where

$$\delta^{\mathcal{E}}_{\mathrm{rel}} = \frac{|\mathcal{E}^{(i)} - \mathcal{E}^{(i-1)}|}{|\mathcal{E}^{(i)}|}. \tag{7.4}$$

The $(i+1)$-th step labels the values calculated with the new parameters obtained by modifying the parameters used in the $i$-th step: i.e., in the case of grid density parameters, $\Delta r$ and $\Delta\eta$ were gradually decreased, while in the case of the simulation box size, $r_{\max}$ was gradually

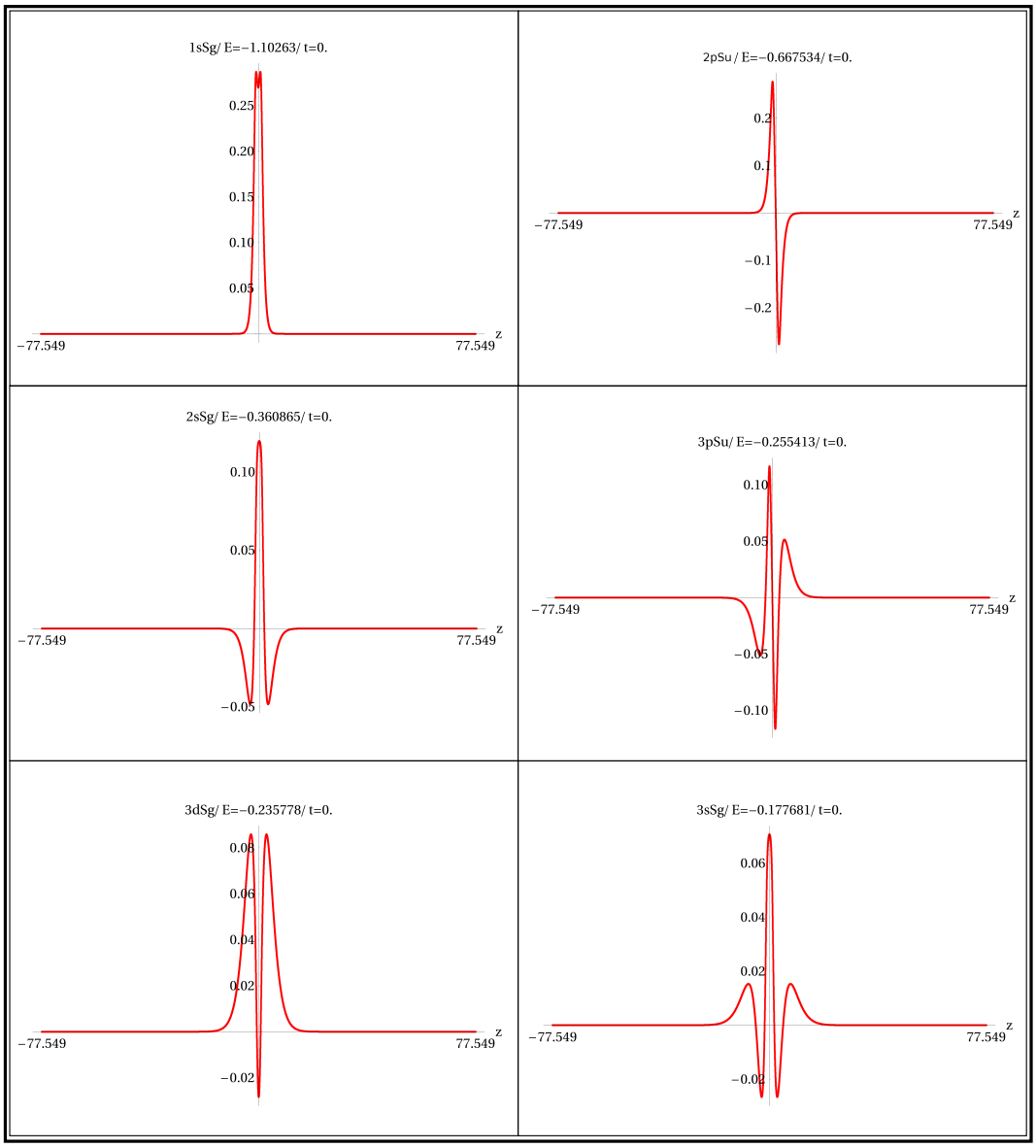


Figure 7.2: The first six electronic bound states' wave function and bound energies of the $H_2^+$ molecule obtained by diagonalizing the field-free Hamiltonian for the equilibrium internuclear separation $R = 2$ a.u.. The plots show the $\varphi_i(\vec{r})$ wave functions rotated into the real plane.

increased.

By looking at the wave functions in Figure 7.4, at first sight it can be observed that a very fast convergence as a function of $\Delta r$ was obtained at the tails of the wave functions, i.e., at distant regions from the nuclei. This high convergence was less pronounced in the vicinity of the two cores especially in the region between the two protons. By zooming into these closer regions, as illustrated in the insets of the $1s\sigma_g$ ground state [Fig 7.4(a)] and $4f\sigma_u$ excited state [Fig 7.4(d)], a convenient convergence was confirmed for these cases as well, proving that the calculated bound states' wave functions can be obtained with high accuracy by working with the optimal numerical parameters.

By taking into account the presented results, we may conclude that the implemented numerical method is applicable for calculating high accuracy convergent eigenenergies and

| R = 0.1 a.u. | | 1sσg | | 2pσu | | 4dσg | | 4fσu | |
|---|---|---|---|---|---|---|---|---|---|
| | | Energy [a.u.] | δrel | Energy[a.u.] | δrel | Energy[a.u.] | δrel | Energy[a.u.] | δrel |
| $\overline{\Delta r}$ [a.u.] (Δη≈6e-3) ($r_{max}$=48.1 a.u.) | 1 | -1.994245 | | -0.500554 | | -0.124863 | | -0.124957 | |
| | 0.85 | -1.983562 | 5e-3 | -0.500484 | 1e-4 | -0.124982 | 1e-3 | -0.124985 | 2e-4 |
| | 0.75 | -1.980064 | 2e-3 | -0.500491 | 1e-5 | -0.12501 | 2e-4 | -0.124997 | 1e-4 |
| | 0.6 | -1.978896 | 6e-4 | -0.500524 | 7e-5 | -0.125015 | 4e-5 | -0.125001 | 3e-5 |
| | **0.5** | **-1.978311** | **3e-4** | **-0.500612** | **2e-4** | **-0.125013** | **2e-5** | **-0.125004** | **2e-5** |
| $r_{max}$ [a.u.] (Δη≈6e-3) (Δr≈5e-2) | R+28 | -1.978431 | | -0.500571 | | -0.124997 | | -0.124976 | |
| | R+38 | -1.978332 | 5e-5 | -0.5006 | 6e-5 | -0.125004 | 6e-5 | -0.125004 | 2e-4 |
| | **R+48** | **-1.978354** | **1e-5** | **-0.500591** | **2e-5** | **-0.125013** | **7e-5** | **-0.125003** | **8e-6** |
| | R+58 | -1.978321 | 2e-5 | -0.500605 | 3e-5 | -0.125014 | 8e-6 | -0.125004 | 8e-6 |
| $\overline{\Delta\eta}$ (Δr≈5e-2) ($r_{max}$=48.1 a.u.) | **6e-2** | **-1.978311** | **<1e-5** | **-0.500612** | **<1e-5** | **-0.125013** | **<1e-5** | **-0.125004** | **<1e-5** |
| | 3e-2 | -1.978311 | <1e-5 | -0.500612 | <1e-5 | -0.125013 | <1e-5 | -0.125004 | <1e-5 |
| | 1.5e-2 | -1.978311 | | -0.500612 | | -0.125013 | | -0.125004 | |
| **R = 2 a.u.** | | **1sσg** | | **2pσu** | | **4dσg** | | **4fσu** | |
| | | **Energy [a.u.]** | **δrel** | **Energy[a.u.]** | **δrel** | **Energy[a.u.]** | **δrel** | **Energy[a.u.]** | **δrel** |
| $\overline{\Delta r}$ [a.u.] (Δη≈6e-3) ($r_{max}$=50 a.u.) | 1 | -1.102702 | 2.2e-4 | -0.667521 | 0.2e-4 | -0.130674 | 1.2e-3 | -0.126623 | 1.4e-4 |
| | 0.85 | -1.102649 | 0.4e-4 | -0.667521 | 0.8e-4 | -0.130748 | 0.5e-3 | -0.126634 | 0.8e-4 |
| | 0.75 | -1.102638 | 0.1e-4 | -0.667518 | <1e-5 | -0.130777 | 2.2e-4 | -0.126639 | 0.4e-4 |
| | 0.6 | -1.102634 | 0.3e-5 | -0.667515 | <1e-5 | -0.130791 | 1.0e-4 | -0.126643 | 0.3e-4 |
| | **0.5** | **-1.102632** | **0.1e-5** | **-0.667519** | **<1e-5** | **-0.130792** | **0.7e-5** | **-0.126644** | **0.7e-5** |
| $r_{max}$ [a.u.] (Δη≈6e-3) (Δr≈5e-2) | R+28 | -1.102632 | <1e-5 | -0.66752 | <1e-5 | -0.130783 | 0.8e-3 | -0.126642 | |
| | R+38 | -1.102632 | | -0.66752 | | -0.130792 | 0.6e-4 | -0.126644 | 1e-5 |
| | **R+48** | **-1.102632** | **<1e-5** | **-0.66752** | **<1e-5** | **-0.130792** | **<6e-5** | **-0.126644** | **<1e-5** |
| | R+56 | -1.102632 | <1e-5 | -0.66752 | <1e-5 | -0.130792 | <6e-5 | -0.126644 | <1e-5 |
| $\overline{\Delta\eta}$ (Δr≈5e-2) ($r_{max}$=50 a.u.) | **6e-2** | **-1.102632** | **<1e-5** | **-0.66752** | **<1e-5** | **-0.130792** | **<1e-5** | **-0.126644** | **<1e-5** |
| | 3e-2 | -1.102632 | <1e-5 | -0.66752 | <1e-5 | -0.130792 | <1e-5 | -0.126644 | <1e-5 |
| | 1.5e-2 | -1.102632 | | -0.66752 | | -0.130792 | | -0.126644 | |
| **R = 12 a.u.** | | **1sσg** | | **2pσu** | | **4dσg** | | **4fσu** | |
| | | **Energy [a.u.]** | **δrel** | **Energy[a.u.]** | **δrel** | **Energy[a.u.]** | **δrel** | **Energy[a.u.]** | **δrel** |
| $\overline{\Delta r}$ [a.u.] (Δη≈6e-3) ($r_{max}$=60 a.u.) | 1 | -0.583503 | <1e-5 | -0.583393 | <1e-5 | -0.136406 | <1e-5 | -0.192088 | <1e-5 |
| | 0.85 | -0.583503 | | -0.583393 | | -0.136405 | | -0.192088 | |
| | 0.75 | -0.583503 | | -0.583393 | | -0.136405 | | -0.192088 | |
| | 0.6 | -0.583503 | | -0.583392 | | -0.136405 | | -0.192088 | |
| | **0.5** | **-0.583502** | **2e-6** | **-0.583392** | **<1e-5** | **-0.136405** | **<1e-5** | **-0.192088** | **<1e-5** |
| $r_{max}$ [a.u.] (Δη≈6e-3) (Δr≈5e-2) | R+28 | -0.583502 | <1e-5 | -0.583392 | <1e-5 | -0.136405 | 0.7e-5 | -0.192088 | <1e-5 |
| | R+38 | -0.583502 | | -0.583392 | | -0.136405 | <1e-5 | -0.192088 | |
| | **R+48** | **-0.583502** | **<1e-5** | **-0.583392** | **<1e-5** | **-0.136405** | **<1e-5** | **-0.192088** | **<1e-5** |
| | R+58 | -0.583502 | <1e-5 | -0.583392 | <1e-5 | -0.136405 | <1e-5 | -0.192088 | <1e-5 |
| $\overline{\Delta\eta}$ (Δr≈5e-2) ($r_{max}$=60 a.u.) | **6e-2** | **-0.583502** | **<1e-5** | **-0.583392** | **<1e-5** | **-0.136405** | **<1e-5** | **-0.192088** | **<1e-5** |
| | 3e-2 | -0.583502 | <1e-5 | -0.583392 | <1e-5 | -0.136405 | <1e-5 | -0.192088 | <1e-5 |
| | 1.5e-2 | -0.583502 | | -0.583392 | | -0.136405 | | -0.192088 | |

Figure 7.3: The energy convergence of the ground state ($1s\sigma_g$), the first excited state (in the $R = 2$ a.u. configuration: $2p\sigma_u$) and for two other low-lying bound states ($4d\sigma_g$, $4f\sigma_u$) as a function of the numerical parameters for different internuclear separations: $R \in \{0.1, 2, 12\}$ atomic units. The highlighted rows correspond to the convergent values within the $\sim 10^{-5}$ relative error.

eigenfunctions [86] of the $H_2^+$ molecule, providing accurate initial state wave function for the time-dependent Schrödinger equation as well. Based on this argument, further essential calculations become feasible: such as the calculation of transition dipole moments [Eq. (6.79)] or potential energy curves (in Figure 7.5 of the next subsection).

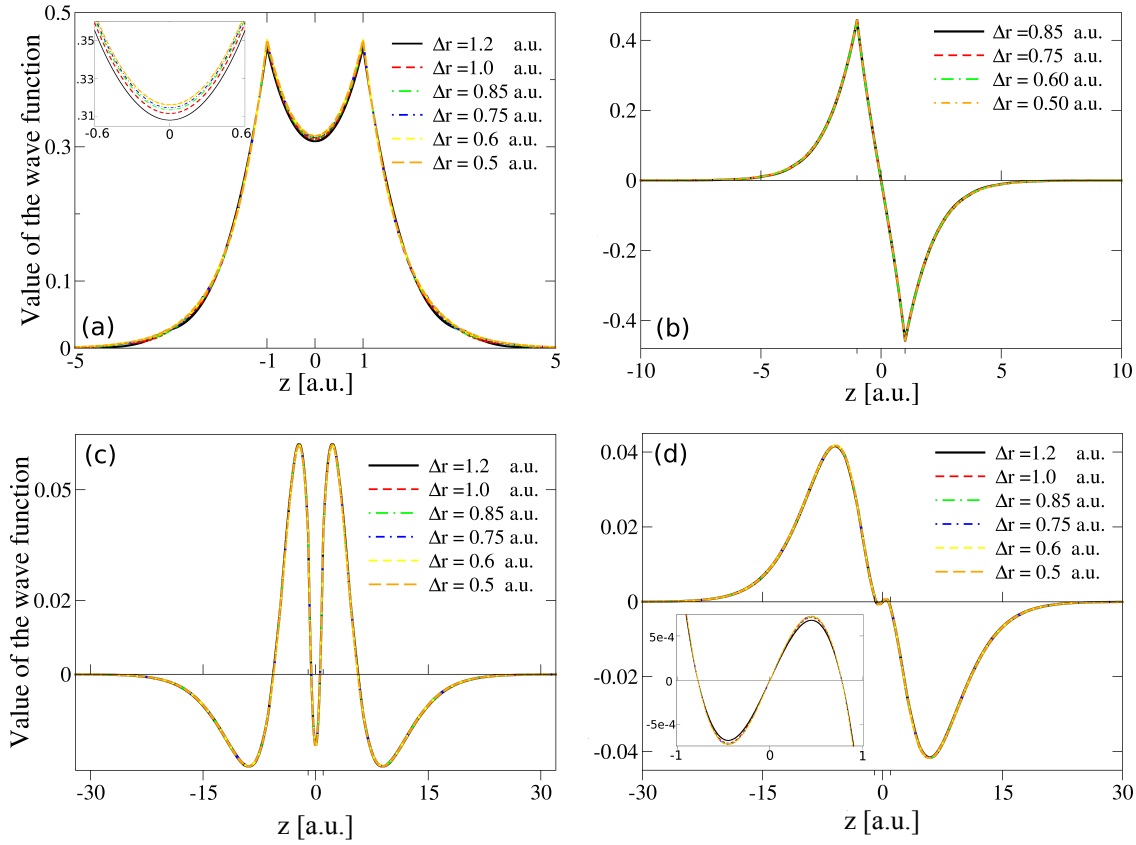


Figure 7.4: The convergence of the equilibrium ($R = 2$ a.u.) electronic wave functions along the internuclear axis as a function of the average radial grid density $\Delta r$. (a) The $1s\sigma_g$ ground state of $H_2^+$ and its zoom image at the vicinity of $z = 0$; (b) the first excited state $2p\sigma_u$; (c) $4d\sigma_g$ state ; (d) $4f\sigma_u$ and a zoom image at the vicinity of $z = 0$ ($r_{\max} = R + 48$ a.u., $\Delta\eta = 6 \times 10^{-3}$).

### Potential energy curves and electronic transition dipole moments

The potential energy curve of the $H_2^+$ molecule for a given electronic state can be calculated as $\mathcal{E}(R) + 1/R$ (with the last term giving the proton-proton repulsion energy) were compared to the reference data found in the literature [87]. As one can see the energies obtained within the present model fit perfectly the data obtained by the other approach, where a B-spline DVR method was used for the representation of the electronic wave function. As it was expected, only the $1s\sigma_g$ state has a minimum point at $R = 2$ a.u., which gives the equilibrium distance of the molecule. On the higher states the energy of the molecule constantly decreases, which brings the molecule into a dissociative state (since $R$ will tend to infinity).

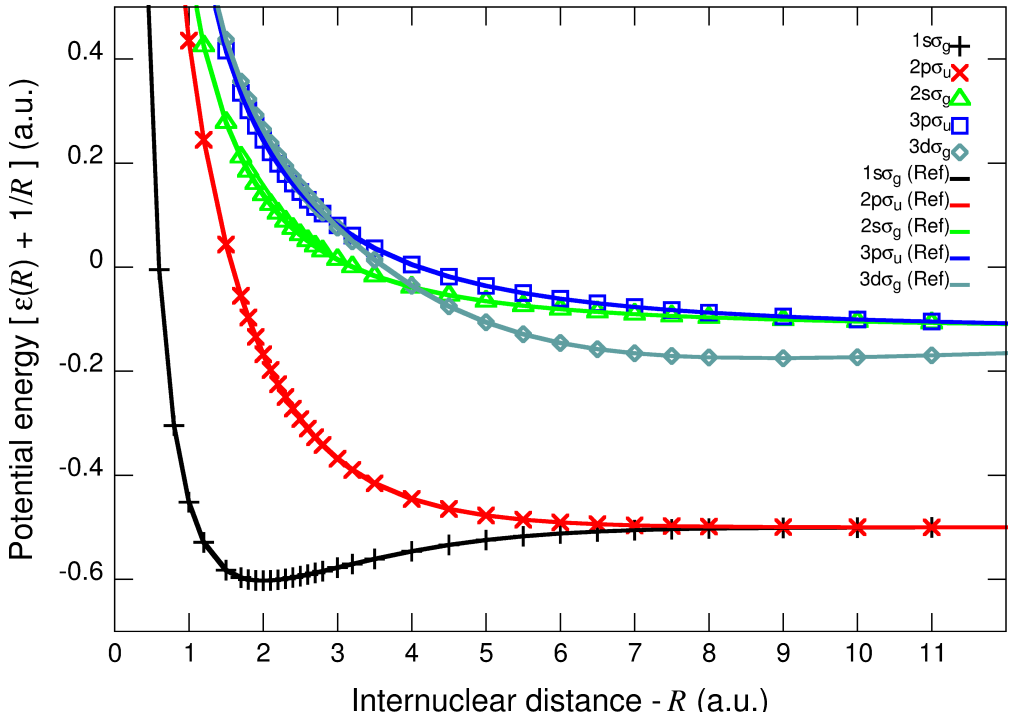


Figure 7.5: The calculated energy curves for different bound states plotted next to the reference data (colored solid lines) [87].

Another application of the convergent wave functions is the calculation of the electronic transition dipole moments, which are computed by evaluating the following integral for the transition matrix element:

$$\vec{\mu}_{ji} = \langle\varphi_j|(q\vec{r})|\varphi_i\rangle = -\langle\varphi_j|\vec{r}|\varphi_i\rangle = -\int \mathrm{d}\vec{r}\ \varphi_j^*(\vec{r})\vec{r}\varphi_i(\vec{r}). \tag{7.5}$$

The calculation of these values represents the essential part of the TDCC approach presented in the final part of the previous section, where the possibility of the inclusion of the nuclear dynamics was discussed. The values of the transition dipole moments

$$\vec{\mu}_{ji} = -\langle\varphi_j|x|\varphi_i\rangle\hat{i} - \langle\varphi_j|y|\varphi_i\rangle\hat{j} - \langle\varphi_j|z|\varphi_i\rangle\hat{k} \tag{7.6}$$

were calculated using the prolate spheroidal coordinates [$x = \sqrt{(\xi^2-1)(1-\eta^2)}\cos(\varphi)$, $\sqrt{(\xi^2-1)(1-\eta^2)}\sin(\varphi)$, $z = (R/2)\xi\eta$] for different internuclear configurations and listed here for the transition from the $|\varphi_i\rangle \equiv |1s\sigma g\rangle$ ground state to the first excited $|\varphi_j\rangle \equiv |2p\sigma u\rangle$ state. The aforementioned transition is one of the most relevant quantity in the one photon excitation process. In this case, since $\varphi_{1s\sigma g}$ is an even (*gerade*), while $\varphi_{2p\sigma u}$ an odd (*ungerade*) function only the integral

$$\vec{\mu}_{2p\sigma u,1s\sigma g} = -\langle\varphi_{2p\sigma u}|z|\varphi_{1s\sigma g}\rangle\hat{k} = -\frac{R}{2}\langle\varphi_{2p\sigma u}|\xi\eta|\varphi_{1s\sigma g}\rangle\hat{k} \tag{7.7}$$

will give non-zero value as a result, since the product of the $z = (R/2)\xi\eta$ odd function with the odd product of $\varphi_{2p\sigma u}(\xi,\eta)^* \cdot \varphi_{1s\sigma g}(\xi,\eta)$ results in a even integrand; while when calculating the $x$ and $y$ components of $\vec{\mu}$ the three-functions-product will be odd, because $x$ and $y$ are even functions of $\eta$. The transition dipole moments from Eq. (7.7) calculated for different internuclear distances are listed in Table 7.1. As it can be seen, by increasing the internuclear distance this coupling is increased, meaning that the laser induced transition from the ground to the first excited state will be more pronounced for larger proton-proton distances where the energies of the two states are getting closer to each other (as it can be observed on the potential energy curves in Fig. 7.5).

Table 7.1: The electronic transition dipole moment calculated for the first two energy level states ($\mu_{2p\sigma_u,1s\sigma_g}$) as a function of proton-proton distance $R$.

| Internuclear distance $R$ (a.u.) | Transition dipole moment $[1s\sigma_g \rightarrow 2p\sigma_u]$ (a.u.) |
|---|---|
| 0.10 | 0.38857 |
| 0.20 | 0.39730 |
| 0.40 | 0.45116 |
| 0.60 | 0.51956 |
| 0.80 | 0.59599 |
| 1.00 | 0.67533 |
| 1.50 | 0.86769 |
| 2.00 | 1.04034 |
| 2.50 | 1.23582 |
| 3.00 | 1.43237 |
| 3.50 | 1.64334 |
| 4.00 | 1.86835 |
| 5.00 | 2.35395 |
| 6.00 | 2.86733 |
| 7.00 | 3.38807 |
| 8.00 | 3.90586 |
| 9.00 | 4.41810 |
| 10.00 | 4.92524 |
| 11.00 | 5.42828 |
| 12.00 | 5.95518 |

## 7.3 XUV laser induced electron dynamics - Photoexcitation of $H_2^+$

In the present case, where the main and final goal is to investigate the physics behind the creation of the holographic image of the $H_2^+$ molecule created with photoelectrons, it is more appropriate to restrict our calculations to laser pulses having shorter wavelengths, i.e., by considering XUV radiations. This statement holds, since in the case when larger wavelengths are used also the field's periods are longer, hence more electron wave packets will be emitted in the continuum on different time moments of the same optical half-cycle resulting in a rather complex electron trajectory mechanism and interference patterns, which are more difficult to be deciphered.

In accordance with this, a two-cycle laser field having angular frequency $\omega_{\text{XUV}} = 0.4445$ a.u.t.$^{-1}$ was chosen from the XUV regime, where $\omega$ corresponds to a $\lambda \approx 100$ nm ($\nu =$ 2.92 PHz=$2.92 \times 10^{15}$ s$^{-1}$) central wavelength radiation and a.t.u. stands for the "atomic unit of time" (in the following abbreviated simply by "a.u.") equal to 24.2 as ($= 24.2 \times 10^{-18}$ s). The temporal profile of the linearly polarized laser field's electric component corresponds to the expression already given in Equation (6.11)

$$\vec{E}(t) = \begin{cases} \hat{\varepsilon} E_0 \sin\left(\omega_{\text{XUV}} t + \varphi_{\text{CEP}}\right) \sin^2\left(\frac{\pi t}{\tau}\right), & \text{if } t \in [0, \tau], \\ 0, & \text{otherwise,} \end{cases} \tag{7.8}$$

where $\hat{\epsilon} = (0, 0, \epsilon_z = 1)$ is the polarization vector of the electric field, the pulse duration $\tau$ was fixed to the value 28.27 a.u ($\sim 684$ as), while in order to obtain a symmetric waveform in time (see Fig. 7.6) the carrier-envelope phase was fixed to $\varphi_{\text{CEP}} = -\omega_{\text{XUV}}\tau/2 - \pi/2 \simeq -7.85$.

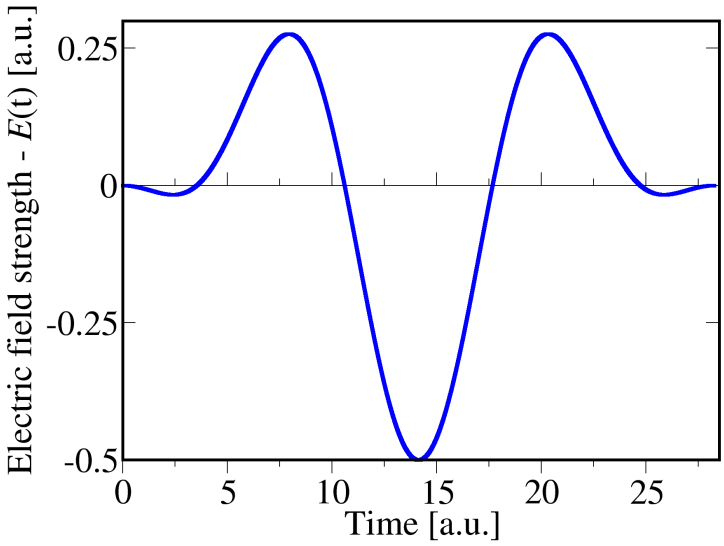


Figure 7.6: The temporal shape of the laser's electric field component with $E_0 = 0.5$ a.u. field amplitude. The angular frequency of the laser field is $\omega_{\text{XUV}} = 0.4445$ a.u., the pulse duration $\tau = 28.27$ a.u., while $\varphi_{\text{CEP}} = -7.85$.

For such an ultrashort laser pulse the motion of the heavy nuclei, which is relatively slow next to the rapid movement of the light electron, can be safely neglected, and hence the fixed nuclei approximation employed. In order to obtain useful information regarding how the value of the internuclear distance ($R$) influences the photoelectron spectrum of the target, we chose three different $R$ values for this study. The following investigations were carried out for a smaller internuclear distance $R = 1$ a.u., for the equilibrium distance $R = 2$ a.u., and for a larger proton-proton separation of $R = 4$ a.u..

The ionization energies of the electron emitted from the $1s\sigma_g$ ground state of the considered internuclear configurations were calculated and listed in Table 7.2.

Table 7.2: The ionization energy of the electron from the $1s\sigma_g$ state for different internuclear separations.

| $R$ [a.u.] | Ionization energy - $I_p$ [a.u.] |
|---|---|
| 1.0 | 1.45178631 |
| 2.0 | 1.10263421 |
| 4.0 | 0.7960848 |

The laser induced photoexcitation processes as a function of field amplitude were investigated [88] for these three different internuclear separations. Since, for the dynamics of the bound states' population a similar behavior was observed in all the three cases, here only the occupation probabilities (OPs) obtained for the $R = 2$ a.u. (equilibrium) distance will be discussed in more details. In order to follow this line of inquire, the $H_2^+$ molecule in its equilibrium configuration was irradiated with laser fields having the same frequency and pulse duration, but different peak intensities [i.e., different $E_0$ electric field amplitudes, see Figure 7.7(a)].

Once the accurate wave functions of the bound states were obtained by employing the numerical methods presented in the previous - theory - section, the population dynamics of numerous ($\sim 100 - 200$) bound states were investigated and the occupation probabilities of a few low-lying states plotted on Figure 7.7(b).

The used field intensities $E_0 \in \{0.25, 0.5, 0.75, 1\}$ a.u. were selected in such a way that the Keldysh parameter $\gamma$ [Eq. (3.7)] was kept near the value of 1, i.e., not far from the transition zone between the multi-photon and tunneling regime, since this region is where the most interesting physical processes are taking place, and which represents one of the most investigated area (especially in plasmonic field enhancement studies [82, 83]). In the limit of extremely high field intensities ($\gamma \ll 1$) already the maximum of the first optical half-cycle would fully ionize the target, thus further ejected electron wave packets would be very improbable to be emitted on a later time moment of the oscillating field. Therefore, this will result in a very 'poor' or featureless photoelectron holographic image of the target.

By taking a quick look at the population dynamics of the first four low-lying bound states in Figure 7.7(b), it can be seen that for the case of the relatively high field intensity ($E_0 = 1$ a.u.; $\gamma \approx 0.7$), already in the vicinity of the first important field maximum at time

$t \simeq 8$ a.u., the ground state is almost totally depleted, i.e. its occupation probability has fallen below the value $10^{-1}$. In parallel to this, the higher level bound states were rapidly populated.

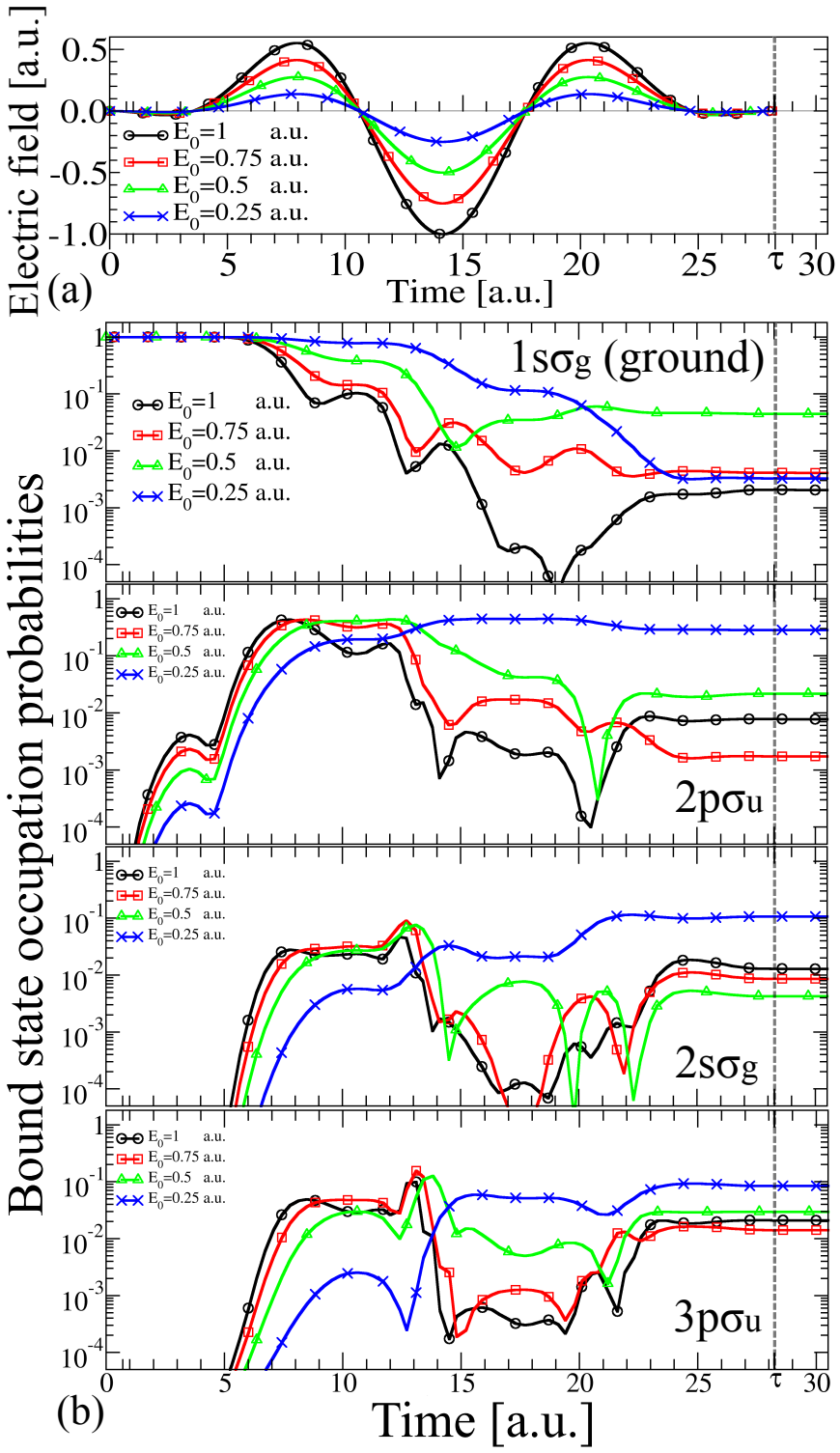


Figure 7.7: (a) The temporal shape of the laser's electric field component for different $E_0$ field amplitudes. (b) The occupation probabilities on logarithmic scale of the first 4 bound state as a function of time for different electric field amplitudes and for the fixed internuclear distance $R = 2$ a.u..

The drastic decrease of the $1s\sigma_g$ state's population, next to the rapid increase of the higher energy states' population, suggests very fast electron dynamics and excitation processes. Moreover, as it can be observed, the second (main) field maximum empties almost totally the bound state: see the OPs near the time moment 18 a.u., where the population of each state is lower than $10^{-4}$. On the other hand, when $E_0$ is low and $\gamma \gg 1$, only few electrons will be emitted, mainly via single or multi-photon absorption mechanisms, which also will lead to a low contrast holographic image created by the photoelectrons. However, in our case when using the given parameters (electric field amplitudes) for the laser pulses, the value of $\gamma$ remains confined in the vicinity of 1, therefore neither the premature (ultrafast) full ionization of the target, nor the low signal of the ejected EWPs would occur.

Next to the aforementioned behaviour of the population dynamics calculated for the high intensity $E_0 = 1$ a.u. radiation field, further important observations can be made. First, it can be seen that independently from the considered field amplitude, the $2p\sigma_u$ state starts to be populated much earlier than the lower symmetry state $2s\sigma_g$ . The former starts to be observable within the $[10^{-4} : 1]$ range already after 1 atomic (time) unit the laser field was switched on, while the later appears in the logarithmic scale only around $t = 5$ a.u.. This primary and dominant $1s\sigma_g \rightarrow 2p\sigma_u$ transition can be explained by looking at the symmetry properties of the two functions: the angular momentum quantum number of the first state is $l = 0$, while in the second (excited) state $l = 1$. By taking into account the selection rules for optical transitions the change $\Delta l = 1$ of the angular momentum quantum number via the excitation process is an optically allowed transition, which can be induced by a single photon absorption (excitation). For the $1s\sigma_g \rightarrow 2p\sigma_u$ transition $\Delta l = 0$, which requires the absorption of an even number, at least two, photons. This process can be induced provided that a higher photon density is present in the radiation field, i.e., at higher electric field values. Indeed, this behaviour was shown for the rise of the OP of the $2s\sigma_g$ state, which begun to exceed exponentially the value of $10^{-4}$ when the $|\vec{E}(t)|$ started to approach its first maximum between 5 and 7 a.u.. The similar rapid increase around this time interval was observed for the $3^{rd}$ excited $3p\sigma_u$ state, which by observing the continuous decrease of the ground's population is mainly due to $1s\sigma_g \rightarrow 3p\sigma_u$ excitation. As the external electric field stops increasing, i.e., after it reached its first maximum at $t \approx 7.5$ a.u. and it starts to decrease, the population dynamics of the excited state's seem to slow down between 7.5 and 8 a.u.. This is mainly due to the fact that for a given excited state an equilibrium in the population transfer occurs, which is the result of two opposite population transfer directions. First, the OP of the excited state is increased by two distinct factors: (i) by further excitations from the lower states (mainly from the ground) which processes, however, have slowed down since the $1s\sigma_g$ "source" already was considerably emptied and because the external field strength started to decrease; (ii) by the repopulation mechanisms from the higher excited states. Second, the OP of the excited state is continuously decreased by the laser field still present with a decreasing but not zero intensity. This behaviour can be more easily observed in Figure 7.8 by looking at the linear scale of the $2p\sigma_u$ state's OP around

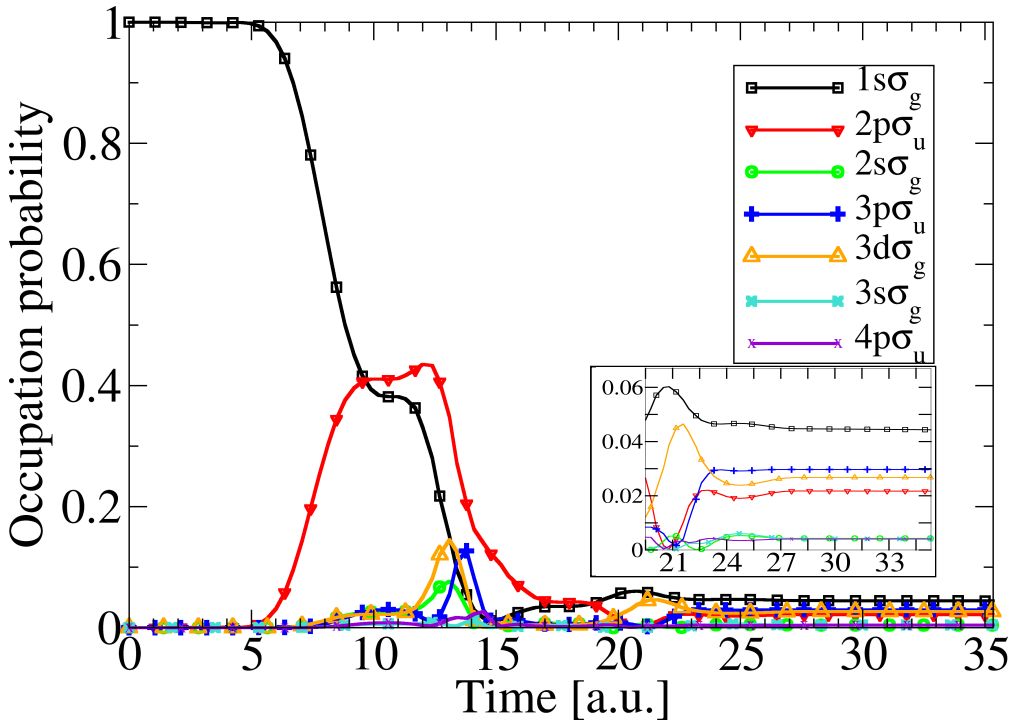


Figure 7.8: The occupation probabilities of different bound states during the interaction with the laser field having electric field amplitude of $E_0 = 0.5$ a.u.. The inlet shows the magnified region near the end ($\tau = 28.27$ a.u.) and shortly after the laser pulse ($R = 2$ a.u.).

the time moment 10 a.u. calculated for electric field amplitude $E_0 = 0.5$ a.u.. As it can be observed as the electric field strength started to decrease, the population dynamics for both the ground and the first excited state has slowed down. However, as long as the ground state still looses electrons, the OP of the first excited state remains practically constant showing a slightly increase. This increase is more obvious when the electric field changes its sign and starts to increase in the opposite direction. This will bring back the electron waves previously driven in the other $z > 0$ direction. By this process a sudden increase of the bound states OPs can be observed around $t = 13$ a.u., when the absolute value of the electric field approaches its main maximum. These ultrafast 'jumps' may be observed on both figures (OPs on logarithmic and linear scales). On the second figure around $t = 15$ a.u. the OPs of all the plotted bound states are almost zero. This occurs short time after the main peak of the laser field ($t = \tau/2 \simeq 14.13$ a.u.) was reached. The extreme depletion of the ground state, and the low OPs of the excited states indicate dominant ionization processes occurring at these high intensity values. Starting from this point the EWP dynamics already become quite complex, since many ejected electrons are already driven along different trajectories by the laser field in the continuum and also a few upper energy bound states remain slightly occupied. As the external field starts to decrease again between 16 and 18 atomic units of time, the observed OP dynamics on the logarithmic scale showed again a slowing down manner. However, since until this moment the electron was already (mainly) ionized the contribution of these excited states in the electron's wave function is very small [see the

$10^{-4} - 10^{-2}$ OP values on Figure 7.7/(b) around $t \sim 16 - 18$ a.u.]. The third larger lobe of the electric field between the time moments 18 and 23 a.u. raises again slightly the OPs which after the pulse intensity decreased again and later on when the laser pulse was switched off remained with approximately the same OP values in the $10^{-3} - 10^{-1}$ range. These values can be seen magnified in the case of the $E_0 = 0.5$ a.u. field (see inset of Figure 7.8), where it was proven that once the laser field was switched off at $\tau = 28.27$ a.u. the OPs of the bound states situated between 0 and $6 \times 10^{-2}$ stayed constant (i.e., without the laser field there is no coupling between the different states).

These small contributions of the OPs are seemingly negligible from the total electronic wave function, which after the conclusion of the laser field dominantly populates the continuum states. Although, since for the description of the continuum states the approximate Coulomb functions will be used, which are not orthogonal to the bound states of the $H_2^+$ molecule, these small contributions should be eliminated from the total electronic wave function. In that cases when these removals are neglected or not a sufficient number of bound states are subtracted from the wave function the presence of the remnant bound states will bring unphysical features into the image of the photoelectron spectrum, as it will be seen in the following section.

## 7.4 Holographic Mapping of the $H_2^+$ target

A considerable number of previous studies were done to investigate how the laser induced Holographic Mapping of atomic targets is influenced by the parameters of the radiation fields [43]. It was shown for noble gas atoms [45], that the features in the photoelectron's holographic image can be influenced by the laser field's parameters. It was demonstrated that the density of the minima and maxima in the holographic image is mainly determined by the $z_0$ maximum distance that the rescattering electron reaches (measured from the parent ion) prior to the rescattering event. It was found that for larger $z_0$ distances the density of the interference pattern was higher, and that the $z_0$ could be controlled directly with the driving field. By increasing the intensity or wavelength of the laser radiation $z_0$ was also increased, hence the HM pattern density as well.

Beside this laser field dependence, another and more interesting finding was made, which states that the features of the holographic image are also strongly influenced by the shape of the Coulomb potential of the target, i.e., the profile of the local potential the scattering electron meets along the returning path.

In order to bring novel information into this field of science the principle goal of this work was to investigate how the molecular binding potential affects the image of the photoelectron spectrum. For this purpose the simplest two center molecule ($H_2^+$) was used, for which in order to modify the Coulomb potential of the target different $R$ internuclear separations were considered: $R \in \{1, 2, 4\}$ atomic units.

Table 7.3: The Keldysh parameter for the radiation field described by $\omega_{\text{xuv}} = 0.4445$ a.u. and $E_0 = 0.5$ a.u. for different $R$ internuclear separations.

| $R$ (a.u.) | Keldysh parameter $\gamma = \sqrt{I_p/2Up}$ |
|---|---|
| 1.0 | 1.5148 |
| 2.0 | 1.3207 |
| 4.0 | 1.1217 |

For all considered internuclear separations the electric field amplitude of the used XUV laser pulse ($\omega_{\text{xuv}} = 0.4445$ a.u.) was set to the value of $E_0 = 0.5$ a.u. ($2.57\times10^9$ V/cm), which corresponds to $I = 8.7 \times 10^{15}$ W/cm$^2$ intensity. For this case the values of the calculated Keldysh gamma parameter are listed in the Table 7.3, which indicates that we are in the transition region between the multiphoton and tunneling ionization.

Moreover, by looking at the sum of the Coulomb potential and the interaction energy with the laser field, a sizable distortion of the Coulombic field (Fig. 7.9) can be observed at the instant when the radiation field is at its peak value (at $t = \tau/2$). In this given moment a potential barrier with a larger width is created.

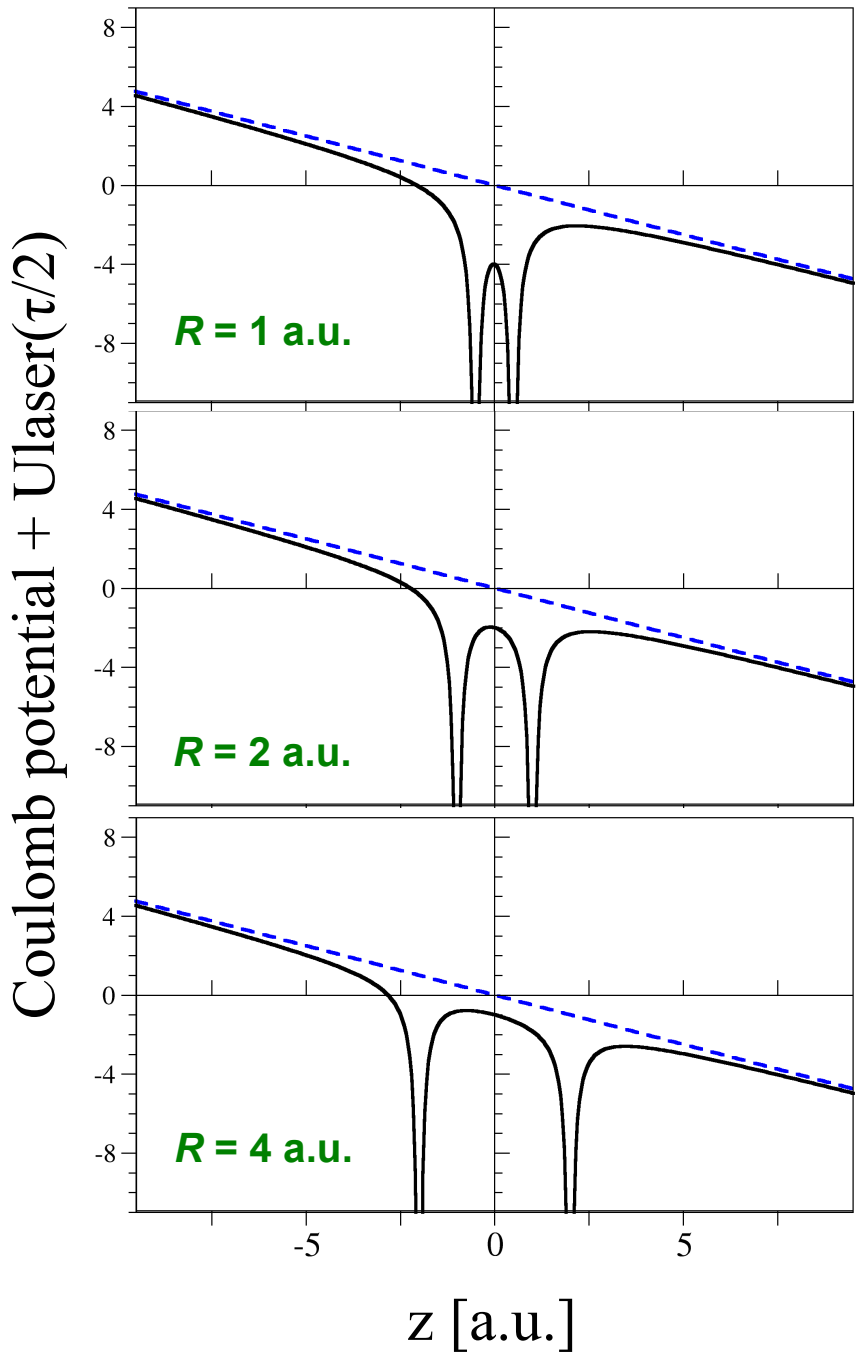


Figure 7.9: The 1D profile along the $0z$ direction of the modified Coulomb potential calculated as the sum of the Coulomb potential and the interaction potential with the laser field at the instant when the electric field is at its peak maximum value: $E(\tau/2) = E_0 = 0.5$ a.u.. The blue dashed line illustrates the force $F\left(z; \frac{\tau}{2}\right) = -zE\left(\frac{\tau}{2}\right) = -zE_0$ exerted from the laser field.

In the following the results obtained for the photoelectron spectra will be discussed, preceded by a detailed study on how the convergent spectra are obtained by removing the bound state contributions from the TDWF, and by further propagating in time ($t > \tau$) the wave function until this will reach those departed regions from the target, where the convergent data calculated by the projections onto the approximate continuum states can be considered exact.

### 7.4.1 Calculating convergent photoelectron holograms

First by fixing the laser field's parameter to $\omega = 0.4445$ a.u., $\tau = 28.26$ a.u. $E_0 = 0.5$ a.u. the photoelectron spectra for the $R$=1, 2, and 4 a.u. internuclear distances are calculated according to Eq. (6.63) and compared. Since the scattering states used during the calculation of the PESs were approximate ones, they introduced a certain amount of error into the spectra, which errors could be eliminated by subtracting the contribution of the bound states from the TDWF and by further propagating in time the wave function after the conclusion of the laser field.

In order to show these errors can be reduced to minimal, first, it was investigated how the number of subtracted bound states affects the photoelectron spectra, and second, how the image of these spectra depends on the propagation time after the end of the of the radiation field. The convergence tests for all considered internuclear separations were performed, and a similar convergence behavior of the PESs was found for all $R$ values. Here, the results obtained for the $R = 4$ a.u. case will be presented in more details.

#### PES convergence as a function of bound state subtraction

Since the two types of investigation, namely how the bound state subtraction and the propagation time influences the obtained photoelectron spectra, were performed in parallel, and it was found that close to convergent results were obtained for each considered internuclear distance at time moment $t = 5\tau$ (measured from the beginning of the laser field). The results calculated at this instance of time for the $R = 4$ a.u. proton-proton distance are presented here. In Figure 7.10 the PESs obtained for different number of subtracted bound states ($N_{BS}$) are shown.

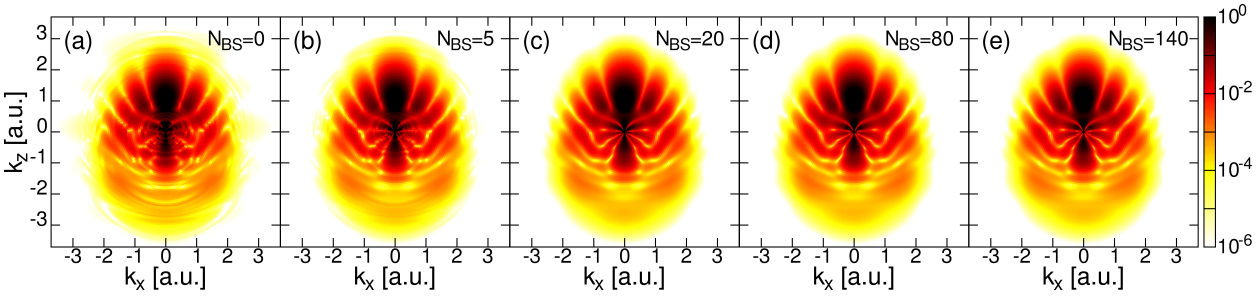


Figure 7.10: Photoelectron spectra as a function of electron momentum component parallel ($k_z$) and perpendicular ($k_x$) to the laser polarization vector, calculated as a function of subtracted bound state number ($N_{BS}$) considered at time moment $5\tau$ for the internuclear separation $R = 4$ a.u.. (a) $N_{BS} = 0$; (b) $N_{BS} = 5$; (c) $N_{BS} = 20$; (d) $N_{BS} = 80$; (e) $N_{BS} = 140$.

As one can observe in Figure 7.10 for low number of subtracted bound states in the image of the PESs some unphysical concentric rings appear, which are gradually reduced by the elimination of a higher number of BSs. The other features of the spectra are not modified by increasing the number of removed states. This demonstrates that, these rings are the direct consequence of the presence of the BSs of the $H_2^+$ in the final TDWF, and they appear

since they are not orthogonal to the used approximate scattering states. Mathematically the projection of the TDWF onto these continuum states can be given as:

$$\langle\psi_{\vec{k}}|\Psi\rangle = \sum_{i=1}^{\infty}\alpha_i\langle\psi_{\vec{k}}|\varphi_i\rangle + \langle\psi_{\vec{k}}|\Psi_{\text{free}}\rangle, \tag{7.9}$$

where the $|\Psi\rangle = \sum_{i=1}^{\infty}\alpha_i|\varphi_i\rangle + |\Psi_{\text{free}}\rangle$ wave function was partitioned into a bound and a free part with $\langle\varphi_i|\Psi_{\text{free}}\rangle = 0$ and $\alpha_i = \langle\varphi_i|\Psi\rangle \neq 0$; in the present case $\langle\psi_{\vec{k}}|\varphi_i\rangle \neq 0$. If the exact - computationally challenging to obtain - scattering states of the $H_2^+$ have been considered instead of the approximate ones, than $\langle\psi_{\vec{k}}|\varphi_i\rangle = 0$, and $\langle\psi_{\vec{k}}|\Psi\rangle \equiv \langle\psi_{\vec{k}}|\Psi_{\text{free}}\rangle$. Since in the present approach this is not the case, the bound states have to be removed from the TDWF by employing the Gram-Schmidt orthogonalization procedure where from the wave function the relevant number of $N_{BS}$ bound states were removed according to

$$|\tilde{\Psi}_{\text{free}}\rangle = |\Psi\rangle - \sum_{i=1}^{N_{BS}}\frac{\langle\varphi_i|\Psi\rangle}{\langle\varphi_i|\varphi_i\rangle}|\varphi_i\rangle, \tag{7.10}$$

where for $N_{BS}\to\infty$: $|\tilde{\Psi}_{\text{free}}\rangle = |\Psi_{\text{free}}\rangle$. By doing so, and taking into account the orthonormal property of the bound states $\langle\varphi_i|\varphi_i\rangle = \delta_{ij}$, the projection of the $|\tilde{\Psi}_{\text{free}}\rangle$ wave function onto the continuum states reads as

$$\begin{aligned}
\langle\psi_{\vec{k}}|\tilde{\Psi}_{\text{free}}\rangle &= \sum_{i=1}^{\infty}\alpha_i\langle\psi_{\vec{k}}|\varphi_i\rangle + \langle\psi_{\vec{k}}|\Psi_{\text{free}}\rangle - \sum_{i=1}^{N_{BS}}\langle\varphi_i|\Psi\rangle\langle\psi_{\vec{k}}|\varphi_i\rangle = \\
&= \sum_{i=1}^{\infty}\alpha_i\langle\psi_{\vec{k}}|\varphi_i\rangle + \langle\psi_{\vec{k}}|\Psi_{\text{free}}\rangle - \sum_{i=1}^{N_{BS}}(\langle\varphi_i|\Psi_{\text{free}}\rangle + \alpha_i)\langle\psi_{\vec{k}}|\varphi_i\rangle \simeq \\
&\simeq \langle\psi_{\vec{k}}|\Psi_{\text{free}}\rangle - \sum_{i=1}^{N_{BS}}\langle\varphi_i|\Psi_{\text{free}}\rangle\langle\psi_{\vec{k}}|\varphi_i\rangle = \langle\psi_{\vec{k}}|\Psi_{\text{free}}\rangle
\end{aligned} \tag{7.11}$$

As described in Eq. (7.9) the projection of the bound part of the TDWF onto single center Coulomb wave functions is non-vanishing, and during the calculation of the PES it is coherently added to the projection of the continuum part of the time-dependent wave function leading to the concentric ring structure appeared in Figure 7.10(a). However, it was proven that with gradual subtraction of the BSs from the TDWF the concentric rings start to fade away: i.e., for $N_{BS} = 5$ they are already significantly reduced [see Figure 7.10(b)], while for $N_{BS} \geq 20$ they are barely visible.

This behavior is also observable on Figure 7.11 where the PES is presented as a function of electron ejection angle $\theta_k$ (measured from the polarization vector of the laser field) for a fixed electron momentum $k = 0.5$ a.u.. We see a significant change in the photoelectron spectra as we increase $N_{BS}$ from 0 to 5, and then to 20, while for $N_{BS} \geq 20$ the changes in the PES are negligible. After analyzing the spectrum at different fixed electron momentum values, by scanning both the lower and higher momentum part of the PES, it was found that

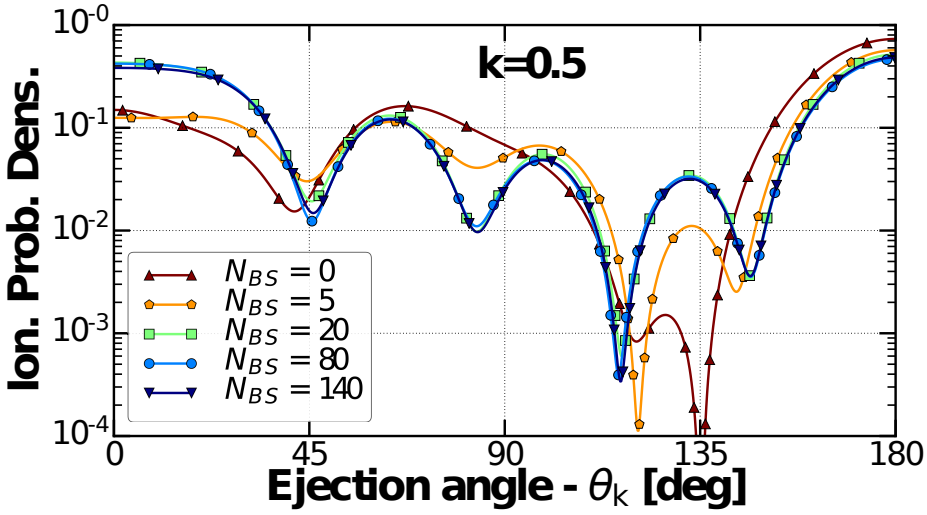


Figure 7.11: Ionization probability density at $t = 5\tau$ for the fixed $k$ =0.5 a.u. momentum as a function of the number of subtracted bound states for the internuclear distance $R$=4 a.u..

the significant differences between the results obtained for $N_{BS} \geq 20$ disappear.

Similar investigations regarding the convergence of the PESs were done for the other internuclear distances as well ($R = 1$ a.u., and $R = 2$ a.u.), where a very similar behavior was observed. However, as it was expected, it was found that with the decrease of $R$ the number of subtracted states required for a converged photoelectron spectra increased. This can be explained simply by the fact, that for smaller $R$ internuclear separation values, the ionization potential is higher (recall Table 7.2), which results that after the conclusion of the laser field a larger portion of the TDWF will be distributed among the various bound states. Therefore, in order to eliminate as much as possible the undesired errors brought into the image of the photoelectron spectra by the presence of these bound states, the PESs presented in the following part of this work were calculated after a total number of $N_{BS} = 120$ bound states had been removed from the wave function.

**PES convergence as a function of propagation time**

In Figure 7.12 the photoelectron spectra calculated for $R = 4$ a.u. at different time moments ($t = \tau$, $3\tau$, and $5\tau$; with $\tau$ being the duration of the laser pulse) is shown. A noticeable change in the PES as a function of the propagation time can be observed for small photoelectron momentum values ($k \leq 1$ a.u.).

In contrast, for the high electron momentum part of the PES by increasing the propagation time the changes in the spectra are barely observable. This difference between the behavior of the two distinct parts of the spectrum can be understood based on the following arguments. The difference between the one-center Coulomb wave functions and the exact continuum (scattering) states of the $H_2^+$ molecule is the largest in the immediate vicinity of the target. Hence, the difference between the spectra calculated by using exact and approximate states for describing the continuum electron will be the most pronounced when an important part of the wave function is still in the area close to the nuclei. In other words,

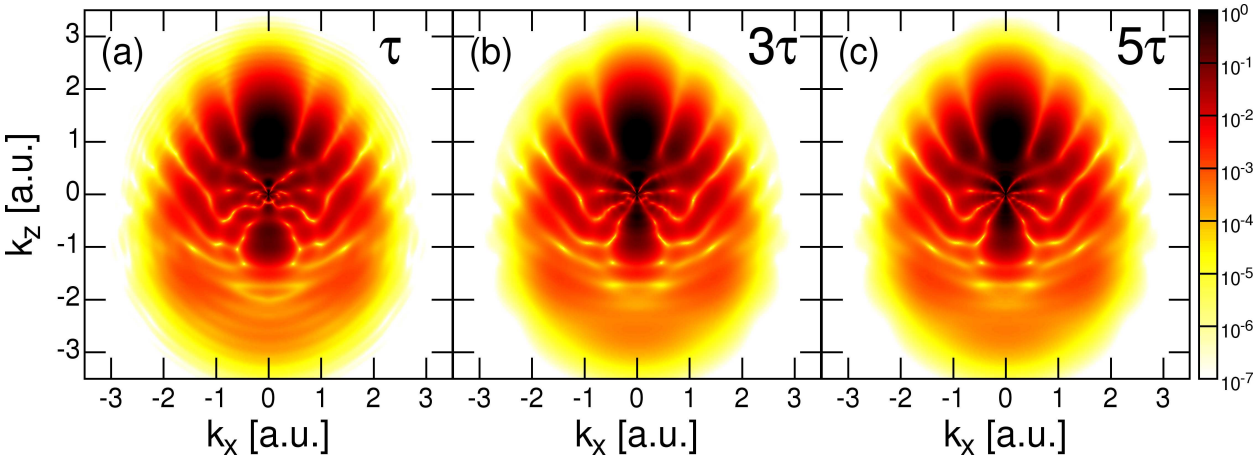


Figure 7.12: Ionization probability density calculated for the internuclear distance $R = 4$ a.u. as a function of electron momentum component perpendicular ($k_x$) and parallel ($k_z$) to the laser polarization vector calculated at time moments: (a) $\tau$; (b) $3\tau$; (c) $5\tau$.

the projection error introduced by the the approximate continuum states is larger when the freed electron wave packet is closer to the target.

These projection errors appearing in the low momentum part of the spectra can be reduced or totally eliminated by further propagating in time the continuum EWP after the laser field was switched off. This goal can be achieved, since by increasing the propagation time the freed electron wave packet will depart from the vicinity of the nuclei to those regions of the coordinate space where the difference between the approximate and exact scattering states is smaller and becomes negligible from the point of view of the PES calculations. Another important remark, is that the low momentum part of the ejected EPWs will depart much slower from the target, so as it can be observed on Fig. 7.12(a)-(b), where by propagating from the time moment $t = \tau$ to $t = 3\tau$, the low momentum part of the spectra (compared to the high momentum part) is more severely affected by the discussed projection error.

These previously outlined arguments are also supported by the fact, that by increasing the propagation time, the differences in the PESs visibly get more and more reduced. While the changes between the PESs calculated at time moments $t = 1\tau$ and $t = 3\tau$ are clearly identifiable, the difference between the $t = 3\tau$ and $t = 5\tau$ PESs gradually faded away, and become less recognizable. In order to check how far the continuum wave packets were departed after the completion of the laser field, we plotted on Figure 7.13 the value of the electron's expected distance $\langle r \rangle$, which practically measures the mean distance of the EWPs from the center of mass of the system, i.e. from the origin. By comparing the expected value of the electron's distance to the values of the internuclear separations it can be seen that even at the completion of the laser field, at time moment $\tau$, the measured distances are near the value of 20 a.u. (10 times the equilibrium internuclear distance), while at time moment $5\tau$ in each internuclear case this exceeds 120 a.u.. This observation suggests that the major part of the EWPs are departed sufficiently far from the nuclei at these larger

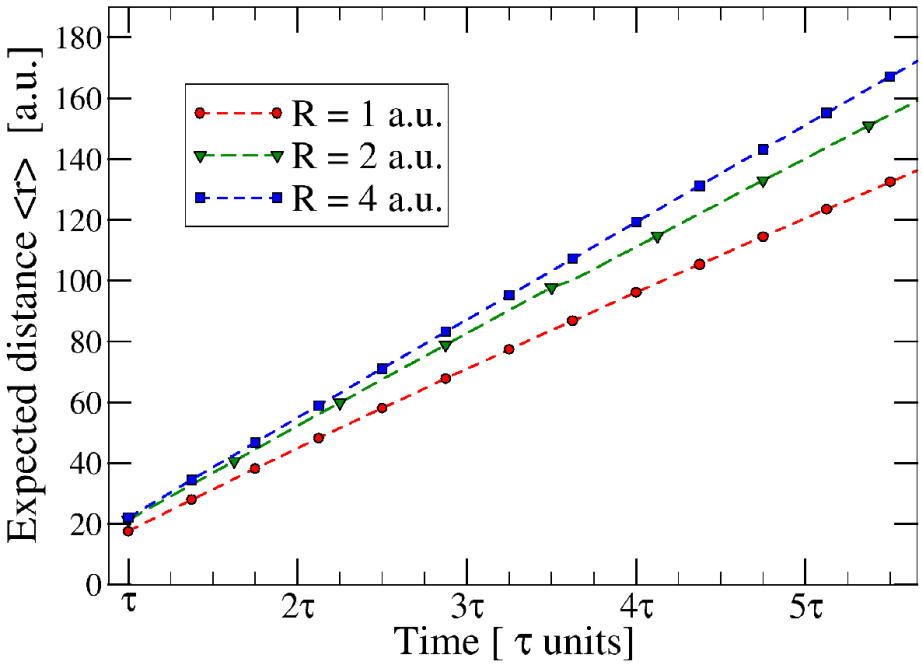


Figure 7.13: The expected position of the continuum ('free') wave function as a function of propagation time after the completion of the laser pulse.

time moment and presumably the use of the approximate scattering states are delivering us reliable results.

More rigorous investigations may be done by taking cuts of the PESs along different fixed $k = |\vec{k}|$ momentum values from different parts of the momentum region. In Figure 7.14 the photoelectron angular distribution as a function of propagation time is shown for a smaller $k = 0.2$ a.u. and for two larger momenta values $k = 0.5$ a.u. and $k = 1$ a.u.. With the increase of $k$ a faster convergence was obtained, which is supported by the aforementioned considerations, according to which the electrons having larger momentum values (i.e., higher velocities) are departed further away from the nuclei - than those with smaller momenta - in regions where the results obtained with the approximate scattering states would approach more and more the exact results. Although, as one can observe in Figure 7.14(a) - where the results for the slowest convergence were obtained - the PESs calculated starting from time moment $t = 4\tau$ up to $5\tau$, $t = 6\tau$ slightly differ from each other.

The distinct behavior of the electronic wave packets with different momentum values can be further highlighted by plotting the PES along a given $\theta_k$ electron ejection angle. This was done for a fixed $\theta_k = 40°$ ejection angle in Figure 7.15 (i.e., the approximate direction of the first maximum in Fig. 7.12), where the convergence as a function of propagation time is shown. As one can clearly see, the larger momentum part ($k > 1$ a.u.) of the spectra converged much faster (already at $t = 2\tau$) than the lower part. For small electron momentum values the convergence is not 'fully' achieved even for $t = 6\tau$ propagation time value (see the inset of Fig. 7.15).

In order to deliver reliable results for the photoelectron spectra two distinct possibilities

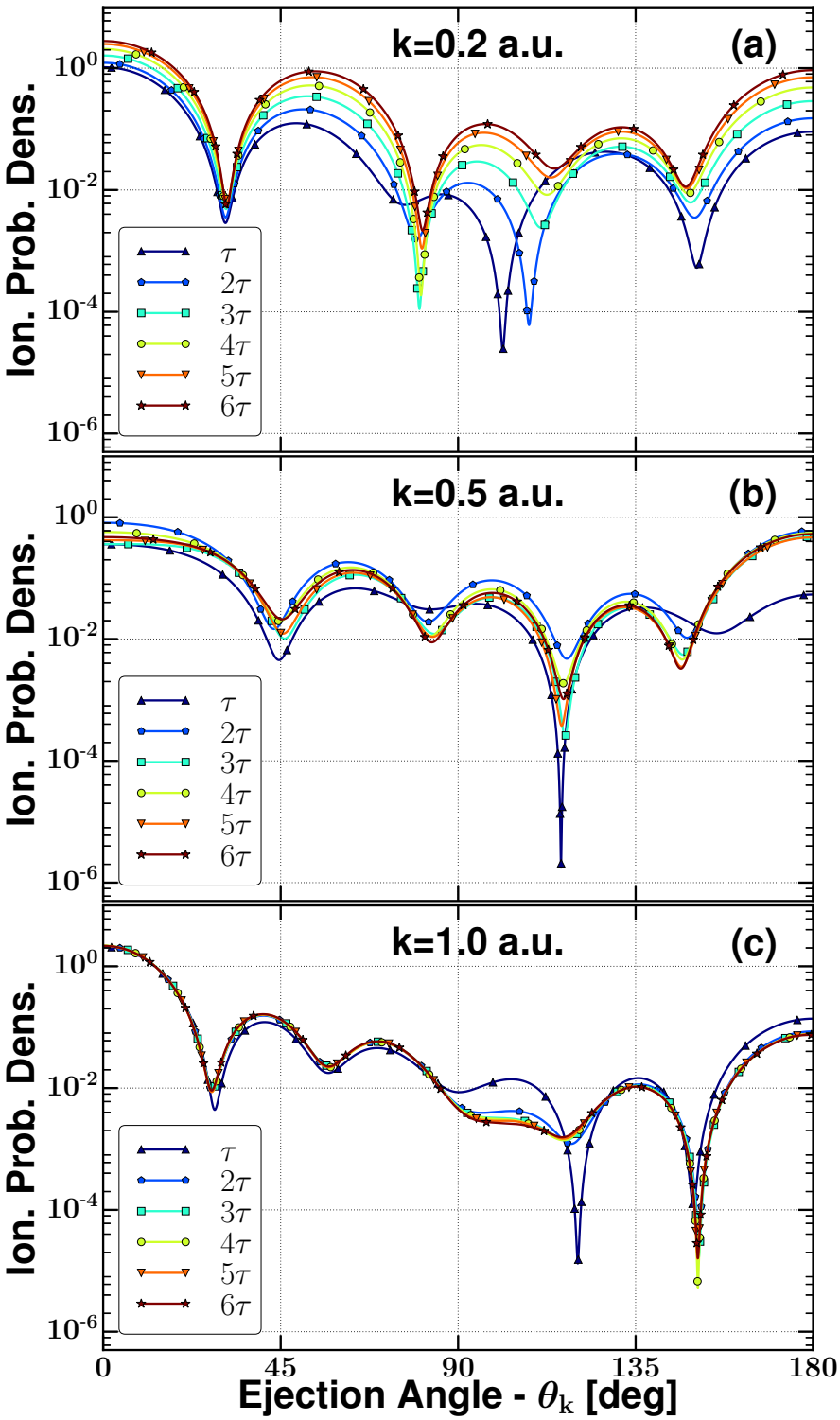


Figure 7.14: The angular distribution of photoelectrons as a function of the propagation time. Results are shown for $R = 4$ a.u. and for different electron momentum values: $k$=0.2 a.u. (a); $k$=0.5 a.u. (b); $k$=1 a.u. (c).

remain. The first one relies in propagating even further in time the time-dependent wave function until a 'full' and also visibly observable convergence in the scale of the *oy* axis of Fig. 7.15 is obtained for the smaller $k$ values as well. However, not even the results obtained with this approach will ever give a perfect match between the data points calculated at a two

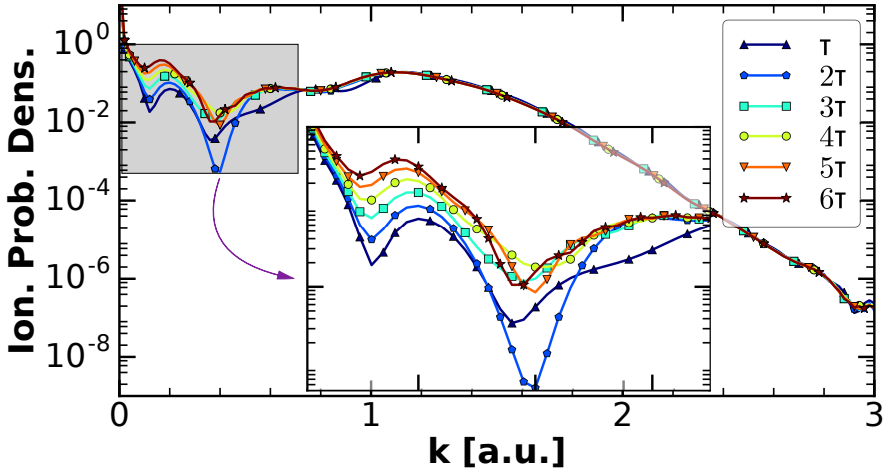


Figure 7.15: Segments of the photoelectron spectra for R=4 at different time moments and for the fixed electron ejection angle $\theta_k = 40°$ in the range of $k \in [0, 3]$ is shown, while in the inset we show a zoom into the range of $k \in [0, 1]$.

later time moments $t' = n \cdot \tau$ and $t'' = (n+1) \cdot \tau$ (where $n \in \mathbb{Z}^+$ being a large positive integer number), since a small difference always will be present between the calculated curves (just as it can be shown to be present also for the larger $k > 1$ momentum values after one zooms more into the image of the curves of Fig. 7.15). Another drawback of this approach consists in a numerical issue, that is, by propagating the TDWF even further in time those EWPs which have the highest momenta at a certain time will reach first the edge of the simulation box. At edge of the simulation grid (i.e., $\xi_{\max}$) these high momenta EWPs are absorbed by the complex absorbing potential provided that the absorbing coefficient was set to a sufficiently high value. If the absorbing coefficient was not chosen correctly reflections from the boundaries may occur. Both the absorptions and reflections from the boundaries will distort the higher momentum part of the PESs. In order to avoid these undesired numerical artifacts, which would appear in the calculated photoelectron spectra, the coordinate space simulation box should also be increased (i.e., to prevent absorptions and reflections at the boundary). This translates to a non-negligible increase of the CPU time required for the simulations.

The other, and implicitly a much more reasonable approach would be to introduce a small valued error tolerance parameter that would characterize the quality of the PES convergence, and to give the final results within a fixed accepted error tolerance value. By doing so, the simulation box from the start of the time propagation (at $t = 0$ a.u.) should have been set to a sufficiently large value, which guarantees that the PES convergence parameter will be achieved before the accumulated WF absorptions at the boundaries does not exceed an initially (arbitrarily) fixed value of $10^{-8}$. Since, the second approach seemed to be much more numerically achievable and reasonable, it was favored instead of the first procedure, and it was used to characterize quantitatively the convergence of the photoelectron spectra.

**Convergence parameter assigned to the calculated photoelectron spectra**

In order to quantitatively describe the convergence of the PES, the parameter

$$\mathcal{E}(t) = \frac{\int\int \mathrm{d}k_x \mathrm{d}k_z |P(k_x, k_z; t) - P(k_x, k_z; \tau)|}{\int\int \mathrm{d}k_x \mathrm{d}k_z P(k_x, k_z; \tau)}, \quad \text{for } t > \tau. \tag{7.12}$$

was introduced, which measures the relative difference between the spectrum calculated at the end of the laser pulse (in time moment $\tau$) and the PES calculated at a later time moment $t > \tau$. As it was assumed and expected, it was observed that $\mathcal{E}(t)$ exponentially converges towards an asymptotic value $\mathcal{E}_\infty$. This value can be obtained by fitting the calculated $\mathcal{E}(t)$ data points with a function having the analytical expression of

$$\mathcal{E}_{\mathrm{fit}}(t) = \mathcal{E}_\infty - \beta e^{-\alpha t}, \quad \alpha, \beta \in \mathbb{R}^+, \tag{7.13}$$

where the positive real numbers $\alpha$ and $\beta$, next to the value of $\mathcal{E}_\infty$ need to be obtained. The fitting procedure was carried out for each internuclear separation considered in the present section, and the $\mathcal{E}_\infty^R$ parameter determined for each case. The estimated relative error of the PES, i.e., the convergence parameter, was defined as

$$\delta_{\mathrm{conv}}^R(t) = \mathcal{E}_\infty^R - \mathcal{E}^R(t). \tag{7.14}$$

In Figure 7.16 this estimated relative error parameter is plotted as a function of time along with its exponential fit ($\beta e^{-\alpha t}$) for the considered proton-proton distances. An excellent agreement was found for each internuclear separation between the $\delta_{\mathrm{conv}}^R$ curves and the used exponential fitting functions, which confirms the assumed exponential decrease behavior of the projection error as a function of time. Figure 7.16 indicates an error estimate below the value of 0.5% for each internuclear separation at the propagation time moment $5\tau$.

Since this small remaining error affects mostly the lower momentum part of the photoelectron spectra (as it was seen in Fig. 7.15) and by taking into account that the dominant features of the photoelectron hologram are situated at the higher momentum regions of the PES, the value of 0.5% for the convergence parameter was accepted and time propagation ended at $t = 5\tau$. The further results were obtained by using the TDWF in time moment $t = 5\tau$ from which a total number of $\mathrm{N_{BS}} = 120$ bound states were eliminated.

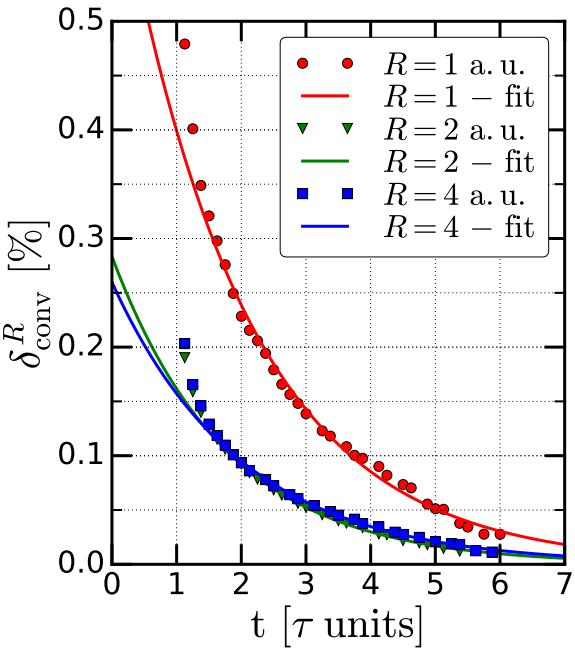


Figure 7.16: The error estimating convergence parameter $\delta^R_{\rm conv}$ [Eq. (7.14)] as a function of time for different internuclear distances. The calculated data points are shown along with the $\beta e^{-\alpha t}$ fits.

### 7.4.2 The effect of the molecular potential on the photoelectron hologram

As it was already mentioned, the present work aims to investigate the structure of the photoelectron hologram for laser irradiated molecular targets, more precisely, how the geometry and internal structure of the molecule affects the holographic image. In order to achieve this goal, the results obtained for different ($R = 1, 2, 4$ a.u.) internuclear separations of the $H_2^+$ molecule interacting with the two-cycle laser pulse (frequency: $\omega = 0.4445$ a.u.; pulse duration: $\tau = 28.26$ a.u.; electric field amplitude: $E_0 = 0.5$ a.u.) is presented.

From previous studies [43, 45, 52, 53] we know that the features appearing in the photoelectron holograms are predominantly affected by two factors. The first one is the spatial path of the signal, or strongly scattered electron, which can be characterized by the $z_0$ parameter meaning the maximum distance that the ejected EWP reached before the rescattering event. It was also shown that the value of $z_0$ highly depends on the laser field parameters, giving the possibility to control this with coherent radiation. The second important factor, which leaves its imprint on the hologram, is the value of the potential in the target's close vicinity that the rescattering electron experiences during its returning time along the signal trajectory (i.e., along its returning path) [45].

In order to identify the influence of the molecular binding potential on the PES, also calculations for a model system as XUV target were carried out. This model system was described by a spherically symmetric potential, which in contrast with the $H_2^+$ molecule had no singularities at the positions of the cores, but its asymptotic form was identical to the Coulomb potential of the molecule. Moreover, by ensuring the ionization energy of the model potential to be equal to the ionization potential of the $H_2^+$ target, when these systems interact with the same XUV few cycle laser field a similar signal electron trajectories will be produced (i.e., the $z_0$ parameter will be the same). If these aforementioned conditions are met, the difference appearing in the photoelectron spectra can be directly attributed to the difference between the two binding potentials in the immediate vicinity of the target systems [45].

The model potential is constructed by performing the molecular axis orientation averaging of the potential created by the two nuclei of the $H_2^+$ molecule, which leads to the following expression

$$V_{\text{mod}}(r) = \begin{cases} -2/r & , \text{ if } \quad r \geq R/2; \\ -4/R & , \text{ if } \quad r < R/2, \end{cases} \tag{7.15}$$

with $R$ being the internuclear separation of the $H_2^+$.

Compared to $H_2^+$ the ionization energy of the model target is lower, since the deep potential well around the two nuclei disappears as a result of the orientation averaging. Therefore, in order to ensure the same ionization energy the model system's potential should be modified by considering the following substitution $R \to R_{\text{equiv}}$, where $R_{\text{equiv}}$ was introduced as the model's parameter. The value of $R_{\text{equiv}}$ for each corresponding internuclear separation

of $H_2^+$ is listed in Table 7.4.

Table 7.4: The values of the equivalent internuclear distances used for the model target system.

| $R$ [a.u.] | $R_{\text{equiv}}$ [a.u.] |
|---|---|
| 1.0 | 0.92 |
| 2.0 | 1.72 |
| 4.0 | 3.01 |

Figure 7.17 illustrates the two considered potentials for $R = 2$ a.u., $R_{\text{equiv}} = 1.72$ a.u. plotted next to each other along the $0x$ and $0y$ Cartesian coordinate axis, while in the next figure, in Fig. 7.18, their scaled differences for all considered internuclear cases are shown in the $\rho 0z$ plane, i.e., in the cylindrical coordinate system where $\rho = \sqrt{x^2 + y^2}$.

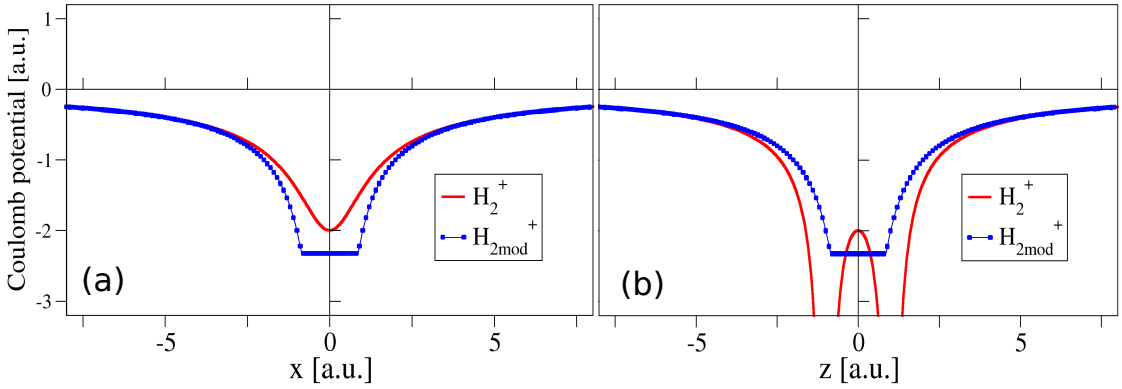


Figure 7.17: The Coulomb potential of the $H_2^+$ molecule and of the $H_{2\text{mod}}^+$ model target along the $0x$ (a) and $0z$ (b) axis is shown for $R(H_2^+) = 2$ a.u. and $R_{\text{equiv}}(H_{2\text{mod}}^+) = 1.72$ a.u. parameters.

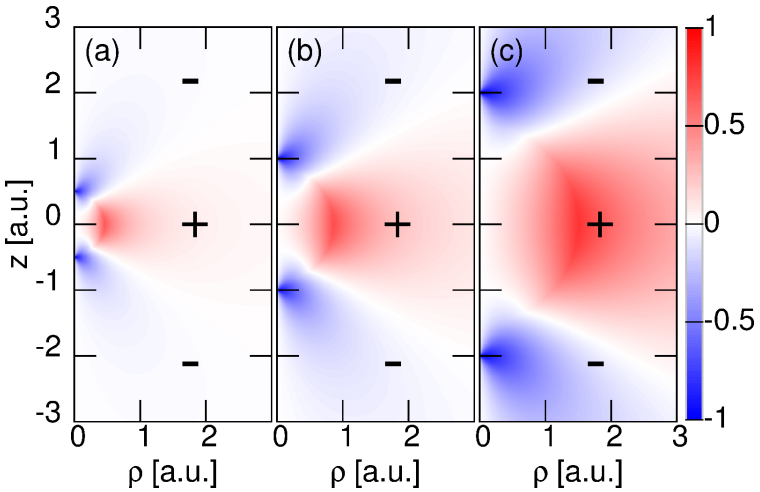


Figure 7.18: The value of $\rho\,[V(\rho, z) - V_{\text{mod}}(\rho, z)]$, where $\rho$ and $z$ are the cylindrical coordinates, calculated for the corresponding pairs: (a) $R(H_2^+) = 1$ a.u., $R_{\text{equiv}}(H_{2\text{mod}}^+) = 0.92$ a.u.; (b) $R(H_2^+) = 2$ a.u., $R_{\text{equiv}}(H_{2\text{mod}}^+) = 1.72$ a.u.; (c) $R(H_2^+) = 4$ a.u., $R_{\text{equiv}}(H_{2\text{mod}}^+) = 3.01$ a.u..

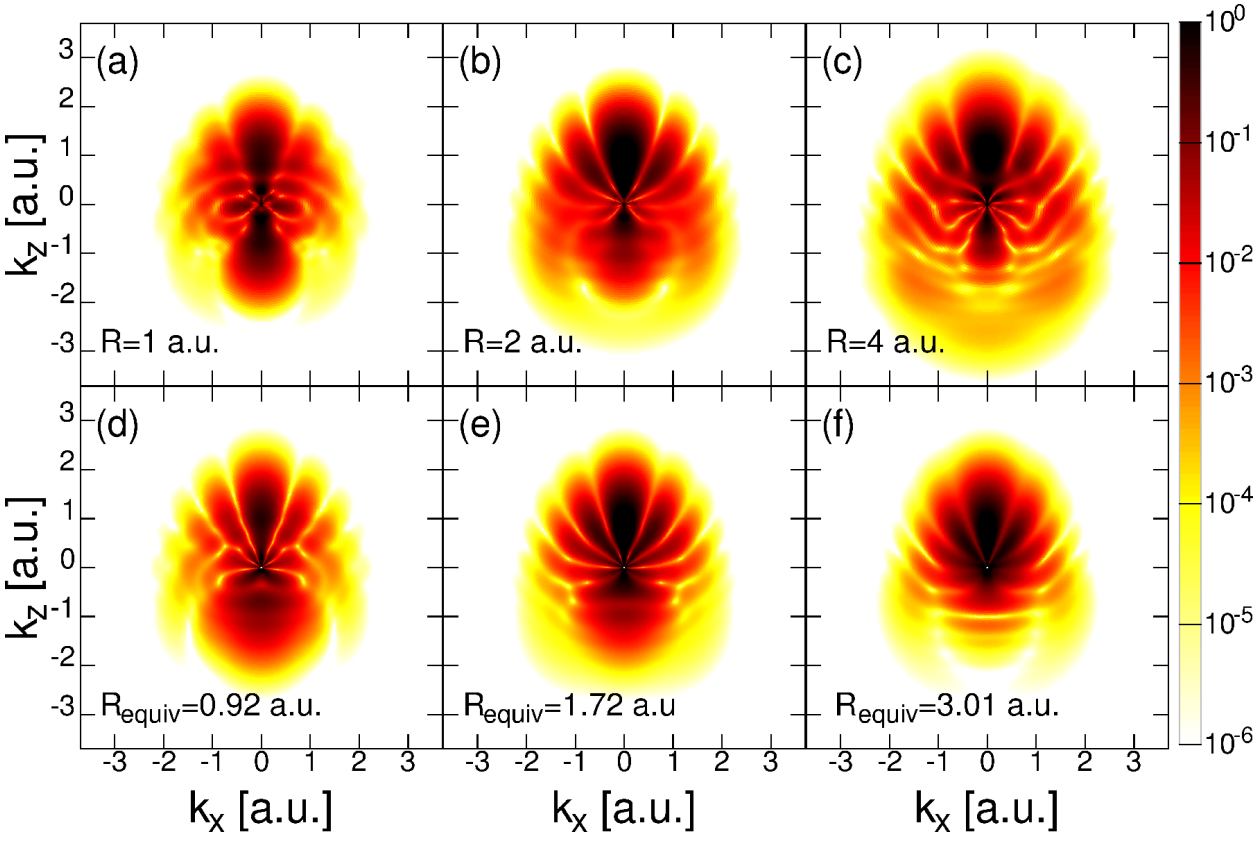


Figure 7.19: The converged photoelectron spectra calculated for the $H_2^+$ (first row) are shown for different internuclear distances: (a) $R = 1$ a.u., (b) $R = 2$ a.u., (c) $R = 4$ a.u.. The $H_{2\text{mod}}^+$ results corresponding to each internuclear separation are shown below the $H_2^+$. For a given $R$ the ionization energy of the $H_2^+$ and $H_{2\text{mod}}^+$ targets is the same: $I_p^{(a)} = I_p^{(d)}$; $I_p^{(b)} = I_p^{(e)}$; $I_p^{(c)} \equiv I_p^{(f)}$.

The converged PESs calculated for the $H_2^+$ and its model target are shown in Figure 7.19. In the first row of the figure the results obtained for the molecule, while in the second one the data calculated for the model system are plotted. At first sight, similarities between the photoelectron spectra calculated for the corresponding $R$ - $R_{\text{equiv}}$ pairs [Fig. 7.19(a)-(d), Fig. 7.19(b)-(e), Fig. 7.19(c)-(f)] can be observed. These similarities between the holograms can be mainly attributed to the fact that the model system was constructed in such a way that its ionization potentials was the same with the $I_p$ of the molecule. Hence, under the action of the same laser pulse the interfering electronic wave packets were driven by the field roughly along the same direct and scattered paths for both targets. This ensured that the phases accumulated by the electron along these paths were similar for both systems.

By knowing this, the differences that occur between the spectra obtained for the different targets are the direct consequence of the different spatial profile of the binding potentials, mainly along the returning path of the signal electron in the vicinity of the cores. The difference between the two potentials was illustrated in Figure 7.18, where the value of $\rho\,[V(\rho, z) - V_{\text{mod}}(\rho, z)]$ is shown in the $\rho Oz$ plane.

The discrepancies between the photoelectron holograms calculated for the $H_2^+$ and the

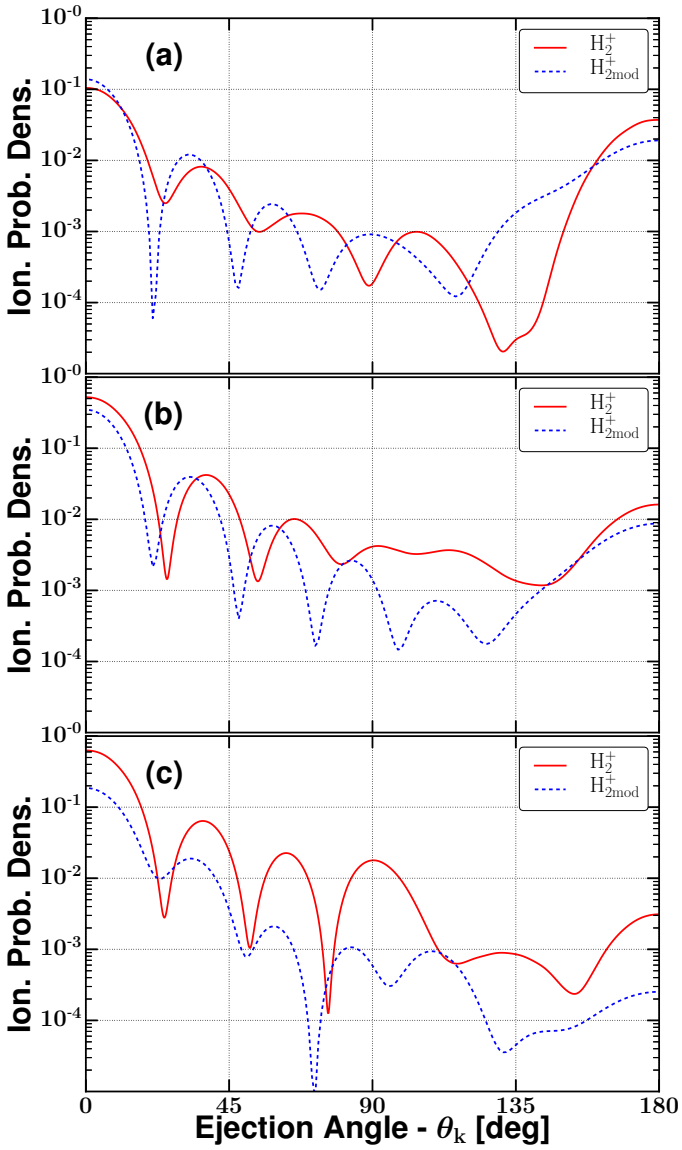


Figure 7.20: The angular distribution of photoelectrons at the fixed $k = 1.5$ a.u. momentum value for the different targets: (a) $R(H_2^+) = 1$ a.u., $R_{\text{equiv}}(H_{2\text{mod}}^+) = 0.92$ a.u.; (b) $R(H_2^+) = 2$ a.u., $R_{\text{equiv}}(H_{2\text{mod}}^+) = 1.72$ a.u.; (c) $R(H_2^+) = 4$ a.u., $R_{\text{equiv}}(H_{2\text{mod}}^+) = 3.01$ a.u..

model target can be further studied by comparing in Figure 7.20 the angular distribution of the laser ejected electrons at a given $k = 1.5$ a.u. electron momentum value for different $R$ parameters. As one can observe, for all internuclear separation values several deep minima appears in the forward electron ejection direction when $\theta_k \leq 90°$. These features associated with the spatial interference of the EWPs can be clearly identified for both type of targets. In addition to this, the location of these interference minima are more or less the same, i.e., the ejection angles at which they appear roughly coincide for both systems.

However, in the case of the $H_{2\text{mod}}^+$ target, for all internuclear separations the interference minima are systematically situated at slightly smaller electron ejection angles. This results a slightly denser (smaller average angular separation between the interference minima) hologram for the model system. The denser features appearing in the hologram of the model

target can be explained by the following reasoning. It was previously shown [45] that the trajectory of the signal electron in the vicinity of the two nuclei does not coincide exactly with the $0z'$ internuclear axis, and there is a small but $\rho \neq 0$ separation between them. Along these signal (strongly scattered) trajectories, which are nearly parallel to the $0z'$ axis and for which $\rho \sim 1$ a.u., the electron meets a deeper binding potential in the case of the model target. This was confirmed in Figure 7.18, where it can be seen, that with the notable exception of the nearest vicinity of the nuclei of the $H_2^+$ molecule for larger domains $\rho\left[V(\rho,z) - V_{\mathrm{mod}}(\rho,z)\right] \geq 0$. The deeper scattering potential along the signal trajectory produces a denser hologram [45], as it was observed on Fig. 7.20.

Based on the presented arguments, obviously the differences between the PES calculated for the real system and the model target can be directly attributed to the difference between the two-center binding potential of $H_2^+$ and the central potential of the model target.

Another interesting, feature appearing in the molecular PES would be the presence of the two-center interference [89, 90, 91] of the EWPs rescattering on the cores of the $H_2^+$ target. At first sight in the hologram of the $H_2^+$ molecule obvious traces indicating this process can not be identified. The fact that well distinguishable two-center interference patterns are not observable is not surprising, since as it was observed in the EWP dynamics the dominant continuum EWPs are 'born' during the second and third half optical cycle of the driving field [2] during a relatively large - compared to the period of the oscillating field - duration of time. These EWPs can be decomposed into smaller wave packets, which are 'born' over a very short period of time during which the vector potential of the radiation field stays practically at a constant value. The two-center interference pattern might be present in these smaller EWPs, which however after the conclusion of the laser field - when these EWPs are coherently added - the shape of this pattern will presumably fade away. This is due to the fact, that each small EWP is shifted in momentum space in accordance with the value of the laser field's vector potential in its creation moment, thus the interference pattern most probably will be averaged out.

Nonetheless, traces of the two-center interference effects in the hologram might be possible to be detected along the path in the PES that follows the curve associated with a minimum, where this effect would appear as a modulation in the depth of the holographic interference minima. In order to continue our investigations, in Figure 7.21 we plotted the PES along the holographic interference minima around the $\theta_k = \pi/8$ electron ejection angle for the $H_2^+$ and the model $H_{2\mathrm{mod}}^+$ targets.

It was found that a high momentum ($k > 1.5$ a.u.) minimum appears in the curve of the $H_2^+$ target which is totally absent in the PES calculated for the model target. This minimum is located relatively close to the two-center interference minimum predicted by simple models (Nagy et al [92]), according to which the two-center interference pattern was found to be proportional to $\cos^2\left(\vec{k}\cdot\vec{R}/2\right)$. The shift in the location of the $H_2^+$ minimum

[2] for similar laser pulse and atomic targets this behavior was also shown in [45, 43]

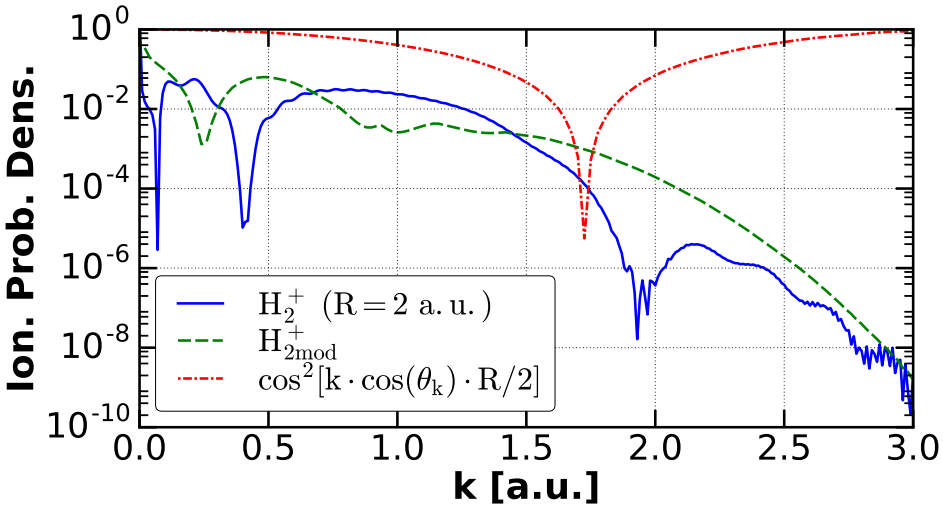


Figure 7.21: PES values along the first spatial interference minimum calculated for $H_2^+$ and for the $H_{2mod}^+$ model plotted next to $\cos^2(\vec{k} \cdot \vec{R}/2) \equiv \cos^2[k \cdot \cos(\theta_k) \cdot R/2]$ using logarithmic scale.

can be mainly attributed to the nonzero value of the vector potential at the moment of birth of the continuum EWP that produced this deep minimum. Beside this, few other deeper minima occurred in the low momentum part of the PES curves obtained for both targets. These features are the results of the interference between electron wave packets created during the second and third half optical cycle of the radiation field [45].

In order to study the internuclear separation dependence of the electron spectra calculated for the $H_2^+$ molecule, we plotted on Figure 7.22 the PESs along a fixed momentum value in the forward ejection region ($\theta_k < 90°$) for different $R$ values. The value of $k$ was chosen in such a way, that the semicircle (whose radius is given by $k$) which can be drawn around the origin of Figs. 7.19(a)-(c) bisects all major maximum lobes appearing in these holograms. This condition was fulfilled by setting $k = 2$ a.u., since in the case of lower momentum values for $R = 1$ a.u. [Fig. 7.19(a)] and $R = 4$ a.u. [Fig. 7.19(c)] the patterns appearing closer to the origin of the PES are more complex, resulted from multiple scattering of the signal EWP [45]. A first observation regarding the internuclear dependence of the hologram could be made already by looking at the forward plane ($0 < \theta_k < 90°$) on these previously presented contour-plot images, where it can be noticed that by increasing $R$ from 1 a.u. to 4 a.u. the number (density) of minimum fringes also increased. This behavior is evidenced in Figure 7.22, where the angular distribution of photoelectrons ejected with asymptotic momentum $k = 2$ a.u. are shown. According to this plot, for $R = 1$ a.u. proton-proton distance 3 spatial interference minima can be counted, which by increasing $R$ to 2 a.u. and 4 a.u. raises to the value 4. By comparing the curves for the two last separation values, it can be seen that the $4^{th}$ interference minimum for $R = 4$ a.u. is located at smaller $\theta_k$ value than the $4^{th}$ interference minimum for $R = 2$ a.u.. This implies a smaller average angular separation between the interference minima for the larger $R$ value.

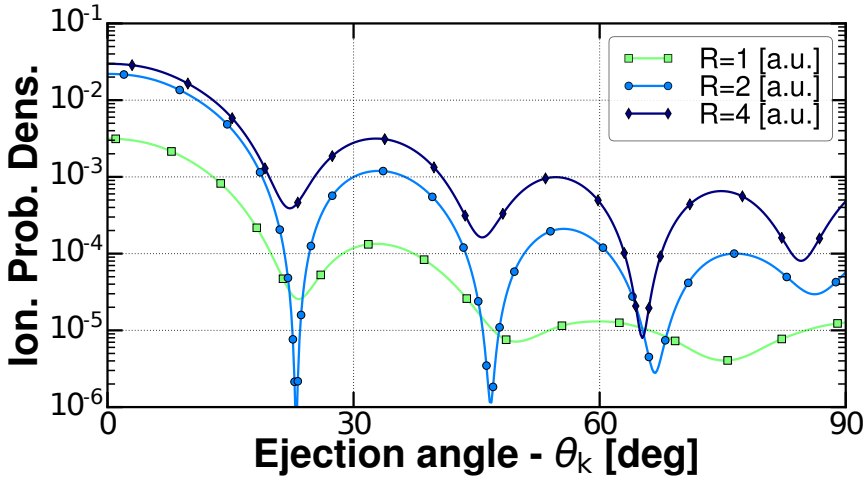


Figure 7.22: The $k = 2$ a.u. segments of the photoelectron spectra zoomed to the ejection region $\theta_k < 90°$ calculated for the $H_2^+$ molecule for the different $R$ internuclear separations.

This behavior of the PES as a function of internuclear distance can be indirectly attributed to the drop-off of the ionization energy with the increase of $R$ (recall Table 7.2). For a fixed driving pulse the drop-off of the $I_p$ will lead to the increase of the initial velocity of the ejected electrons, which in turn will cause longer signal trajectories before the rescattering event. Since the signal path is increased also $z_0$ gets larger, hence the density of the PES will be increased as well.

In spite of the considerably large change in the $I_p$ of the $H_2^+$ molecule from 1.4517 a.u. ($R = 1$) to 0.796 a.u. ($R = 4$) a drastic increase in the density of photoelectron holograms is not present. This is due to the fact, that by increasing the internuclear distance the depth of the binding potential experienced by the electron along the signal path is shallower, which in turn will lower the density of the holographic image of the molecular target.

### 7.4.3 Photoelectron spectra as a function of laser field intensity

The frequency of the laser field was fixed to $\omega = 0.4445$ a.u., while the duration of the laser pulse to $\tau = 28.26$ a.u., and by modifying the value of the electric field's amplitude ($E_0$) the ionization of the $H_2^+$ was investigated. In this part of the work the results obtained for the $R = 2$ a.u. equilibrium internuclear distance of $H_2^+$ are presented. In Figure 7.23 the obtained ionization probability densities are shown as a function of electron momentum component perpendicular ($k_x$) and parallel ($k_z$) to the laser field's polarization vector for the electric field amplitudes $E_0 \in \{0.25, 0.5, 0.75, 1\}$ a.u..

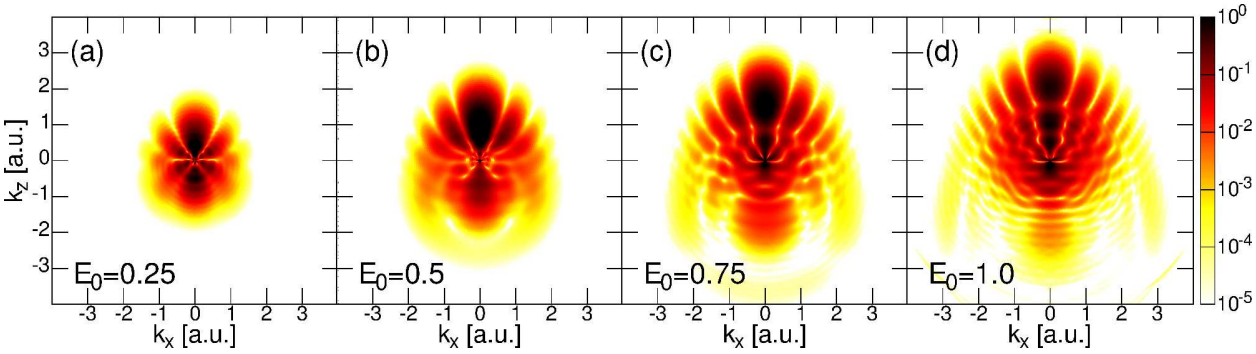


Figure 7.23: Laser induced photoelectron spectra as a function of electric field amplitude [(a) $E_0 = 0.25$ a.u., (b) $E_0 = 0.5$ a.u., (c) $E_0 = 0.75$ a.u., (d) $E_0 = 1$ a.u.] calculated for the $R = 2$ a.u. equilibrium internuclear distance after the completion of the external field ($t = \tau$). On the x-axis electron momentum component perpendicular ($k_x$), on the y-axis parallel ($k_z$) to the laser polarization vector is shown.

By looking at the plots, at first sight two straightforward observations can be made. The first one is an obvious and expected behavior, according to which with the increase of the field's intensity the ionization probability of the electrons is distributed along a larger region of the momentum space, implying that by using more intense radiation, the largest measurable electron energy is increased (i.e., higher momentum and energy electrons will appear in the spectrum). While, for the lowest $E_0 = 0.25$ a.u. field the maximum of the ionization probability densities is situated around the value of $k_z = 0.5$ a.u. (resulting a $\mathcal{E}_{\text{kin}} = (k_x + k_z)^2/2 = 0.125$ a.u. electron energy), the maximum is shifted to the high momentum value of $k_z = 2$ a.u. for the case of the extremely high intensity ($E_0 = 1$ a.u.), which correspond to $\mathcal{E}_{\text{kin}} = 2$ a.u. electron energy. However, this scaling of the largest probability of photoelectron energies with the value of the electric field's amplitude is given by the expression $\mathcal{E}^{(2)}_{\text{kin,max}}/\mathcal{E}^{(1)}_{\text{kin,max}} = \left(E_0^{(2)}/E_0^{(2)}\right)^2$ , which for the discussed cases gives a factor of 16 magnification in maximum electron energy by increasing the amplitude from 0.25 a.u. to 1 a.u.. The linear scaling between $k_{\text{max}}$ and $E_0$ is obvious by looking at the plots calculated for the four different intensity fields.

The second observation that can be made, is that the photoelectron spectra image becomes more and more complicated by increasing the external field's strength. As one can see, in the lowest case very few features are appearing in the spectra, while for the largest

$E_0$ value the pattern becomes quite complex. This increase in the complexity of the PES images can be explained by the following. As the intensity of the radiation is higher the dynamics of the continuum EWPs get more diversified. Moreover, it can be observed that well structured minimum radial patterns appeared in all cases, which are interference minima of the signal and reference EWPs. These minima patterns were showed that are depending on the $z_0$ maximum distance that the signal electron reached before the return to the parent ion, which parameter is directly controlled by the intensity of the laser field (by increasing $E_0$ the value of $z_0$ also increases).

Beside these two first sight observations, another aspects regarding the structure of the PESs should be mentioned. It can be observed, that by increasing the field amplitude the number of radial interference minima appearing at the forward ejection region ($k_z > 0$) increased. By considering only the upper part of the forward ejection region ($k_x > 0$, $k_z > 0$) in the case of $E_0 = 0.25$ a.u. two minima are present, while by increasing the field amplitude, for $E_0 = 0.5$ a.u. the number of minima is increased to 3. By going even further this value is raised to 4 and to 5 by using $E_0 = 0.75$ a.u., and $E_0 = 1$ a.u. fields, respectively. This number of interference minima is again the direct consequence of the strength of the radiation field, which by getting increased drives the signal EWP to larger and larger $z_0$ distances.

Another interesting feature that appears in the PES occurs when the intensity of the laser field is increased to $E_0 = 0.75$ a.u. and above that: $E_0 = 1$ a.u. [Figures 7.23/(c)-(d)]. As it can be observed for these high intensity laser pulses in the low momentum part of the spectra a second interference pattern is present. For $E_0 = 0.75$ a.u. this secondary structures are located at $k_z < 1$, while for $E_0 = 1$ a.u. appear below the parallel momentum component value $k_z < 1.5$ a.u.. These two distinct interference pattern regions that are obtained for the high intensity fields are due to two different interference mechanisms. While in the case of lower field strengths (i.e., $E_0 \in \{0.25, 0.5\}$) only the primary dominant mechanism is observable, i.e., interference between EWPs created during the same half optical cycle, for higher electric field strengths a secondary mechanism can be detectable, which can be attributed to an additional ejection of EWPs (a secondary pair of a reference and signal EWP) happening at a different half optical cycle. This secondary mechanism as it can be observed in the last two subfigures of Fig. 7.23 modifies the low momentum part of the primary pattern, which can be simply explained by the difference in the value of the vector potential $\vec{A}(t)$ in the moments of these two optical half-cycles (i.e., in the instances) when these two pairs of EWPs are ejected into the continuum by the radiation field.

The developed and implemented numerical method - presented in this principal part of the work - for the direct solution of the time-dependent Schrödinger equation for the laser irradiated diatomic molecule with a single active electron was partly or entirely employed in several investigations, where the obtained results were presented in several ISI articles and at numerous international conferences:[3]

[3]Publications

ISI articles:

G.Zs. Kiss, S. Borbély, A. Tóth, and L. Nagy, *Photoelectron holography of the $H_2^+$ molecule* [sent to publication] .
G.Zs. Kiss, S. Borbély, and L. Nagy, *Efficient numerical method for investigating diatomic molecules with single active electron subjected to intense and ultrashort laser fields* AIP Conf. Proc. **1916**, 020010 (2017).
A. Tóth, S. Borbély, G.Zs. Kiss, G. J. Halász, and Á. Vibók, *Towards the Full Quantum Dynamical Description of PhotonInduced Processes in $D_2^+$* J. Phys. Chem. A **120**, 9411 (2016).
G.Zs. Kiss, S. Borbély, and L. Nagy, *An efficient numerical discretization method for the study of the $H_2^+$ in intense laser fields*, AIP Conf. Proc. **1694**, 200171 (2015).

Oral presentations at international conferences:

G.Zs. Kiss, S. Borbély, L. Nagy, *Photon Induced Electron Dynamics in Diatomic Molecules by XUV Laser Pulses*, Joint ISCP-INDLAS Conference organized by National Institute for Laser Plasma & Radiation Physics (INFLPR), 03-07 September 2018, Alba-Iulia, Romania
G.Zs. Kiss, S. Borbély, L. Nagy, *Efficient Numerical Method for Investigating Diatomic Molecules in Intense and Ultrashort laser Fields*, TIM17 Physics Conference, organized by the West University of Timişoara, 25-27 May 2017, Timişoara, Romania

CHAPTER 8.

# Conclusions and outlook

In the first part of the thesis I have presented two different theoretical approaches that were implemented to investigate laser induced electron dynamics in small atomic systems. The first approach was a semi-classical method based on the *strong-field approximation* (SFA) scheme, where the simple three step model of SFA was used and the acceleration of the tunnel-ionized electron calculated in the presence of the oscillating field. In the recombination process of the ionized electron to the parent ion - which mechanism is responsible for the creation of the *high harmonic generation* (HHG) pulses - was included also the Stark-shift of the ground state of the hydrogen atom in the presence of the oscillatory electric field, and the characteristics of the high harmonic spectra were investigated as a function of laser parameters. With the implemented method the expected increase of the HHG plateau was obtained, where the last (highest energy) harmonic in the plateau region is resulted from the reabsorption of an electron that releases its $3.17U_p + I_p$ exes energy gained from the radiation field and $U_p$ (ponderomotive energy) increased with increasing the wavelength or the electric field amplitude of the laser pulse ($U_p \sim \lambda^2 E_0^2$). The obtained behavior of the HHG spectra may give us further possibilities to introduce the (CPU parallelized) calculations into more complex numerical codes, where the macroscopic effects of the laser propagation through medium are investigated.

Beside this semi-classical approach, that was used to calculate the dynamics of the reabsorbed laser driven electrons, two other methods were presented as well, which were based on the solution of the *time-dependent Schrödinger equation* (TDSE), and which can be used to extract a full physical picture regarding the behavior of ejected electronic wave packets. For the solution of the TDSE two different approaches were presented and numerically implemented, an *iterative solution* and the *direct solution* of the *momentum space TDSE*, which were employed to calculate and compare the laser induced photoelectron spectra obtained for the hydrogen atom.

In the principle part of the present thesis the photoelectron holography of a diatomic molecule considered with a single active electron was studied. This goal was achieved by implementing first a numerical method which is based on the direct solution of the TDSE for the XUV laser field irradiated system. As target the $H_2^+$ molecule was considered and

the interaction with a few-cycle (ultrashort) XUV laser pulse was investigated. The electronic wave function and the Hamiltonian of the system was represented in the *prolate spheroidal coordinate* system and on a *finite-element discrete variable representation* (FE-DVR) grid, where in each finite element the wave function was expanded in the basis of local Lagrange interpolating polynomials. As the first step the accuracy of the grid representation was checked, and accurate/convergent bound state energies and wave functions of $H_2^+$ were obtained by the direct diagonalization of the field-free Hamiltonian. With the calculated bound states accurate *potential energy curve* and *electronic transition dipole moments* were obtained which can be included in further calculations where the nuclear dynamics are also involved in the laser induced processes. Another important element in the study of the laser induced electron dynamics was the calculation of the initial (ground) state wave function of the target, which was later on propagated in time by using the short-iterative Lanczos algorithm. In this time propagation scheme a *complex absorbing potential* (CAP) was also built in to eliminate the reflections from the edge of the simulation box, and to control the size of the grid (i.e., if absorption is detected at the CAP, then the size of the simulation box is extended) in order to reduce as much as possible the absorptions at the boundary (i.e., to decrease the information losses at the end of the simulation box). With the implementation of the time-propagation algorithm the electron dynamics was investigated: first, the occupation probabilities of different bound states as a function of time for different field intensities. The major dynamics and there occurrence in time were identified, and it was shown that a not negligible contribution from different bound states still remained in the *time-dependent wave function* (TDWF) after the conclusion of the external field. These remnant small contributions were removed from the wave function prior to calculating the *photoelectron spectra* (PES) in order to reduce the possible error that the projection of the TDWF onto the approximate one-center continuum states would bring into the image of the spectra. Using the presented theoretical tool the dependence of the photoelectron spectra as a function of molecular internuclear distance was studied.

The accurate PES and *photoelectron holograms* (i.e., interference patterns created in the PES by the interference between the scattered and reference electronic wave packets) were obtained after performing rigorous convergence tests, implying the convergence as a function of number of the subtracted bound states and as a function of propagation time after the completion of the laser field.

In order to identify how the spatial profile of the molecular binding potential influences the shape of the photoelectron spectra obtained for the $H_2^+$ also a one-center model system ($H_{2\mathrm{mod}}^+$) with the same ionization energy and long range potential as $H_2^+$ was considered. Provided that the same XUV pulses were used and the aforementioned conditions were satisfied when constructing the potential of the model system, similar scattered and reference *electronic wave packet* (EWP) trajectories were produced for both targets. As expected, roughly similar PESs were obtained for both systems, and it was shown that the differences between the calculated patterns are the direct consequence of the differences in the parent

ion's binding potential that the rescattering (signal) electron meets along the returning path: higher density minima locations are obtained if the potential along the signal path was deeper.

Furthermore, it was shown that the locations of the PES minima obtained for the $H_2^+$ molecule changed as the internuclear separation $R$ was modified. As the internuclear separation $R$ was increased a denser interference pattern was observed, which is the result of the interplay between two opposite factors. First, by increasing $R$ the ionization energy of the target molecule became lower, which implicitly means that the ionized electron had a higher initial velocity. As a consequence, this electron departed at a larger distance measured from the parent ion, meaning a higher $z_0$ parameter before the returning event. If the value of $z_0$ is increased a higher density in the hologram appears. However, the second factor weakened this effect, since for higher $R$ internuclear distances the signal electron met a shallower binding potential, hence the density of the hologram was decreased. As future perspectives, further investigations may be carried out in order to identify and to quantify the effects of these two distinct processes that are responsible for the shift of the minima location in the photoelectron spectrum, which opens the possibility of extracting information from the photoelectron hologram regarding for example the value of internuclear distance in the instance, when the signal and direct electronic wave packets were emitted into the continuum.

According to the calculated EWP dynamics it was shown that the dominant EWPs, which are responsible for the creation of the well identifiable interference minima appearing in the PES, were "born" in the second and third optical half-cycle of the oscillating field, while obvious presence of the *two-center interference* effects (expected as horizontal interference patterns parallel to the $k_x$ axis) were not detectable in the photoelectron holograms. This could be explained by the fact that these EWPs can be decomposed into smaller EWPs which on the other hand are shifted in the momentum space in accordance with the value of the external field's vector potential in their creation moment, and when these smaller EWPs are coherently added the two-center interference pattern is most probably averaged out. However, by carefully analyzing the PES of the $H_2^+$ molecule along the first minimum, traces of the two-center interference appeared to be present as a modulation in the depth of the spatial interference minimum (near the location where it was predicted by simple models).

In the final part of this work the features of the holograms were investigated as a function of field intensity, and it was found that for high external electric field strengths more interference minima appeared in the PESs (higher interference pattern density) and more complex patterns were obtained. The higher complexity of the holographic patterns obtained for the higher intensity fields is due to the fact that a secondary EWP interference mechanisms appeared in the lower momentum part of the photoelectron spectra.

The developed method opens further possibilities to calculate PESs for numerous internuclear separations (provided that a sufficiently large CPU time is available) and to identify the density of the interference patterns as a function of $R$, while also other investigations may

be carried out by using different ultrashort laser pulses, where the inclusion of the nuclear dynamics may be the next goal.

# Acknowledgements

Firstly, I would like to thank my supervisor, Prof. Dr. Ladislau Nagy for his continuous support of my PhD studies and for giving me the opportunity to be part of his research group at the Faculty of Physics at Babeş-Bolyai University (UBB) Cluj-Napoca. His expertise and knowledge helped me considerably to better understand the investigated processes and to correctly interpret the obtained results. I am very thankful to him, for the encouragement during the last years of my studies, when he also supported me to start new collaborations with internationally recognized research groups as the "Laser induced phenomena" group of Dr. Valer Toşa in the National Institute for Research and Development of Isotopic and Molecular Technology, Cluj-Napoca (INCDTIM), or the "Ultrafast and attosecond physics" group lead by Dr. Péter Dombi in MTA Wigner Research Centre for Physics, Budapest. Hereby, I also acknowledge Valer Toşa and Péter Dombi for accepting me in their groups.

I would also like to thank Prof. Dr. Nicolae Avram (Faculty of Physics, West University of Timişoara), Dr. Attila Bende (Senior Researcher I, Molecular and Biomolecular Physics Department, National Institute for R&D of Isotopic and Molecular Technologies Cluj-Napoca) and Associate Professor Dr. Ferenc Járai-Szabó (Faculty of Physics, Babeş-Bolyai University Cluj-Napoca) for accepting to be part of my thesis jury.

I would like to deeply thank Lect. Dr. Sándor Borbély (UBB) and Dr. Katalin Kovács (INCDTIM) for giving me the opportunity to be part of their research projects, and for their valuable scientific guidance, that facilitated the correct understanding of the studied processes that emerge in this continuously developing field of physics. I am especially thankful to Sándor, who tirelessly helped me and answered all of my questions related to the numerics and physics throughout these years.

I am also greatly thankful to my colleagues at the Babeş-Bolyai University, Dr. Tóth Attila, Dr. Tóth István, Lect. Dr. Nagy Katalin, Lect. Dr. Szabó László, drd. Papp István, and to my colleagues at the INCDTIM research institute, Dr. Ana Maria Mihaela Gherman, Dr. Alexandra Fălămaş, Dr. Cosmin Farcău, Dr. Alexandra Fărcaş, drd. Alex-Adrian Fărcaş and drd. Călin Firţa, for the friendly atmosphere in the shared offices, and the numerous valuable professional and personal discussions.

My sincere thanks also goes to Dr. Ioan Turcu, who as the head of the Dept. Molecular and Biomolecular Physics at INCDTIM Cluj-Napoca untiringly strives to offer us the best working environment possible at the research institute.

I would like to thank Prof. Dr. Fernando Martín as well for having me for two months in his "XChem" research group at Autonomous University of Madrid. This opportunity was an important and useful step in my professional progress. My thanks also goes to Dr. Czirják Attila professor of physics at University of Szeged who invited me for three month to his research group in Szeged.

During my PhD studies all the scientific work was possible with financial background secured by the participation in several scientific projects financed by the Romanian National Authority for Scientific Research: PN-II-ID-PCE-2011-3-0192, PN-II-RU-TE-2014-4-0425, RO-CERN 03ELI/01.09.2016 (PROPW), or the international project COST Action no. CM1204 XUV/X-ray, which also supported my research visit in Madrid. My studies were mainly supported by the scholarship provided by the Romanian state, and in other occasions by different scholarships financed by the Hungarian governments Secretariat of State for National Policy via the Collegium Talentum and "Soós Kálmán" programmes. I also acknowledge the Erasmus placement programme for financing my stay in Szeged.

Certainly, I want to express my gratitude towards my secondary school physics teachers, Mr. László József and Mrs. Szász Ágota, who introduced me into the interesting and fascinating field of physics leading me to choose it as an academic and scientific path.

My biggest thanks, however, goes to my family, to my parents, brother, and my loving wife who all encouraged me with their continuous care and moral support throughout these years. I am deeply grateful to them. Finally, I would like to dedicate my thesis to my lovely - less than one year old - daughter, Zsolna.

# List of publications

ISI articles indexed in Web of Science (Knowledge) database:

G.Zs. Kiss, S. Borbély, A. Tóth, and L. Nagy, *Photoelectron holography of the $H_2^+$ molecule* [sent to publication] .

G.Zs. Kiss, S. Borbély, and L. Nagy, *Efficient numerical method for investigating diatomic molecules with single active electron subjected to intense and ultrashort laser fields* AIP Conf. Proc. **1916**, 020010 (2017).

A. Tóth, S. Borbély, G.Zs. Kiss, G. J. Halász, and Á. Vibók, *Towards the Full Quantum Dynamical Description of PhotonInduced Processes in $D_2^+$* J. Phys. Chem. A **120**, 9411 (2016).

G.Zs. Kiss, S. Borbély, and L. Nagy, *An efficient numerical discretization method for the study of the $H_2^+$ in intense laser fields*, AIP Conf. Proc. **1694**, 200171 (2015).

G. Zs. Kiss, S. Borbély, L.Nagy, *Momentum Space Iterative Solution of the Time-Dependent Schrödinger Equation*, AIP Conf. Proc. **1564**, 78 (2013).

S. Borbély, G. Zs. Kiss, L. Nagy, *The Excitation and Ionization of the Hydrogen Atom In Strong Laser Fields*, Central European Journal of Physics **8**, 249 (2010).

other (non-ISI article) publication:

Kiss Gellért Zsolt *et al.*, (in Hungarian) *"Numerikus módszerek intenzív lézertér és atomok közötti kölcsönhatás elméleti tanulmányozására"*, Conf. proc.: "A fizika, matematika és művészet találkozása az oktatásban, kutatásban"/ ISBN 978-963-284-346-9, ELTE TTK (2013).

# Oral presentations at international conferences

G.Zs. Kiss, S. Borbély, L. Nagy, *Photon Induced Electron Dynamics in Diatomic Molecules by XUV Laser Pulses*, Joint ISCP-INDLAS Conference organized by National Institute for Laser Plasma & Radiation Physics (INFLPR), 03-07 September 2018, Alba-Iulia, Romania

G.Zs. Kiss, S. Borbély, L. Nagy, *Efficient Numerical Method for Investigating Diatomic Molecules in Intense and Ultrashort laser Fields*, TIM17 Physics Conference, organized by the West University of Timişoara, 25-27 May 2017, Timişoara, Romania

G.Zs. Kiss, S. Borbély, L. Nagy, *The Numerical Solution of The Time-Dependent Schrödinger Equation for Atoms in Intense Laser Fields*, PHYSICS CONFERENCE TIM-12 organized by the West University of Timişoara, 27-30 November 2012, Timişoara, Romania

# Poster presentations at international conferences

"Laser-atom interaction beyond the strong field approximation model" [Processes in Isotops and Molecules (PIM) 11th International Conf., Cluj, RO, 27-29/09/2017]

"Efficient numerical method for investigating diatomic molecules with single active electron subjected to intense and ultrashort XUV laser fields." [14th International Conference on Multiphoton Processes, Budapest, HU, 24-27/09/2017]

"Theoretical Investigation Beyond the Strong Field Approximation Model" [TIM17 Physics Conference, Timioara, Romania, 25-27/05/2017]

"Theoretical Study of the Dihydrogen Cation Irradiated with Intense XUV Laser Fields" [TIM17 Physics Conference]

"Numerical Method to Investigate Diatomic Molecules with Single Active Electron Subjected to Intense Laser Fields" [4th XLIC General Meeting, Prague,Czechia, 14-16/03/2017]

"Numerical investigations beyond the SFA model." (G.Zs. Kiss, K.Kovács, V. Toa) [MEDEA: Ultrafast Dynamics with Intense Radiation Sources, Crete, Greece, 18-22/10/2016]

"Investigation of the Electronic Wave Packet Dynamics of the $H_2^+$ Molecule Subjected to External Laser Field" [XUV/X-ray light and fast ions for ultrashort chemistry (XLIC) 3rd General Meeting, Debrecen, HU, 2-4/09/2015]

"Investigation of the $H_2^+$ molecule by strong, ultrashort laser pulses" [Workshop 2015: "Photon and fast Ion induced Processes in Atoms, Molecules and Nanostructures" (PIPAMON), Debrecen, 24-26/03/2015]

"Photionization of Atoms and Molecules ($H_2^+$) Irradiated with Ultrashort and Strong Laser Pulses" (G.Zs.Kiss et al.) [Work shop: Autumn School on Laser Dynamics, Bolyai Institute, University of Szeged, 24-28/09/2014, Szeged, HU]

"Ionization of The $H_2^+$ Molecule by Ultrashort EUV/XUV Laser Pulses" (G.Zs.Kiss, et al) [COST CM1204 Madrid, 11-13/09/2013]

"Numerical Method for The Investigation of $H_2^+$ Molecule In External XUV Laser Field" ["PHYSICS CONFERENCE TIM-14" organised by the West University of Timisoara, 27-30/09/2012, RO]

Solving the TDSE by Using Levin's Integration Method (G.Zs. Kiss, S.Borbély, L.Nagy) [4th anual meeting of the COST Action CUSPFEL, 21-23/03/2012, Cluj, Romania]

# Poster contributions

"Dissociative ionization of $D_2^+$ in strong laser fields." (**A. Tóth**, S. Borbély, G.Zs. Kiss, G. Halász, and Á. Vibók) [MEDEA: Ultrafast Dynamics with Intense Radiation Sources, Crete, Greece, 18-22/10/2016]

Iterative Solution of The Time-Dependent Schrödinger Equation (**S. Borbély**, G.Zs. Kiss, L.Nagy) [44th CONF. ON THE EUROPEAN GROUP ON ATOMIC SYSTEMS, 9-13/07/2012, Göthenburg]

Appendix I.

# Atomic Units

| Dimension | Symbol/Expression | Value in SI units |
|---|---|---|
| Mass of the electron | $m_e$ | $9.109 \times 10^{31}$ kg |
| Reduced Planck constant | $\hbar = h/(2\pi)$ | $6.626 \times 10^{-34}/(2\pi)$ J·s |
| Coulomb's constant | $1/(4\pi\varepsilon_0)$ | $8.99 \times 10^9$ N $\cdot$ m$^2$ $\cdot$ C$^{-2}$ |
| Elementary charge | $e$ | $1.602 \times 10^{-19}$ C |
| Length (Bohr radius) | $a_0$ | $0.528 \times 10^{-10}$ m |
| Energy (1 Hartree is twice the ionization potential of H atom) | $E_h$ | 27.21 eV |
| Time | $\hbar/E_h$ | $2.41 \times 10^{-18}$ s |
| Velocity (electron velocity on first Bohr orbit) | $v_0$ | $2.18 \times 10^6$ m/s |
| Momentum | $\hbar/a_0$ | $1.992 \times 10^{-24}$ kg $\cdot$ m/s |
| Force | $E_h/a_0$ | $8.238 \times 10^{-8}$ N |
| Electric field strength | $E = e/a_0$ | $5.14 \times 10^{11}$ V/m |
| Intensity of the laser field ($E = 1$ a.u.) | $\varepsilon_0 c E^2/2$ | $3.51 \times 10^{16}$ W/cm$^2$ |
| Electric dipole moment | $ea_0$ | $8.478 \times 10^{-30}$ C $\cdot$ m |
| Electric potential | $E_h/e$ | 27.21 V |

Appendix II.

# Coordinate Transformations

Spherical ← Prolate spheroidal

$$\begin{aligned} r &= \frac{R}{2}\sqrt{\xi^2+\eta^2-1}; \\ \theta &= \arccos\frac{\xi\eta}{\sqrt{\xi^2+\eta^2-1}}; \\ \varphi &= \varphi \text{ (azimuthal angle).} \end{aligned}$$

Prolate spheroidal ← Spherical

$$\begin{aligned} \xi &= \frac{r_\mathrm{A}+r_\mathrm{B}}{R} = \frac{\sqrt{r^2+\frac{R^2}{4}+rR\cos\theta}+\sqrt{r^2+\frac{R^2}{4}-rR\cos\theta}}{R}; \\ \eta &= \frac{r_\mathrm{A}-r_\mathrm{B}}{R} = \frac{\sqrt{r^2+\frac{R^2}{4}+rR\cos\theta}-\sqrt{r^2+\frac{R^2}{4}-rR\cos\theta}}{R}; \end{aligned}$$

Cartesian ← Prolate spheroidal

$$\begin{aligned} x &= \frac{R}{2}\sqrt{(\xi^2-1)(1-\eta^2)}\cos\varphi; \\ y &= \frac{R}{2}\sqrt{(\xi^2-1)(1-\eta^2)}\sin\varphi; \\ z &= \frac{R}{2}\xi\eta. \end{aligned}$$

Prolate spheroidal ← Cartesian

$$\begin{aligned} \xi &= \frac{\sqrt{x^2+y^2+\left(z+\frac{R}{2}\right)^2}+\sqrt{x^2+y^2+\left(z-\frac{R}{2}\right)^2}}{R}; \\ \eta &= \frac{\sqrt{x^2+y^2+\left(z+\frac{R}{2}\right)^2}-\sqrt{x^2+y^2+\left(z-\frac{R}{2}\right)^2}}{R}; \\ \varphi &= \arctan\frac{y}{x}. \end{aligned}$$

Spherical ← Cartesian

$$\begin{aligned} r &= \sqrt{x^2+y^2+z^2}; \\ \theta &= \arccos\frac{z}{\sqrt{x^2+y^2+z^2}}; \\ \varphi &= \arctan\frac{y}{x}. \end{aligned}$$

Cartesian ← Spherical

$$\begin{aligned} x &= r\sin\theta\cos\varphi; \\ y &= r\sin\theta\sin\varphi; \\ z &= r\cos\theta. \end{aligned}$$

# Bibliography


[1] A. L. Schawlow and C. H. Townes. Infrared and optical masers. *Phys. Rev.*, 112:1940–1949, Dec 1958.

[2] T. Maiman. Stimulated optical radiation in ruby. *Nature (London)*, 187:493, 1960.

[3] B. Baier, A. Kern, L. Kaderali, B. Bis, D. Koschel, and A. Rolle. Retrospective survival analysis of 237 consecutive patients with multiple pulmonary metastases from advanced renal cell carcinoma exclusively resected by a 1318-nm laser. *Interact Cardiovasc Thorac Surg.*, 21:211–217, 2015.

[4] G. Bertino, G. Degiorgi, C. Tinelli, and et al. Co2 laser cordectomy for t1-t2 glottic cancer: Oncological and functional long-term results. *Eur Arch Otorhinolaryngol*, 272:2389–2395, 2015.

[5] D.S. Fink, H. Sibley, M. Kunduk, and et al. Subjective and objective voice outcomes after transoral laser microsurgery for early glottic cancer. *Laryngoscope*, 126:405–407, 2016.

[6] T. Sakimoto, M.I. Rosenblatt, and D.T. Azar. Laser eye surgery for refractive errors. *The Lancet*, 367:1432–1447, 2006.

[7] D. Ortega-Concepcin, J.A. Cano-Durn, J.-F. Pea-Cardelles, V.-M. Paredes-Rodrguez, J. Gonzlez-Serrano, and J. Lpez-Quiles. The application of diode laser in the treatment of oral soft tissues lesions. a literature review. *J Clin Exp Dent.*, 9:925–928, 2017.

[8] E. Azma and N. Safavi. Diode laser application in soft tissue oral surgery. *J Lasers Med Sci.*, 4:206, 2013.

[9] B.M. Toregard. Laser applications in cosmetic surgery. *Ann Chir Gynaecol*, 79:208, 1990.

[10] W. Yu, M.Y. Yu, H. Xu, and Y.W. Tian. Intense local plasma heating by stopping of ultrashort ultraintense laser pulse in dense plasma. *Laser and Particle Beams*, 25:661–638, 2007.

[11] K. Ikeda et al. Selective crystallization of the metastable phase of indomethacin at the interface of liquid/air bubble induced by femtosecond laser irradiation. *Applied Physics Express*, 8:045501, 2015.

[12] V. Lazar. World premiere: The laser in magurele has reached peak power 10 petawatts, 13.03.2019.

[13] G.A. Mourou and V. Yanovsky. Relativistic optics: A gateway to attosecond physics. *Optics and Photonics News*, 15:40–45, 2004.

[14] A. Einstein. Über einen die erzeugung und verwandlung des lichtes betreffenden heuristischen gesichtspunkt. *Annalen der Physik*, 17:132–148, 1905.

[15] M. Planck. Über eine verbesserung der wien'schen spectralgleichung. *Verhandlungen der Deutschen Physikalischen Gesellschaft*, 2:202–204, 1900.

[16] M. Peters, T.-T. Nguyen-Dang, E. Charron, A. Keller, and O. Atabek. Laser-induced electron diffraction: A tool for molecular orbital imaging. *Phys. Rev. A*, 85, 2012.

[17] Y. Ito, C. Wang, A.-T. Le, M. Okunishi, D. Ding, C.D. Lin, and K. Ueda. Extracting conformational structure information of benzene molecules via laser-induced electron diffraction. *Struct Dyn.*, 3:034303, 2016.

[18] G. Porat, G. Alon, S. Rozen, O. Pedatzur, M. Krüger, D. Azoury, A. Natan, G. Orenstein, B. D. Bruner, M.J.J. Vrakking, and N. Dudovich. Attosecond time-resolved photoelectron holography. *Nature Communications*, 9, 2018.

[19] F. Krausz and M. Ivanov. Attosecond physics. *Rev. Mod. Phys.*, 81, 2009.

[20] M. Nisoli, P. Decleva, F. Calegari, A. Palacios, and F. Martín. Attosecond electron dynamics in molecules. *Chem. Rev.*, 16, 2017.

[21] A. Palacios, A. González-Castrillo, and F. Martín. Molecular interferometer to decode attosecond electronnuclear dynamics. *PNAS*, 111, 2014.

[22] D. Jelovina, J. Feist, F. Martín, and A. Palacios. A pump-probe scheme with a single chirped pulse to image electron and nuclear dynamics in molecules. *New Journal of Physics*, 20, 2018.

[23] J. Gonzalez-Vazquez, Z. Masin, D.S. Brambilla, A.G. Harvey, F. Morales, and F. Martín. Ultrafast imaging of laser-controlled non-adiabatic dynamics in no2 from time-resolved photoelectron emission. *Physical Chemistry Chemical Physics*, 21, 2019.

[24] N.E. Henriksen. Laser control of chemical reactions. *Chem. Soc. Rev.*, 31:37–42, 2002.

[25] A.H. Zewail. Femtochemistry: atomic-scale dynamics of the chemical bond. *J. Phys. Chem*, 104:5660–5694, 2000.

[26] A. Einstein. The quantum theory of radiation. *Physikalische Zeitschrift*, 18:121, 1917.

[27] J.P. Gordon, H.J. Zeiger, and C.H. Townes. The masernew type of microwave amplifier, frequency standard, and spectrometer. *Phys. Rev.*, 99:1264, 1955.

[28] A. L. Schawlow and C. H. Townes. Infrared and optical masers. *Phys. Rev.*, 112:1940–1949, Dec 1958.

[29] M.J. Weber. *Handbook of laser wavelengths*. CRC Press, 1999.

[30] P.B. Corkum. Plasma perspective on strong field multiphoton ionization. *Physical Review Letters*, 71:1994, 1993.

[31] J.E. Bayfield and P.M. Koch. Multiphoton ionization of highly excited hydrogen atoms. *Physical Review Letters*, 33:258, 1974.

[32] M. Lewenstein, Ph. Balcou, M. Yu. Ivanov, Anne L'Huillier, and P. B. Corkum. Theory of high-harmonic generation by low-frequency laser fields. *Phys. Rev. A*, 49:2117–2132, Mar 1994.

[33] A. L'Huillier, Ph. Balcou, S. Candel, K.J. Schafer, and K.C. Kulander. Calculations of high-order harmonic-generation processes in xenon at 1064 nm. *Phys. Rev. A*, 46:2778–2790, Sep 1992.

[34] P. Rácz, V. Ayadi, and P. Dombi. On the role of rescattering and mirror charge in in ultrafast nanooptical field probing with electrons. *J. Opt.*, 20:015501, 2018.

[35] Christoph B. Burckhardt Robert J. Collier and Lawrence H. Lin. *Optical Holography*. Academic Press, 1971.

[36] D. Gabor. A new microscopic principle. *Nature*, 161:777, May 1948.

[37] Y. Huismans, A. Rouzée, A. Gijsbertsen, J.H. Jungmann, A.S. Smolkowska, P.S.W.M. Logman, F. Lépine, S. Zamith C. Cauchy, T. Marchenko, J.M. Bakker, G. Berden, B. Redlich, A.F.G. van der Meer, H.G. Muller, W. Vermin, K.J. Schafer, M. Spanner, M.Yu. Ivanov, O. Smirnova, D. Bauer, S.V. Popruzhenko, and M.J.J. Vrakking. Time-resolved holography with photoelectrons. *Science*, 331:61 – 64, 2011.

[38] T. Marchenko, Y. Huismans, K. J. Schafer, and M. J. J. Vrakking. Criteria for the observation of strong-field photoelectron holography. *Phys. Rev. A*, 84:053427, Nov 2011.

[39] X.-B. Bian, Y. Huismans, O. Smirnova, K.-J. Yuan, M.J.J. Vrakking, and A.D. Bandrauk. Subcycle interference dynamics of time-resolved photoelectron holography with midinfrared laser pulses. *Phys. Rev. A*, 84:043420, Oct 2011.

[40] D.G. Arbó, E. Persson, and J. Burgdörfer. Time double-slit interferences in strong-field tunneling ionization. *Phys. Rev. A*, 74:063407, Dec 2006.

[41] Y. Huismans, A. Gijsbertsen, A.S. Smolkowska, J.H. Jungmann, A. Rouzée, P.S.W.M. Logman, F. Lépine, C. Cauchy, S. Zamith, T. Marchenko, J.M. Bakker, G. Berden, B. Redlich, A.F.G. van der Meer, M. Yu. Ivanov, T.-M. Yan, D. Bauer, O. Smirnova, and M.J.J. Vrakking. Scaling laws for photoelectron holography in the midinfrared wavelength regime. *Phys. Rev. Lett.*, 109:013002, Jul 2012.

[42] D.D. Hickstein, P. Ranitovic, S. Witte, X.-M. Tong, Y. Huismans, P. Arpin, X. Zhou, K.E. Keister, C.W. Hogle, B. Zhang, C. Ding, P. Johnsson, N. Toshima, M.J.J. Vrakking, M.M. Murnane, and H.C. Kapteyn. Direct visualization of laser-driven electron multiple scattering and tunneling distance in strong-field ionization. *Phys. Rev. Lett.*, 109:073004, Aug 2012.

[43] S. Borbély, A. Tóth, K. Tőkési, and L. Nagy. Spatial and temporal interference during the ionization of h by few-cycle xuv laser pulses. *Phys. Rev. A*, 87:013405, Jan 2013.

[44] H. Agueny and J.P. Hansen. High-order photoelectron holography in the midinfrared-wavelength regime. *Phys. Rev. A*, 98:023414, Aug 2018.

[45] S. Borbély, A. Tóth, D. G. Arbó, K. Tőkési, and L. Nagy. Photoelectron holography of atomic targets. *Phys. Rev. A*, 99:013413, Jan 2019.

[46] S. López and D. Arbo. Holographic interferences in photoelectron spectra: different approaches. *The European Physical Journal D*, 73:28, Feb 2019.

[47] M. Okunishi, T. Morishita, G. Prümper, K. Shimada, C. D. Lin, S. Watanabe, and K. Ueda. Experimental retrieval of target structure information from laser-induced rescattered photoelectron momentum distributions. *Phys. Rev. Lett.*, 100:143001, Apr 2008.

[48] S. Micheau, Zhangjin Chen, A. T. Le, J. Rauschenberger, M. F. Kling, and C. D. Lin. Accurate retrieval of target structures and laser parameters of few-cycle pulses from photoelectron momentum spectra. *Phys. Rev. Lett.*, 102:073001, Feb 2009.

[49] Junliang Xu, Zhangjin Chen, Anh-Thu Le, and C. D. Lin. Self-imaging of molecules from diffraction spectra by laser-induced rescattering electrons. *Phys. Rev. A*, 82:033403, Sep 2010.

[50] C D Lin, Anh-Thu Le, Zhangjin Chen, Toru Morishita, and Robert Lucchese. Strong-field rescattering physics – self-imaging of a molecule by its own electrons. *Journal of Physics B: Atomic, Molecular and Optical Physics*, 43(12):122001, 2010.

[51] Cosmin I. Blaga, Junliang Xu, Anthony D. DiChiara, Emily Sistrunk, Kaikai Zhang, Pierre Agostini, Terry A. Miller, Louis F. DiMauro, and C. D. Lin. Imaging ultrafast molecular dynamics with laser-induced electron diffraction. *Nature*, 483:194 – 197, 2012.

[52] S. Borbély, A. Tóth, K. Tőkési, and L. Nagy. Laser-induced electron diffraction in a pumpprobe setup using half-cycle electric pulses. *Physica Scripta*, 2013(T156):014066, 2013.

[53] A. Tóth, S. Borbély, K. Tőkési, and L. Nagy. Ionization of atoms by few-cycle euv laser pulses: carrier-envelope phase dependence of the intra-pulse interference effects. *The European Physical Journal D*, 68(11):339, 2014.

[54] X.-B. Bian and A.D. Bandrauk. Attosecond time-resolved imaging of molecular structure by photoelectron holography. *Phys. Rev. Lett.*, 108:263003, Jun 2012.

[55] M. Meckel, A. Staudte, S. Patchkovskii, D. M. Villeneuve, P. B. Corkum, R. Doerner, and M. Spanner. *NATURE PHYSICS*, 10(8):594–600, 2014.

[56] X.-B. Bian and A.D. Bandrauk. Orientation-dependent forward-backward photoelectron holography from asymmetric molecules. *Phys. Rev. A*, 89:033423, Mar 2014.

[57] K.-J. Yuan, X.-B. Bian, and A.D. Bandrauk. Two-center interference in molecular photoelectron energy spectra with intense attosecond circularly polarized xuv laser pulses. *Phys. Rev. A*, 90:023407, Aug 2014.

[58] W. Yang, Z. Sheng, X. Feng, M. Wu, Z. Chen, and X. Song. Molecular photoelectron holography with circularly polarized laser pulses. *Opt. Express*, 22(3):2519–2527, Feb 2014.

[59] L. Chen, C. Huang, X. Zhu, P. Lan, and P. Lu. Molecular photoelectron holography by an attosecond xuv pulse in a strong infrared laser field. *Opt. Express*, 22(17):20421–20431, Aug 2014.

[60] M. Li, X. Sun, X. Xie, Y. Shao, Y. Deng, C. Wu, Q. Gong, and Y. Liu. Revealing backward rescattering photoelectron interference of molecules in strong infrared laser fields. *Scientific Reports*, 5:8519.

[61] H. Marko, X.-B. Bian, M. Spanner, A. Staudte, and P.B. Corkum. Probing molecular dynamics by laser-induced backscattering holography. *Phys. Rev. Lett.*, 116:133001, Apr 2016.

[62] Y. Li, Y. Zhou, M. He, M. Li, P. Lan, and P. Lu. Time-resolved internal-electron-scattering effect of $H_2^+$ in enhanced ionization regions. *Phys. Rev. A*, 94:013422, Jul 2016.

[63] M. He, Y. Zhou, Y. Li, M. Li, and P. Lu. Revealing the target structure information encoded in strong-field photoelectron hologram. *Optical and Quantum Electronics*, 49(6):232, May 2017.

[64] H. Miyagi, T. Morishita, and S. Watanabe. Electron scattering and photoionization of one-electron diatomic molecules. *Phys. Rev. A*, 85:022708, Feb 2012.

[65] P. Antoine, A. L'Huillier, M. Lewenstein, P. Salières, and B. Carré. Theory of high-order harmonic generation by an elliptically polarized laser field. *Phys. Rev. A*, 53:1725–1745, Mar 1996.

[66] S. Borbély, G. Zs. Kiss, and L. Nagy. The excitation and ionization of the hydrogen atom in strong laser fields. *Central European Journal of Physics*, 8:249, 2010.

[67] S. Borbély, K. Tőkési, and L. Nagy. Ionization of the hydrogen atom by intense ultrashort laser pulses. *Phys. Rev. A*, 77:033412, Mar 2008.

[68] G.Zs. Kiss, S. Borbély, and L. Nagy. Momentum space iterative solution of the time-dependent schrödinger equation. *AIP. Conf. Proc*, 1564:78, Nov 2013.

[69] D. Levin. Fast integration of rapidly oscillatory functions. *Journal of Computational and Applied Mathematics*, 67, 1996.

[70] G. Duchateau, E. Cormier, and R. Gayet. Coulomb-volkov approach of ionization by extreme-ultraviolet laser pulses in the subfemtosecond regime. *Phys. Rev. A*, 66:023412, Aug 2002.

[71] G.Zs. Kiss, S. Borbély, and L. Nagy. An efficient numerical discretization method for the study of the $H_2^+$ in intense laser fields. *AIP Conf. Proc.*, 1694:200171, 2015.

[72] A. Messiah. *Quantum Mechanics*, volume I. North-Holland Publishing Company, 1961.

[73] M. Born and J.R. Oppenheimer. Zur quantentheorie der molekeln [on the quantum theory of molecules]. *Annalen der Physik*, 389:457–484, 1927.

[74] J.J. Sakurai. *Advanced Quantum Mechanics*. Addison-Wesley, 1967.

[75] C.J. Foot. *Atomic Physics*. Oxford University Press, 2005.

[76] Daniel Dundas. Efficient grid treatment of the ionization dynamics of laser-driven $H_2^+$. *Phys. Rev. A*, 65:023408, 2002.

[77] Liang-You Peng, Daniel Dundas, J F McCann, K T Taylor, and I D Williams. Dynamic tunnelling ionization of $H_2^+$ in intense fields. *J. Phys. B: At. Mol. Opt. Phys*, 36:295–302, 2003.

[78] L.D. Landau, E.M. Lifshitz, and L.P. Pitaevskii. *Electrodynamics of Continuous Media (Volume 8 of the Course of Theoretical Physics)*. New York: Pergamon Press, 1984.

[79] C.D.T. Runge. Über die numerische auflösung von differentialgleichungen. *Mathematische Annalen*, 46:162–178, 1895.

[80] W. Kutta. Beitrag zur näherungweisen integration totaler differentialgleichungen. *Z Math Phys*, 46:435–453, 1901.

[81] A.N. Krylov. Translated from russian into english: On the numerical solution of equation by which are determined in technical problems the frequencies of small vibrations of material systems. *Izvestija AN SSSR (News of Academy of Sciences of the USSR)*, 7:491–539, 1931.

[82] P. Rácz, Z. Pápa, I. Márton, J. Budai, P. Wrobel, T. Stefaniuk, C. Prietl, J. R. Krenn, and P. Dombi. Measurement of nanoplasmonic field enhancement with ultrafast photoemission. *Nano Lett.*, 17:1181–1186, 2017.

[83] J. Budai, Z. Pápa, I. Márton, P. Wróbel, T. Stefaniuk, Z. Márton, P. Rácza, and P. Dombi. Plasmon-plasmon coupling probed by ultrafast, strong-field photoemission with ¡7 angström sensitivity,. *Nanoscale*, 10:16261–16267, 2018.

[84] M. Hiyama and H. Nakamura. *Two-center Coulomb functions*, volume 103. Computer Physics Communications, 1997.

[85] V. Hernández, J.E. Roman, and V. Vidal. Slepc: A scalable and flexible toolkit for the solution of eigenvalue problems. *ACM Trans. Math. Software*, 31(3):351–362, 2005.

[86] A. Tóth, S. Borbély, G.Zs. Kiss, G. J. Halász, and Á. Vibók. Towards the full quantum dynamical description of photoninduced processes in $D_2{}^+$. *J. Phys. Chem. A*, 120:9411, 2016.

[87] C.Amovilli and N.H.March. Characterization of potential energy curves for $H_2{}^+$ and $H_2$ by local values of electron density. *Chemical Physics*, 146:207–210, Sep 1990.

[88] G.Zs. Kiss, S. Borbély, and L. Nagy. Efficient numerical method for investigating diatomic molecules with single active electron subjected to intense and ultrashort laser fields. *AIP Conf. Proc.*, 1916:20010, 2017.

[89] K.-J. Yuan, H. Lu, and A.D. Bandrauk. Linear- and circular-polarization photoionization angular distributions in $H_2$ and $H_2{}^+$ by attosecond xuv laser pulses. *Phys. Rev. A*, 83:043418, Apr 2011.

[90] K.-J. Yuan, H. Lu, and A.D. Bandrauk. Molecular photoelectron interference effects by intense circularly polarized attosecond x-ray pulses. *A.D. Struct Chem*, 28:12971309, Oct 2017.

[91] L. Czipa and L. Nagy. Two-center interference in the ionization of $H_2$ by ion impact: Comparison of different models. *Phys. Rev. A*, 95:062709, Jun 2017.

[92] L. Nagy, S. Borbély, and K. Póra. Interference effects in the photoionization of molecular hydrogen. *Phys. Lett. A*, 327:481–489, 2004.